ORIGINAL PAPER

Laser Powder Bed Fusion Printing of CoCrFeMnNi High Entropy Alloy: Processing, Microstructure, and Mechanical Properties

Sila Ece Atabay[1,2] · Sheida Sarafan[1] · Aminul Islam[3] · Fabrice Bernier[1] · Javad Gholipour[1] · Robert Amos[4] · Prakash Patnaik[1] · Priti Wanjara[1] · Mathieu Brochu[2]

Abstract

Equiatomic CoCrFeMnNi high entropy alloy (HEA) powder was processed by laser powder bed fusion (LPBF) additive manufacturing (AM). The properties of the spherical pre-alloyed CoCrFeMnNi powder were characterized and its process-ability using LPBF AM was systematically investigated through the volumetric energy density (VED) based on the surface roughness, defects (micro-cracks and porosity) and densification. After optimization, LPBF processing at a VED of 104 J/mm^3 achieved highly dense and crack-free vertical and horizontal test specimens with a porosity fraction lower than 0.01% and micro-pores having a mean size of, respectively, 25.9 μm and 13.4 μm, as determined from X-ray micro-computed tomography (μCT) inspection. Scanning electron microscope (SEM) analysis of the as-built (AB) CoCrFeMnNi processed at a VED of 104 J/mm^3 showed a heterogeneous solidification microstructure, consisting of columnar grains with a cellular subgrain structure, and electron backscattered diffraction (EBSD) revealed a crystallographic texture mainly along the < 100 > direction. Post treatment with hot isostatic pressing (HIP) was effective in closing the remnant micro-pores in the bulk volume of the AB CoCrFeMnNi. Also, the cellular sub-grain structure in the AB CoCrFeMnNi completely disappeared after HIP and the resulting microstructure consisted of recrystallized equiaxed grains with annealing twins. The room temperature tensile response was anisotropic for AB CoCrFeMnNi with horizontally built specimens exhibiting higher strength and fracture strains (global and local) compared to vertically built ones; HIP reduced the anisotropy in the tensile properties and led to similar tensile strength with elongation values that were ~ 50% higher than in the AB condition. The HIPed CoCrFeMnNi also displayed higher Charpy impact toughness and absorbed energy at both room and liquid nitrogen temperatures compared to the AB material. Examination of the fracture surfaces after tensile and Charpy impact testing revealed ductile features with characteristic dimpled appearance and pointed to the important role of the remnant micro-pores on failure in the AB CoCrFeMnNi. Tribological assessments pointed to the superior low-stress abrasion resistance of AB and HIPed CoCrFeMnNi compared to 316L stainless steel (SS), which was included in this study to reinforce the analysis. SEM observations revealed that scratching and micro-fracture are the dominant wear mechanisms for the CoCrFeMnNi HEA, whereas ploughing and cutting parallel to the abrasive flow direction are the dominant mechanisms for 316L SS. To the authors' knowledge, this study is the first to evaluate and report the low-stress abrasion resistance of any high entropy alloy. To understand the corrosion behavior, polarization curves of AB and HIPed CoCrFeMnNi were measured in 3.5 wt% NaCl and 1N H_2SO_4 solutions, and the results were compared to those of 316L SS. The findings indicate that AB and HIPed CoCrFeMnNi outperform 316L SS in a chloride-containing environment, but not in an acid-containing environment. Additionally, observations of hydrogen permeability revealed that AB CoCrFeMnNi permeates a lower volume of hydrogen atoms (by ~ 5 times) compared to 316L SS, despite its higher (by nearly 3 times) diffusion coefficient. Electrochemical hydrogen permeation data showed that the concentration of atomic hydrogen in the sub-surface of AB and HIPed CoCrFeMnNi was, respectively, about 32 and 26 times lower than in 316L SS. This study provides important material–structure–property data and indicates a promising outlook for LPBF of the CoCrFeMnNi HEA with high-performance.

Extended author information available on the last page of the article

Abbreviations

2D	Two dimensional
3D	Three dimensional
AB	As-built
AD	Apparent density
AM	Additive manufacturing
AOR	Angle of repose
BD	Build direction
BCC	Body centered cubic
CAD	Computer-aided design
CE	Counter electrode
CI	Cohesive index
CR	Corrosion rate
D_{eff}	Effective diffusion coefficient
DIC	Digital image correlation
DSC	Differential scanning calorimetry
EBSD	Electron backscatter diffraction
E_b	Breakdown potential
E_{corr}	Corrosion potential
ε_f	Fracture strain
E_p	Passivation potential
E_{pit}	Pitting potential
E_{pp}	Primary passivation potential
ED	Energy density
EDM	Electro-discharge machining
EDS	Energy dispersive spectroscopy
EW	Equivalent weight
F	Faraday constant
FCC	Face-centered cubic
FTIR	Fourier transform infrared
h	Hatch distance
HEA	High entropy alloy
HIP	Hot isostatic pressing
HRC	Hardness Rockwell C-scale
$HV_{0.5}$	Vickers hardness at 500 g load
ICP-OES	Inductively coupled plasma-optical emission spectroscopy
I_{corr}	Corrosion current
I_{pass}	Passivation current
I_{ss}	Steady-state current
IM	Intermetallic
IGA	Instrumental gas analysis
IPF	Inverse pole figure
Jss	Permeation flux
K_1	Constant
L	Permeation coupon thickness
LPBF	Laser powder bed fusion
LN2	Liquid nitrogen
μCT	Micro-computed tomography
MUD	Multiple of uniform density
OCP	Open circuit potential
ρ	Density
P	Power
PSD	Particle size distribution
R_a	Arithmetic mean height
R_z	Maximum height
S_a	Areal arithmetic mean height
S_z	Areal maximum height
SCE	Saturated calomel electrode
SEM	Scanning electron microscope
SS	Stainless steel
STD	Standard deviation
t	Layer thickness
t_b	Breakthrough time
t_{lag}	Time lag
T_M	Material toughness
TGA	Thermogravimetric analysis
UTS	Ultimate tensile strength
v	Scanning speed
VED	Volumetric energy density
XRD	X-ray diffraction
YS	Yield strength

Introduction

Traditionally, alloy development has been predominately based on selecting a principal element (i.e., Fe, Cu, Al, or Ni) as the matrix with minor additions of alloying elements to modify the properties. This classical alloy design concept greatly limits degrees of freedom in new alloy development and, thus, the number of practical alloys, and their range of achievable properties. By the end of the 1970s, the advancement of high-performance alloys reached a plateau, which, in early 2000 [1], was disrupted by the emergence of high entropy alloys (HEAs), which are a new, underexplored class of materials consisting of multiple principal elements in equal or nearly equal atomic concentrations. One of the first equiatomic HEAs is the Cantor alloy CoCrFeMnNi, which forms a single-phase solid solution with a face-centered cubic (FCC) structure [2]. On the basis of previous research [3–5] on the synthesis of CoCrFeMnNi using conventional processing—i.e., predominately via a casting route and then followed by different thermal [6] and/or mechanical post-processing treatments—the microstructural stability [7] and resulting performance showed promise for developing this alloy for applications requiring a combination of high mechanical strength and high ductility at both high and low temperatures [8]. However, eliminating/reducing macro-scale segregation of alloying elements during solidification of this alloy has presented a key challenge for manufacturing homogenous castings/ingots [9].

Thus, more recent research on equiatomic CoCrFeMnNi HEA has considered fabrication via metal additive manufacturing (AM) technologies, which are rapidly mainstreaming beyond prototyping to production-at-scale of high

complexity, customized, and near-net-shape structures, especially using powder bed fusion processes with laser as the energy source. To date, research on laser powder bed fusion (LPBF) AM of CoCrFeMnNi has examined the printability [10–12], powders other than pre-alloyed feedstock [13, 14], process/parametric influences [15, 16], post-processing [17, 18], microstructural analysis [19, 20], room temperature compressive [21], tensile [22] and fatigue [23–25] properties, and elevated temperature properties [13, 26], to name a few. A number of studies on LPBF processing have reported that the CoCrFeMnNi HEA has good printability [11, 18, 25] owing partially to its narrow solidification/freezing range (i.e., the range between the liquidus and solidus temperatures) of 69 °C (1280 °C—1349 °C) [27], which should minimize the risk of solidification/liquation cracking. Even so, the CoCrFeMnNi HEA is susceptible to solidification cracking—perhaps due partly to the addition of Mn that nearly doubles the gap between the solidus and liquidus relative to the quaternary (CoCrFeNi) alloy [27]—and several studies have conveyed the processing and performance sensitivity to the LPBF parametric conditions [15, 16, 22, 23]. Anisotropic properties have been another important concern for LPBF AM of CoCrFeMnNi HEA [11, 21, 28, 29], but research on subsequent heat treatments [30] and/or hot isostatic pressing (HIP) [18], to reach a more isotropic mechanical response, has been limited. Moreover, apart from strength (compressive, tensile, fatigue), the relationship between such processing factors and other properties—e.g., impact, wear, hydrogen permeation, corrosion—have not been systematically explored for CoCrFeMnNi fabricated by LPBF processing.

Accordingly, this research study was defined to further understand the processing and performance of additively manufactured CoCrFeMnNi. Specifically, as the LPBF process and the resulting microstructure and properties depend on the characteristics of the starting powder, the commercially available pre-alloyed CoCrFeMnNi powder used in this study was examined to evaluate its particle size distribution, morphology, chemical composition, chemical homogeneity, phase composition, density, as well as static and dynamic flowability. The processability of this powder to print cubic ($5 \times 5 \times 5$ mm^3 and $10 \times 10 \times 10$ mm^3) coupons was investigated to understand the operational window for LPBF manufacturing of highly dense and crack-free CoCrFeMnNi specimens. Based on the best combination of process conditions, test specimens—oriented perpendicular (horizontal) and parallel (vertical) to the build direction

(BD)—were printed to study the porosity features using X-ray micro-computed tomography (μCT), macro/microstructure, hardness, tensile properties, Charpy impact properties at room and liquid nitrogen (LN2) temperatures and the fracture characteristics, both in the as-built (AB) state and after post-process HIP. The response of the AB and HIPed CoCrFeMnNi to low-stress abrasion wear (ASTM G65 [31]), hydrogen permeation (ASTM G148 [32]), and electrochemical corrosion (ASTM G5 [33]) was also studied to gain insight into the resistance of this HEA to material degradation so as to expand applications in different environments, which is key for transitioning to net-zero emissions with alternate energy sources including hydrogen.

Materials and Methods

The starting material used in this study was commercially available pre-alloyed argon gas-atomized equiatomic CoCrFeMnNi powder from Stanford Materials (Lake Forest, CA, USA) with an elemental composition as given in Table 1. The morphology of the starting powder particles was analyzed using a Hitachi SU3500 (Fukuoka, Japan) scanning electron microscope (SEM) equipped with a detector for energy dispersive spectroscopy (EDS). As shown in Fig. 1a, and 1b; the majority of the as-received powder particles were spherical with a few irregularities and fine satellites attached to their surfaces. The particle size distribution (PSD) of the CoCrFeMnNi powder was measured using an LA-920 Horiba (Kyoto, Japan) laser particle size analyzer, and the results are shown in Fig. 1c. The PSD analysis showed a normal distribution with D_{10}, D_{50}, and D_{90} values of 27 μm, 38 μm, and 56 μm, respectively.

Cross-sectional analysis of the CoCrFeMnNi powder particles revealed the occasional presence of spherical pores (Fig. 2) that likely originated from entrapped gas during the atomization process, as can be seen in other additive powders [34, 35]. Also, EDS elemental maps were acquired from a single powder particle to understand the elemental distribution within the powder feedstock. As shown in the elemental maps in Fig. 2, there is solute partitioning with the dendrites enriched in Fe and to a much lesser extent Co, and Cr, while the interdendritic regions are enriched in Mn and to a lesser extent Ni. The depletion in the Fe and enrichment in the Mn content at the interdendritic region indicates Mn segregation during solidification after gas atomization

Table 1 The chemical composition of the feedstock CoCrFeMnNi powder and the LPBF-fabricated test parts

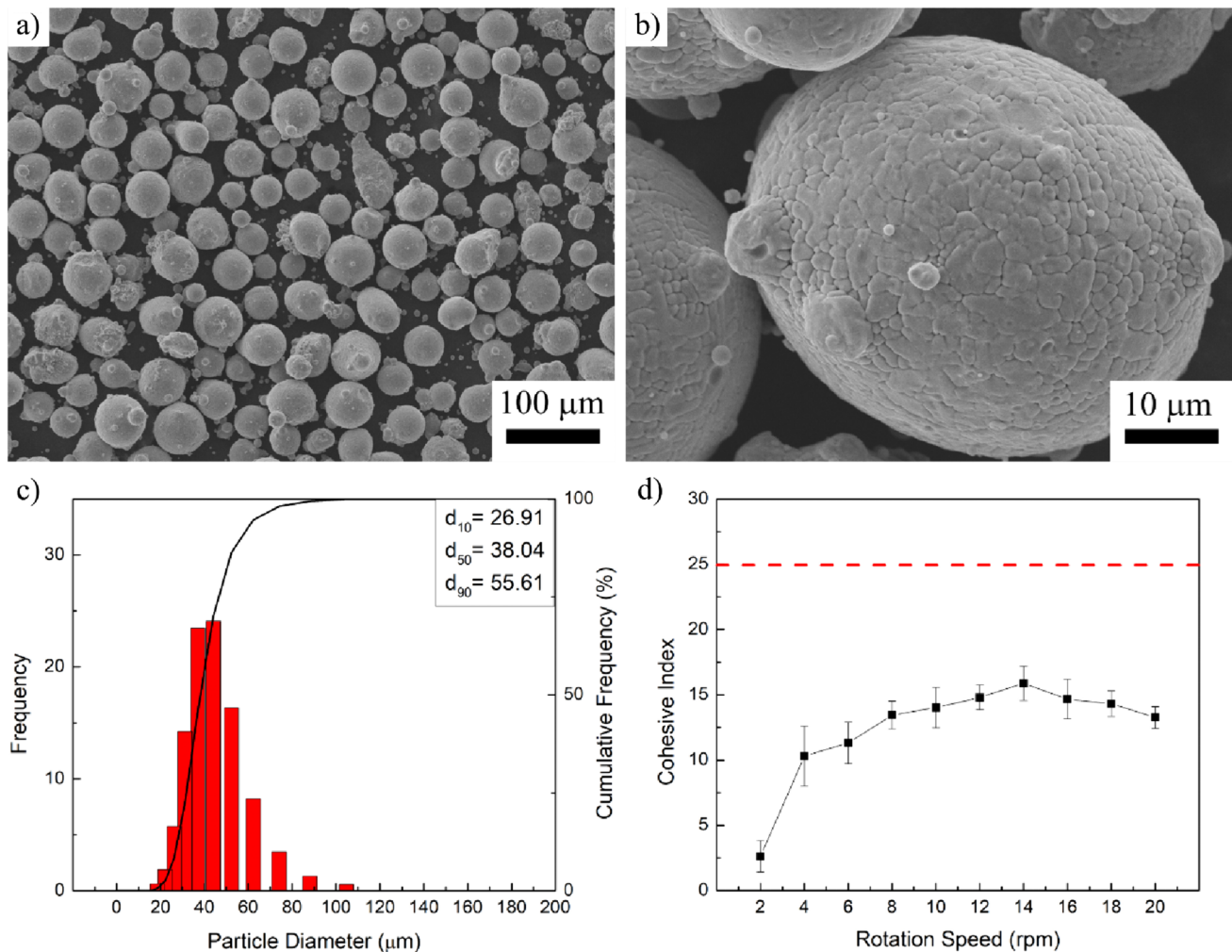| Element	Co	Cr	Fe	Mn	Ni	O (ppm)
Powder (wt%)	21.1	18.1	20.1	19.8	21.4	370
LPBF part (wt%)	21.6	18.1	20.5	18.4	20.9	590

Fig. 1 a and **b** Morphology, **c** particle size distribution, and **d** cohesive index (CI) of the starting CoCrFeMnNi powder in relation to the CI upper limit of 25 (dotted line) for good spreadability during LPBF processing according to [39]

of the pre-alloyed CoCrFeMnNi powder feedstock used in the present study. This finding is supported by previous research [36] that attributed solute partitioning during the solidification of the CoCrFeMnNi alloy system to the relatively low melting temperature of Mn compared with that of other elements (Co: 1495 °C, Cr: 1907 °C, Fe: 1538 °C, Mn: 1246 °C, and Ni: 1455 °C).

Flowability and the apparent density of the powder were assessed using Hall and Carney funnels according to the specifications in ASTM B213 [37] and ASTM B964 [38]. The measured flow rates of the powder from the Hall and Carney funnels were, respectively, 17.9 ± 0.2 s and 3.2 ± 0.1 s for 50 mg of powder, as shown in Table 2, indicating that the powder has suitable flowability to be used in the LPBF process. The apparent density of the powder was assessed as 4.3 g/cm^3. Also, dynamic flowability analysis was conducted using a GranuDrum (Granutools, Avans, Belgium) rotating drum instrument. Figure 1d shows the

cohesive index (CI) of the starting powder as a function of the drum rotational speed from 2 to 20 rpm. The average of the three measured CI values ranged between 3 and 16, indicating that the starting powder has good flowability. It is suggested that metal powders having CI values lower than 25 show good flowability and spreadability characteristics, resulting in a uniform powder layer for LPBF processing [39].

The specimens examined and tested in this study were fabricated with a Renishaw AM400 LPBF system equipped with a reduced build volume chamber using an Nd: YAG laser with a maximum power output of 400 W and a beam diameter at the focus of ~ 70 μm. The process was conducted under argon gas atmosphere with oxygen levels lower than 300 ppm. A bi-directional scanning strategy was used for LPBF fabrication with a 67° rotation between each layer. Various process parameters with an equivalent volumetric energy density (VED) value ranging between 47 and 148 J/
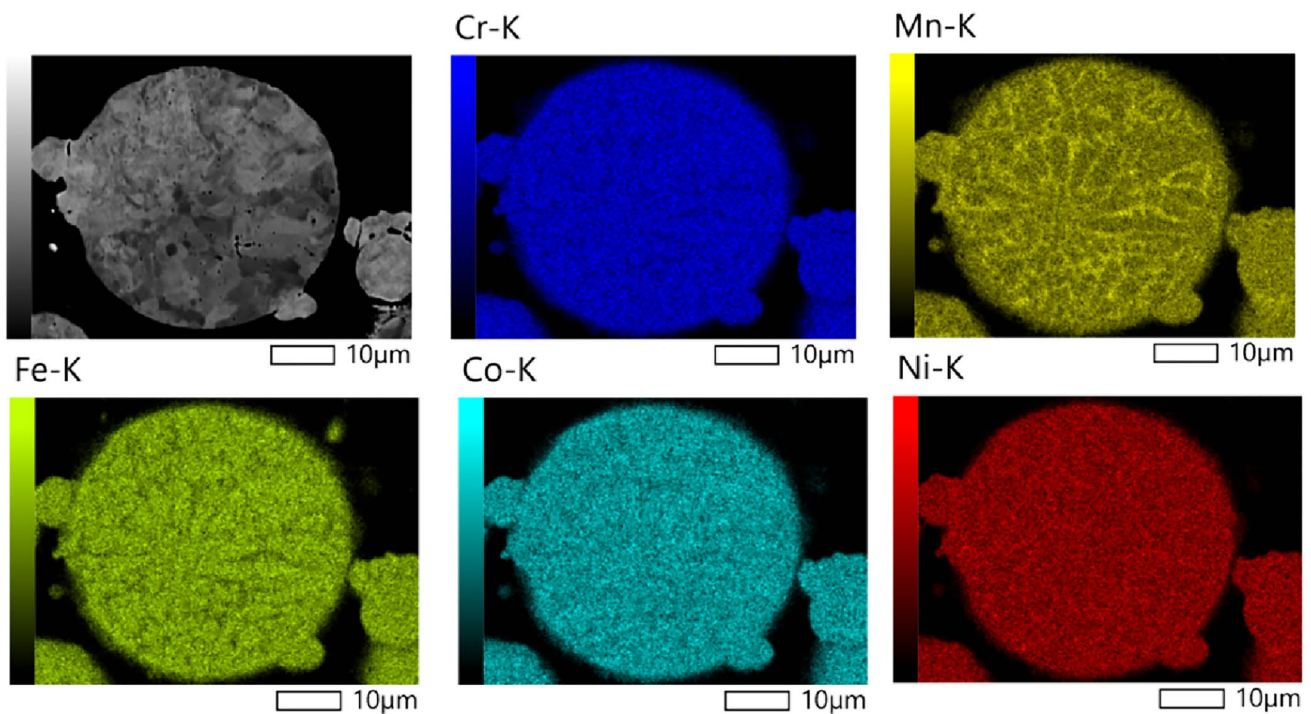
Fig. 2 EDS elemental maps of a representative CoCrFeMnNi powder particle

Table 2 Flowability and apparent density of the CoCrFeMnNi powder through Hall and Carney funnels

Hall Flow (s/50g)	Carney Flow (s/50g)	Apparent Density (g/cm^3)
17.9 ± 0.2	3.2 ± 0.1	4.3 ± 0.03

Table 3 Process parameters used for LPBF of CoCrFeMnNi alloy

Power (W)	Hatch distance (µm)	Point distance (µm)	Exposure time (µs)	Layer thickness (µm)	VED* (J/mm^3)
120–200	50–80	50–80	80–100	30	47–148

*Volumetric energy density

mm^3 were examined for LPBF processing. The range for each process parameter used for optimization is given in Table 3. Cubic specimens with dimensions of $5 \times 5 \times 5$ mm^3 and $10 \times 10 \times 10$ mm^3 were fabricated for the parametric optimization studies and microstructural analysis. Using the best combination of process parameters, two different sets of rectangular bar specimens with dimensions of $8 \times 8 \times 42$ mm^3 and $8 \times 10 \times 55$ mm^3 were fabricated at a VED of 104 J/mm^3 in both the vertical and horizontal directions for tensile testing and Charpy impact testing, respectively. Also test specimens measuring $26 \times 48 \times 5$ mm^3 were fabricated at a VED of 104 J/mm^3 for wear, hydrogen permeation and electrochemical corrosion testing. After fabrication, selected specimens were subjected to HIP at 1150 °C for 3 h under 150 MPa pressure.

The specimens were removed from the baseplate using electro-discharge machining (EDM) (FANUC Robocut C400iB, Oshino-mura, Yamanashi, Japan) with a brass wire having a diameter of 0.2 mm. The surface quality of the fabricated CoCrFeMnNi was evaluated by measuring the linear and areal surface roughness parameters on both the top and side faces of the cubic specimens. Linear roughness profiles were assessed in accordance with ASTM B946-23 [40] using a portable Surftest SJ-210 (4 mN type profilometer, Mitutoyo Aurora, IL, USA) with a tip radius of 2 µm. The arithmetic mean height (R_a), and maximum height (R_z) values were derived from a primary line profile with an evaluation length of 6 mm by suppressing the long-wave component using the high-pass filter with a cut-off of $\lambda_c = 0.8$ mm. Three traverses (profiles) at different locations were undertaken to calculate the average values of the linear roughness parameters. In regards to the areal roughness parameters, Sa and Sz are the counterpart of Ra and Rz. Measurement of the Sa and Sz was guided by the principles in ISO 25178-2 [41] and performed over a definition area of 2 mm^2 on both the top and side surfaces of the specimens using a 3D laser scanning confocal microscope (Keyence VK-X250, Osaka, Japan).

The bulk density of each specimen was measured at room temperature using the Archimedes water immersion method

with a theoretical density value of 7.96 g/cm^3 to calculate the relative density of CoCrFeMnNi HEAs processed by LPBF AM and HIP. Also, X-ray µCT was used to analyze representative horizontal and vertical test specimens both in the AB and HIPed conditions to study the porosity evolution. X-ray µCT was undertaken on these specimens using a Nikon HMXST 225 system (Brighton, MI, USA) equipped with a Perkin-Elmer 1621AN CsI (2000×2000 pixels, 40×40 cm^2 and 200 µm/pixel) detector panel. The X-ray µCT system was operated at a voltage of 155 kV, a current of 57 µA with an exposure time of 708 ms. Four frames per projection were taken and a voxel size of 2.5 µm was used. The volume of the inspected region was ~ 30 mm^3, while the volume of the analysis region was 20 mm^3. For the inspection, pores were filtered at 10 voxels (i.e., pores containing less than 10 voxels were excluded from the analysis). For image analysis, Dragonfly software was utilized for the 3D reconstruction to analyze the volume and size distribution of the pores. The porosity levels were detected using a lower Ostu threshold [42–45] to select the region of interest of the pores.

The chemical composition of the LPBF-fabricated specimens was characterized using instrumental gas analysis (IGA) to determine the composition of the main alloying elements and inductively coupled plasma-optical emission spectroscopy (ICP-OES) to determine the oxygen content, compared with the powder composition. As shown in Table 1, LPBF processing did not result in a significant change in the CoCrFeMnNi composition or oxygen pick up.

Thermal analysis of the CoCrFeMnNi powder and fabricated specimens was undertaken using thermogravimetric analysis (TGA) and differential scanning calorimetry (DSC) (Netzsch STA 449 F1, TGA-MS-FTIR; Selb, Germany) in the temperature range of 40 to 1500 °C, at a heating rate of 20 °C /min under 50 mL/min argon atmosphere for 1 h. The TGA was coupled to a Fourier transform infrared (FTIR) spectrometer (Bruker Tensor 27, Opus 8.5 software) to investigate in tandem, the sample composition (i.e., evolved gas analysis). Temperature and mass calibrations followed the manufacturer's recommended procedures. Typically, 15 to 20 mg of each specimen was loaded into an empty aluminum oxide crucible. All TGA/DSC were processed with Proteus Analysis Software (version 8.0.2) and smoothing (7th order) was applied to all the derived thermogravimetric curves. In the present work, TGA-FTIR was explored to characterize the surface of the atmospherically exposed CoCrFeMnNi powder (i.e., after removal from the vacuum sealed container) and fabricated specimens in the AB and HIPed conditions. The thermograms indicated low mass losses with values ranging from 0.3 to 0.8% for the CoCrFeMnNi powder, 1.2–2.6% for the AB specimens and 1.4–1.6% for the HIPed specimens, which are statistically similar. Analysis

of the evolved product gases indicated the minor presence of carbon monoxide, carbon dioxide and/or water vapour from the CoCrFeMnNi powder and fabricated specimens.

For microstructural characterization, the cubic CoCrFeMnNi specimens were sectioned parallel to the BD and then mounted and ground with 600 grit SiC paper. The specimens were then polished with 9 µm, 3 µm, and 1 µm diamond suspensions on a rigid composite disc, followed by synthetic polishing cloths. Final polishing was performed using a 0.05 µm colloidal silica suspension on a Vibromet 2 polisher (Buehler, Longueuil, QC, Canada).

A Keyence VK-X250 3D laser scanning confocal microscope was used for optical imaging of the polished cross-sections. The entire cross-section was scanned and all the images were analyzed using image analysis software Image J [46] to quantify the relative optical density, crack lengths and crack densities. To reveal the microstructure, the CoCrFeMnNi specimens were etched for 5–10 s using a mixture consisting of 100 ml ethanol, 100 ml HCl, and 5 g CuCl$_2$. A JCM-7000 NeoScope™ benchtop SEM (JEOL, Akishima, Tokyo, Japan) equipped with EDS facilitated observation and characterization of the microstructure.

Detailed examination of the grain morphology and texture was conducted by electron backscatter diffraction (EBSD) on the surfaces of selected specimens (after vibratory polishing) using a Hitachi SU3500 SEM under operating conditions of 15 kV with a 2 µm step size. The raw EBSD data were collected using Aztec data acquisition software and analyzed with HKL Channel 5 data processing software (Oxford Instruments NanoAnalysis, Concord, MA, USA). Pole figures of the {100}, {110}, and {111} planes were extracted from the EBSD data using a half-width of 10° and a cluster size of 5°. Also, the grain diameter and aspect ratio of the grains were visualized using the inverse pole figure (IPF) maps obtained from the EBSD analysis. Image J software and a line intercept method was used to measure the average length of the grains from the IPF maps. Phase analysis of the pre-alloyed CoCrFeMnNi powder and fabricated specimens was conducted by X-ray diffraction (XRD) analysis using a Bruker D8 Discovery X-Ray diffractometer with Co Kα1 radiation (wavelength 1.78897 Å) and operating at 35 kV with 45 mA.

Microhardness measurements were performed according to ASTM E384 [47] standard on the CoCrFeMnNi specimens using a Struers DuraScan 80 hardness tester (Ballerup, Denmark). Individual hardness indentations were measured on the entire polished surfaces of the AB cubic specimens (5×5 mm^2 and 10×10 mm^2) using a spacing of 0.5 mm and a load of 300 g for 15 s, so as to determine the hardness distribution. The data presented correspond to an average hardness observed at each VED condition

studied. Microhardness testing was also used to understand the impact of the HIP treatment on the LPBF-fabricated test specimens.

The room temperature tensile properties of the horizontally and vertically built specimens were determined using a 250 kN MTS load frame integrated with a laser extensometer (Eden Prairie, MN, USA) and a non-contact optical 3D deformation measurement system (referred often as digital image correlation (DIC)), Aramis® GOM-Trillion Quality Systems, (King of Prussia, PA, USA). For each direction (horizontal and vertical) and condition (AB and HIPed), round test specimens with a reduced cross-sectional diameter of 2.5 mm and a gauge length of 10 mm were machined from the rectangular bars for tensile testing, according to ASTM E8/E8M-22 [48]. Before tensile testing, two pieces of retro-reflective tape were attached to one side of the tensile specimen to distinguish the gage section for the laser extensometer during testing. On the opposite side, the surface of the tensile specimen was first painted with a white background and then a high-contrast random pattern of black speckles was applied, as illustrated in [49]. As the functionality of the Aramis® system is sensitive to the quality of this speckle pattern, verification of pattern recognition was performed before tensile testing to ensure proper strain recording along the entire gage length, as described in [50–52]. Tensile tests were conducted with a strain rate of 10^{-3} s^{-1} and between 4 and 5 specimens were tested for each specimen condition. To obtain the stress–strain curves and the related mechanical properties—yield strength (YS), ultimate tensile strength (UTS) and fracture strain (ε_f)—the load data, collected by the tensile testing machine, was used to calculate the engineering stress, while the data collected by the laser extensometer was used to calculate the global strain or elongation, based on the assumption that the entire gauge length is under uniform or homogeneous deformation. By contrast, the strain maps captured by the Aramis® system were used to assess the local deformation behavior of the specimens during tensile testing and measure the local strain just before fracture. As well, the material toughness (T_M)—also referred to as modulus of toughness—was calculated from the area under the engineering stress–strain curve for each specimen condition to evaluate the strain energy density (strain on a unit volume of material) that the CoCr-FeMnNi alloy can absorb before fracture.

V-notch Charpy impact specimens were machined according to ASTM E23-16a [53]. Charpy impact testing was performed using a Satec Systems SI Series pendulum impact tester at room temperature (~ 293 K) and at LN2 temperature (~ 77 K). For each condition (AB/HIP and horizontal/vertical), three specimens were tested at room temperature, and one specimen was tested at LN2 temperature, with the exception of the vertically built HIPed condition for which 3 specimens were tested at 77 K. Fractography analyses were conducted on the tested (tensile and impact) specimens after fracture using a JCM-7000 NeoScope™ Benchtop SEM.

The wear testing was conducted according to ASTM G65 Procedure A (dry sand rubber wheel) using a Falex friction/wear test machine [54]. AFS 50–70 Ottawa silica sand served as the abrasive particles and was fed at a controlled flow rate of 380 ± 5 g/min into the contact zone between a rotating rubber-rimmed wheel and the specimen. Figure 3a and b display the morphology and size distribution of the abrasive particles, respectively, with an average particle size falling within the range of 212–300 μm. The final dimensions of the test specimen measured $25.4 \times 47.7 \times 4.9$ mm^3. The test apparatus was calibrated before each test series, employing D2 tool steel with a volume loss of 35 ± 1 mm^3. Conditions were consistently maintained to ensure reliable

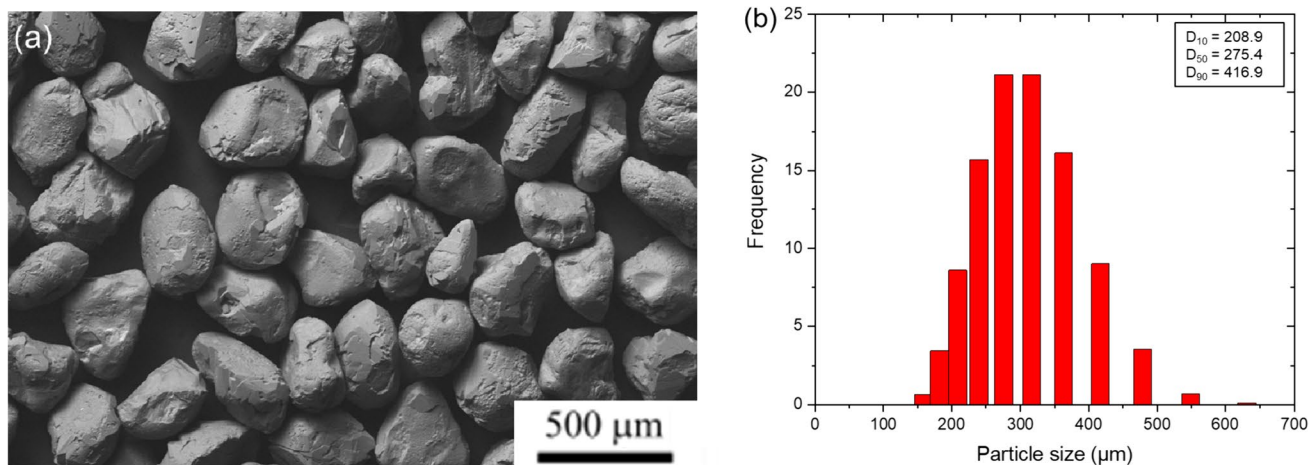**Fig. 3 a** Morphology of semi-angular AFS 50–70 silica sand, and **b** particle size distribution

results. To maintain humidity within the enclosed test chamber below 5%, the test chamber was purged with dried compressed air. Volume loss was measured using a laser profilometer, which was then adjusted by multiplying measured loss with the ratio of standard wheel diameter and wheel diameter after wear testing.

$$\text{Adjusted Volume Loss(AVL)} = \text{Measured Loss} \times \frac{228.6 \, \text{mm}(9.00'')}{\text{Wheel diameter after testing}} \tag{1}$$

Electrochemical corrosion tests were conducted using a three-electrode cell with a Gamry PC4/750 potentiostat, a saturated calomel electrode (SCE) as the reference electrode, and platinum as the counter electrode. The test specimen with a 1 cm^2 surface area served as the working electrode. The electrochemical tests were conducted at room temperature in two solutions: 3.5 wt% NaCl and 1.0 N H$_2$SO$_4$. Before each test, the specimens were allowed to stabilize for 90 min at the open circuit potential (OCP). Potentiodynamic polarization tests were carried out at a scan rate of 0.6 V/h, starting from an initial potential of -250 mV and ending at a final potential of -250 mV versus OCP. The corrosion rate (CR) was determined using Tafel extrapolations [55]:

$$CR = K_1 \times \frac{i_{cor}}{\rho} \times EW \tag{2}$$

Here, CR is in mm/yr, corrosion current (i_{corr}) in µA/cm^2, constant (K_1) is 3.27×10^{-3}, in mm g/µA cm yr, density (ρ) in g/cm^3 and EW is the equivalent weight (molecular weight/valency) in g. After the electrochemical tests, the specimens were rinsed with distilled water and air dried for examination.

Electrochemical hydrogen permeation tests were performed according to ASTM G148 standard [32] to evaluate the diffusion and trapping behavior of hydrogen. A schematic of the permeation tester is shown in Fig. 4. Permeation test coupons with dimensions of $25 \times 25 \times 1$ mm^3 were fabricated using the LPBF process at the optimal VED of 104 J/mm^3. In the initial testing phase, no permeation was observed after 72 h of charging, attributable to the high hydrogen permeation resistance of the specimens. Subsequently, the thickness of the specimens was reduced to 150 µm using EDM prior to further testing, as shown in Fig. 5. To ensure consistency and interference-free surface conditions, each specimen was ground using 600 grit sandpaper prior to the permeation test. The test specimens were cleaned via sonication before testing, employing a sequence of solutions in 5-min intervals: a mixture of soap and water (1:7 ratio), ultrapure water (18.2 MΩ), acetone, and methanol.

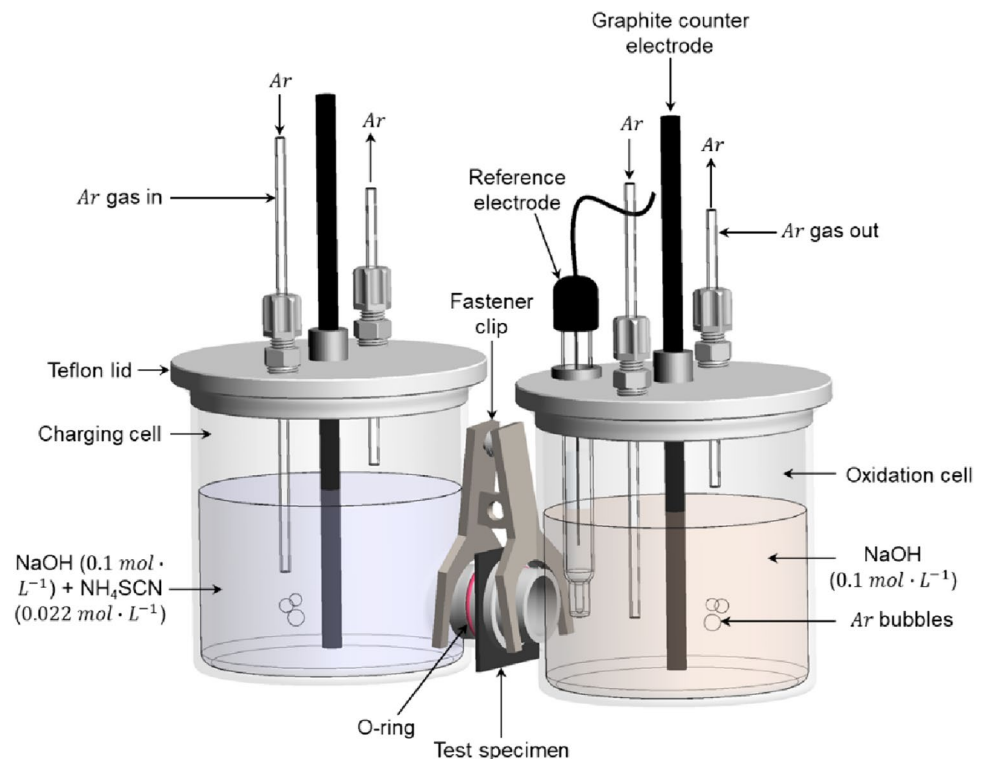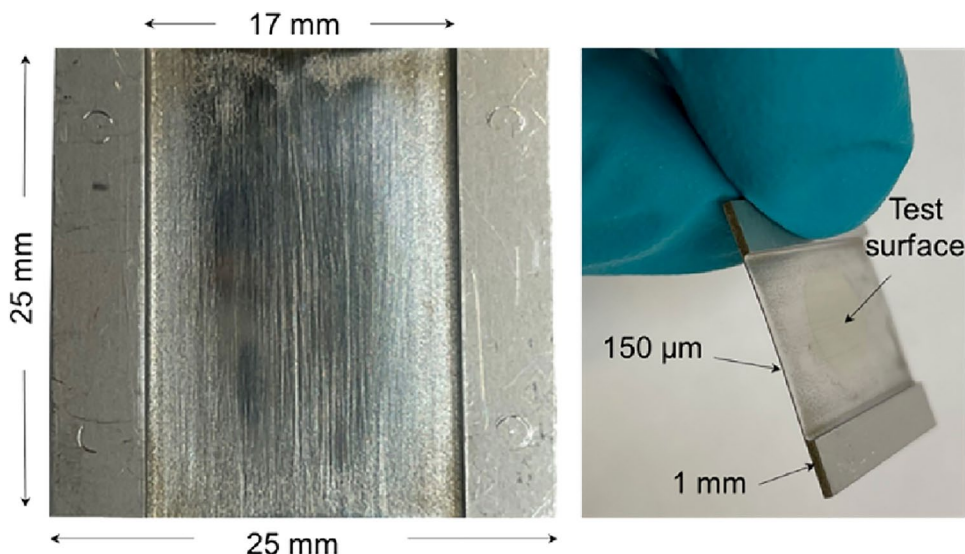**Fig. 4** Schematic of the hydrogen permeation testing device

Fig. 5 Test specimen for electrochemical permeation test

Table 4 Experimental parameters of electrochemical hydrogen permeation test

Parameter	Description
Charging cell solution	0.1molL^{-1} NaOH + 0.022mol NH$_4$SCN
Oxidation cell solution	0.1molL^{-1} NaOH
pH	~13.5
Maximum background current	<100 nA
Test duration	36 h
Sample rate	1 Hz
Reference electrode (RE)	Saturated Calomel electrode (SCE)
Counter electrode (CE)	Graphite rod
Applied potential	300 mV versus SCE
Purging gas	Argon

Following the cleaning process, thickness measurements were taken using a micrometer.

The test specimens were then clamped between the charging and oxidation cells using a gasket with an exposed area of 1 cm^2. During the permeation test, 0.1 mol L^{-1} sodium hydroxide (NaOH) and 0.022 mol L^{-1} ammonium thiocyanate (NH$_4$SCN) were used as the electrolyte in the charging cell, while 0.1 mol L^{-1} NaOH was in the oxidation cell. The NH$_4$SCN was added in the charging cell to reduce the recombination of hydrogen atoms. Argon gas was bubbled through both cells at a low flow rate (~one bubble per second) to reduce the amount of dissolved oxygen [56]. A Gamry electrochemical potentiostat (interface 5000) was connected to the specimen (working electrode). A graphite rod and SCE was used as the counter electrode (CE) and the reference electrode (RE), respectively. The permeation test was conducted at room temperature. Electrochemical permeation test parameters are summarized in Table 4. For the baseline acquisition, a chronoamperometry (CA) program was executed, maintaining a constant voltage of 300 mV versus SCE and a sample rate of 1 Hz. A stable baseline, i.e., background current, was achieved after 24 h. After acquiring a stable baseline, the power supply unit was activated to initiate the charging cycle, as depicted in Fig. 6. The permeation test continued until the current density reached its peak and stabilized, representing the steady-state current (I_{ss}).

From the electrochemical permeation test (Fig. 6), the hydrogen permeation flux can be determined by converting the steady-state hydrogen current (I_{ss}), measured at the point when the permeation curve reaches the steady-state, into the hydrogen permeation flux (J_{ss}) [57, 58]:

$$J_{ss} = \frac{I_{ss}}{F \times A}, \tag{3}$$

where A is the specimen area (m^2) and F is the Faraday constant (96,485 s A/mol). Effective diffusion coefficient, D_{eff} (m^2 s^{-1}) was then calculated using both time lag (t_{lag}) and breakthrough time (t_b) method using the following equations:

$$D_{eff,t_{lag}} = \frac{L^2}{6 \times t_{lag}} \tag{4}$$

$$D_{eff,t_b} = \frac{L^2}{15.3 \times t_b}, \tag{5}$$

where, L is the thickness of the test specimen. The breakthrough time (t_b) can be obtained by extrapolating the linear part of the permeation curve, while time lag (t_{lag}) corresponds to the time it takes to reach 63% of I_{ss}.

Fig. 6 Electrochemical permeation of 316L SS as representative example
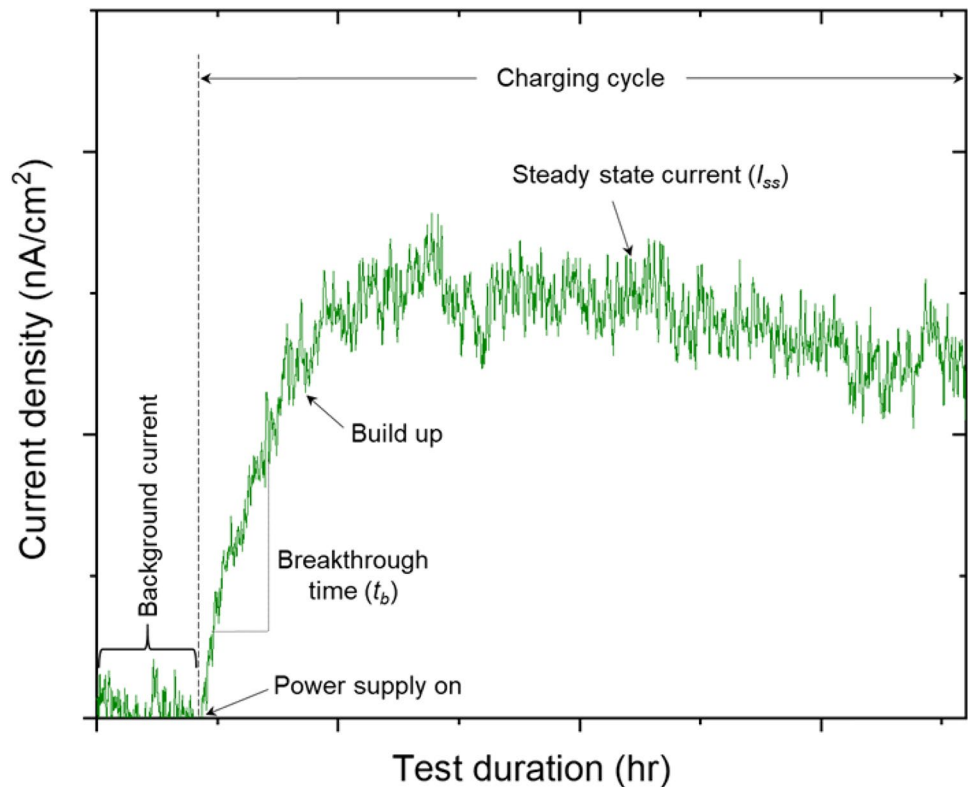
Results and Discussion

Surface Roughness

The topography of the top and side surfaces of the AB cubes was characterized and compared using a 3D laser scanning confocal microscope. Representative topological profiles of the top and side wall surfaces are shown in Fig. 7a and c, respectively. The top surface of all the specimens consists of periodical lines caused by the parallel scanning tracks during LPBF processing. The side surface of the AB specimens mainly consists of unmelted powder particles sintered to the surface of the part due to heating during fabrication.

Linear and areal surface roughness values were also measured for both the top and side surfaces of the cubes and summarized as a function of VED in Fig. 7b and d, respectively. For the top surface, the linear roughness parameters, R_a and R_z ranged between 3–10 and 18–70 µm, respectively. Both values show that the minimum surface roughness was achieved for VED values between 80 and 100 J/mm^3. Additionally, it can be seen that the roughness value decreases with increasing VED within that range. Surface areal roughness parameters S_a and S_z also revealed a similar trend. The highest value of S_a and S_z was measured for the specimens fabricated with the lowest VED

and a decreasing trend was observed until it reached a minimum at a VED value of 100 J/mm^3. Further increases in the VED resulted in a higher surface roughness. The linear and areal roughness measurements also show that the surface quality of the side walls is not as sensitive to the printing parameters as the top surface. Figure 7d shows that each of the VED values applied for the fabrication of the specimens in this study resulted in statistically similar roughness parameters for the side surface and no visible trend was observed for both the linear and areal surface roughness parameters. As the surface of the side walls mainly consisted of sintered powder particles, the main factor determining the roughness parameters are the powder bed and the size distribution of the powder. The similar values for the roughness parameters observed for all specimens could be explained by the use of the same powder feedstock.

Parameter Optimization

Regardless of the LPBF parameters utilized, each specimen showed a similar hierarchical microstructure in the AB condition. Representative SEM micrographs showing the typical solidification microstructure are given in Fig. 8. As can be seen in Fig. 8a, the etched cross-section of the specimens consists of semi-elliptical melt pools. The arrangement of these melt pools is determined by the scan
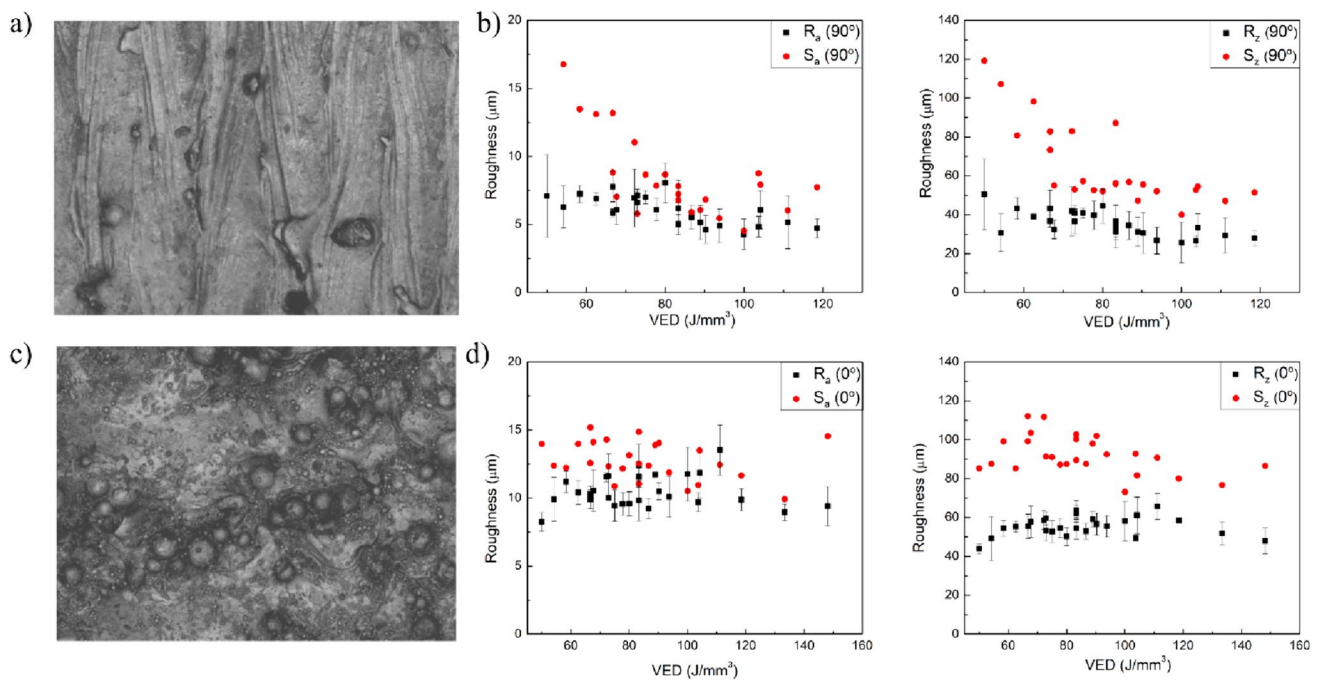
Fig. 7 **a** Representative surface topography of the top and **c** side faces of the AB CoCrFeMnNi specimens; linear and areal surface roughness measurements as a function of the VED for **b** top surface (R_a and S_a: left plot, R_z and S_z: right plot) and **d** side surface (R_a and S_a: left plot, R_z and S_z: right plot)
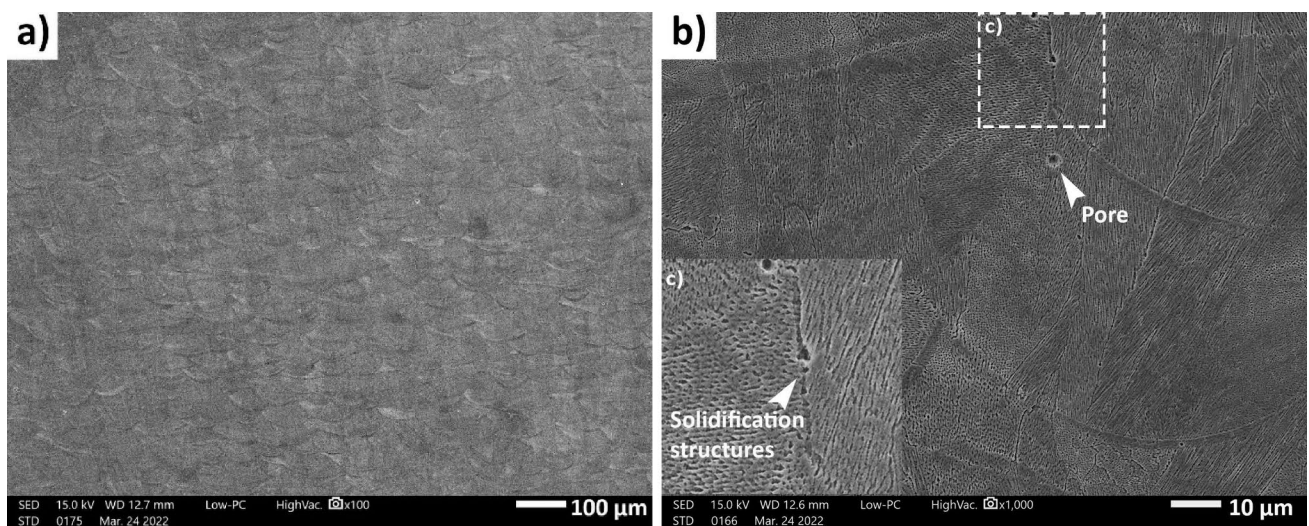

Fig. 8 **a** and **b** Representative SEM micrographs of AB CoCrFeMnNi with inset **c** showing a magnified view of the fine solidification structure

tracks that were alternating 67° between two successive layers. The size and overlapping of these melt pools varied for each specimen, since these are a result of the chosen LPBF process parameters. The SEM image in Fig. 8b shows the presence of columnar grains, starting from the bottom of the molten pools and growing for multiple layers along the BD. This reveals that the grains grew epitaxially parallel to the direction of maximum heat flow. Additionally, the solidification conditions during LPBF processing promoted the formation of a cellular subgrain structure, which is also visible in Fig. 8b and more clearly in the inset (c). It is noteworthy that the grain morphology and size of the solidification features are determined by the thermal gradient (G) and solidification front velocity (R). Thus, the microstructure

will change from equiaxed dendritic to columnar dendritic, cellular, and planar as the ratio of the G/R increases, and the size of the features will be smaller as the cooling rate increases. As a result, even though all the specimens showed epitaxially grown grains and cellular sub-grain structures, the cell and grain size of the various cube specimens studied showed some minor differences due to the variation in the LPBF process parameters during exploration of the process window to identify the optimal VED conditions. For the selected optimal process parameters and VED, a more detailed microstructural characterization was conducted and is discussed in Sect. 3.3.

The systematic parameter optimization study, conducted over a VED range of 47–148 J/mm^3, revealed not only differences in the surface roughness (as discussed in Sect. 3.1), but also the defects in the LPBF AB parts. The most frequently observed defects in the specimens were gas porosity, lack of fusion, and cracking. The relative optical density and Archimedes density of each specimen were calculated and are plotted as a function of their corresponding VED in Fig. 9. The plot in Fig. 9 shows no visible relationship between the VED and the density of the specimens. The main reason for this is that the applied VED equation accounts for an equal effect of each process parameter. Despite this, all the specimens having a VED lower than 60 J/mm^3, showed lack of fusion defects, while all the specimens having a VED higher than 110 J/mm^3 had a high number of large cracks. Representative micrographs of these defects are also presented in Fig. 9. Thus, it can be concluded that the optimal LPBF processing window for this alloy is between a VED of 60 and 110 J/mm^3. However, the density values varied considerably within this VED range, and further analysis of the individual effects of processing parameters was deemed necessary. Specifically, the optical density of all the specimens was above 99.5%, whereas the Archimedean density was varying between 97 and 99.5%. As the relative optical

densities plotted in the Fig. 9 were measured using polished specimen cross-sections, the observed higher optical densities can be associated with the masking of some of the defects (pores and cracks) during metallographic preparation. Hence, to account for all the porosity and cracks, a more detailed analysis was conducted on lightly etched specimen cross-sections and considerable attention to detail was directed to confirming and differentiating cracks from solidification structures, as revealed in Fig. 8b, where at low magnification, the region delineated by the white dashed rectangle appears to a have crack-like feature, but an enlarged image of this rectangle-delineated region (inset (c)) clearly shows that this solidification feature is not a crack. The number of cracks and crack density (total crack length/area) was calculated for each specimen using the image processing software ImageJ. Contour maps showing the number of cracks and crack density as a function of power and scanning speed were generated using the measured data and are shown in Fig. 10. As observed in these contour maps, the crack density is highest at higher power levels between 180 and 200 W, and scan speeds less than 900 mm/s, even though the number of cracks is not. As such, this parameter window seems to generate large cracks that are continuing across multiple layers. Also, with increasing speed in this power range, an increase in the number of cracks is apparent, while the crack density remains unchanged. Hence, the increase in the speed at higher power ranges, results in a higher number of cracks that are shorter in length. The contour maps also show that at lower power values (i.e., below 160 W), the scan speed range applied in this study doesn't affect the number and density of the cracks. A decrease in the cracking tendency was observed as the power was decreased for all scan speeds, and cracking was eliminated for the specimens fabricated using 140 W power. It is also worth noting that when the power is reduced below 140 W, lack of fusion defects are observed instead of the cracks.
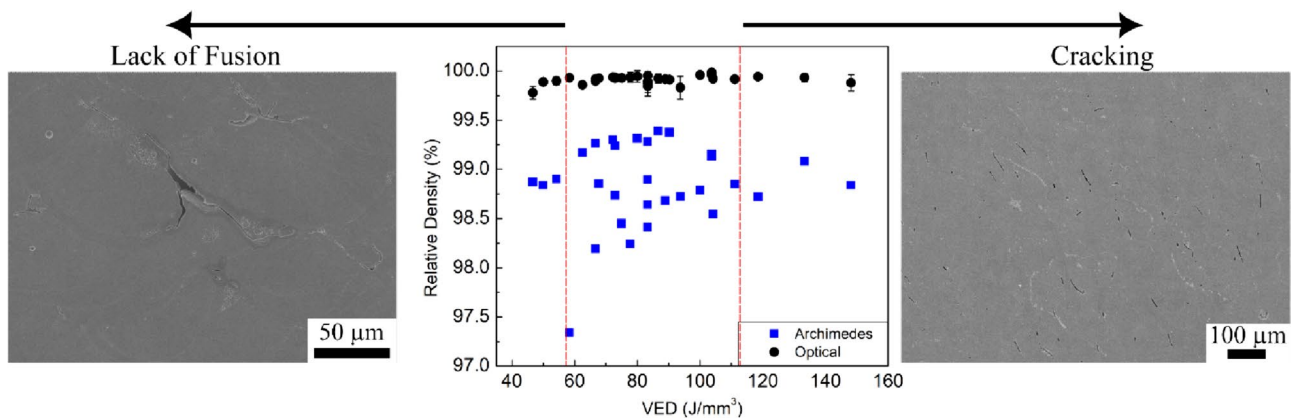

Fig. 9 The relative density of LPBF AB CoCrFeMnNi specimens as a function of VED and representative micrographs of the common defects
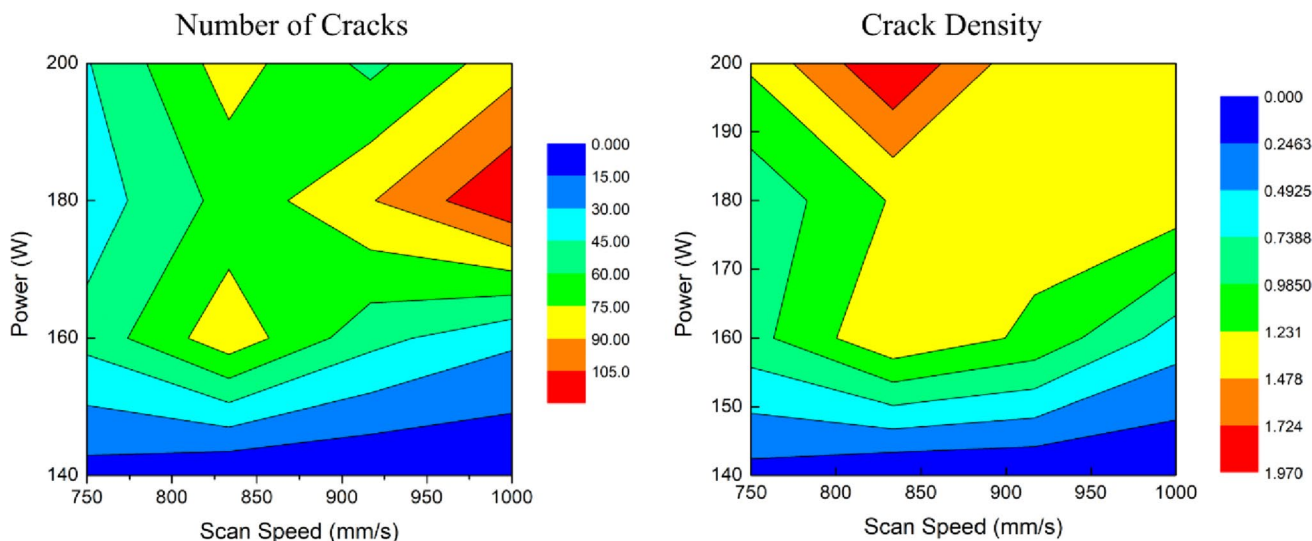
Fig. 10 Contour maps, that show the number of cracks and crack density in LPBF AB CoCrFeMnNi as a function of power and scan speed

For this reason, the specimens fabricated with that power range (i.e., below 140 W) are not included in the contour maps given in Fig. 10.

Sun et.al [59] studied the hot cracking mechanism in CoCrFeNi alloy and showed that the residual stress induced by the thermal shrinkage during solidification caused cracking at the end stage of solidification. They suggested that the cracking susceptibility of this alloy reduces as the grain size decreases, since there are more grain boundaries to withstand the residual stress [59]. For LPBF-fabricated alloys, it is known that grain morphology is affected by the melt pool geometry and their overlapping, since the grains grow towards the center of the melt pool [60, 61]. As the melt pool shape becomes deeper and narrower, the grain morphology becomes more directional and columnar. Hence, the grain boundary area is decreased. To investigate this effect on the CoCrFeMnNi alloy, the melt pool width and depth of each specimen condition were measured using a line intercept method. The change in the melt pool geometry as a function of VED is shown in Fig. 11a along with a schematic representation of melt pools showing the change in their shape. It is noticeable that as the VED increases, the width to depth
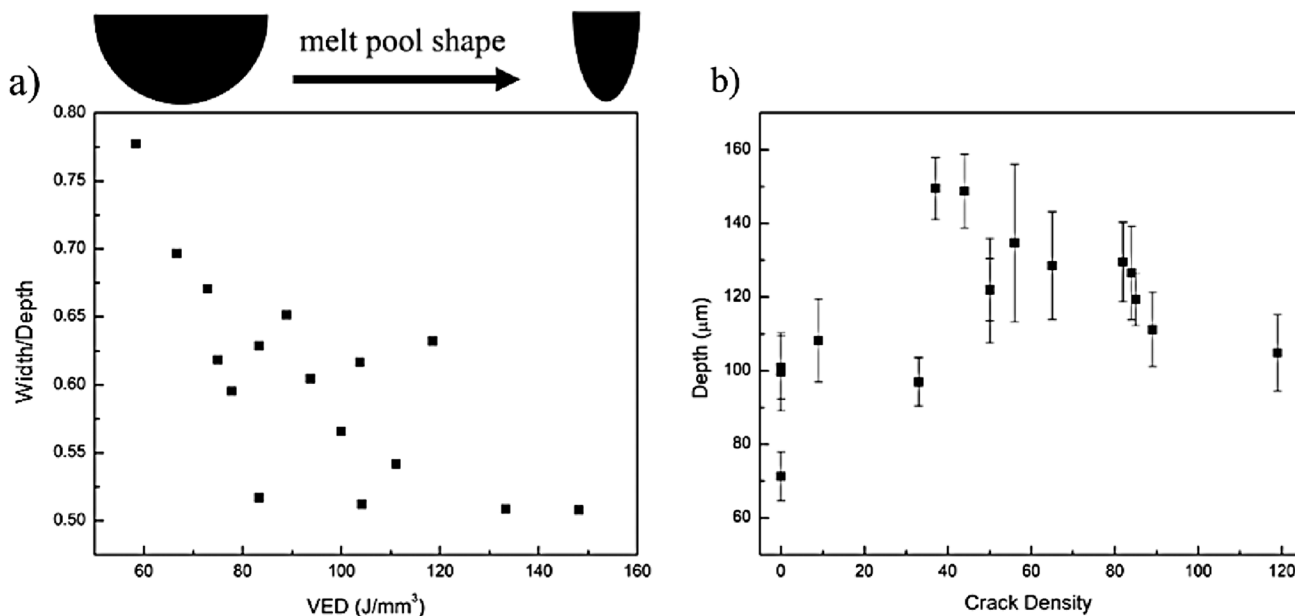

Fig. 11 Effect of **a** VED on melt pool shape and **b** melt pool depth on the crack density of LPFB-fabricated CoCrFeMnNi

ratio of the melt pools decreases. This change in the melt pool shape in turn results in a more columnar grain morphology with long grain boundaries along the BD, which are susceptible to crack formation and propagation. The effect of melt pool depth on the crack density, as plotted in Fig. 11b, also supports this observation of a significant increase in the crack density, once a certain melt pool depth is surpassed.

As-Built Microstructure

After this systematic parameter optimization study using 5 mm cube specimens, the optimal parametric conditions were selected considering the surface roughness, density, and crack density. For the $5 \times 5 \times 5$ mm^3 specimen size, a VED of 73 J/mm^3 resulted in the fabrication of a crack-free specimen with the highest density (~99.5%), whilst with a VED of 104 J/mm^3 the surface roughness and crack density were lowest among the cracked specimens. Hence, these two conditions were selected for further characterization and scaling to the larger specimen dimensions of $10 \times 10 \times 10$ mm^3.

EBSD analysis was conducted to characterize the grain morphology and texture of the LPBF AB CoCrFeMnNi specimens. Figure 12 shows the IPF orientation maps of selected specimens along with the corresponding pole figures obtained from the cross-section of the cubes parallel to the BD. Grain boundaries are denoted with solid black lines for high-angle grain boundaries having misorientations higher than 15°. The IPF orientation map given in Fig. 12a for the 5 mm cube specimens fabricated with a VED of 73 J/mm^3 reveals a mixture of equiaxed and columnar grain structures mainly along the <110> direction. However, there is no strong texture observed in this specimen with a multiple of uniform density (MUD) of 3.02. This is also evident from the measurement of the average length of the grains, which was, respectively, ~59 μm and ~25 μm parallel and perpendicular to the growth direction.

When the VED is increased to 104 J/mm^3, for the same specimen size, the observed solidification structure becomes predominantly columnar, as shown in Fig. 12b. The average length of the grains increased to ~112 μm in the growth direction, but remained nearly unchanged (~26 μm) perpendicular to it. Epitaxial growth of the columnar grains for multiple layers along the direction of maximum thermal gradient is commonly observed for various alloys after LPBF processing [62–64]. The longitudinal axis of the columnar grains is predominantly oriented along the <100> direction, which is the preferential growth direction in FCC crystals [11, 65]. Niu et. Al. [61] also reported that the columnar grains extend for more number of layers as the VED increases. This is associated with the higher temperature at the bottom of the melt pools that promote epitaxial growth.

In addition to the VED, specimen geometry also affects the grain morphology and texture of the LPBF AB parts. Figure 12c, and d depict the IPF orientation maps for the $10 \times 10 \times 10$ mm^3 specimens fabricated at a VED of 73 J/mm^3 and 104 J/mm^3, respectively. For both VED values, a shorter long axis of the columnar grains can be seen with an average measured length in the growth direction of ~45 μm and ~97 μm for the 73 J/mm^3 and 104 J/mm^3 conditions, respectively. Perpendicular to their growth direction, the average grain size (diameter) for the $10 \times 10 \times 10$ mm^3 specimens remained comparable at ~24–26 μm for both VED values and unchanged relative to that observed for $5 \times 5 \times 5$ mm^3. The previously printed layers act as a heat sink during printing and generate the highest thermal gradient parallel to the BD. As the specimen size increases, heat accumulation at the bottom of the melt pool decreases due to both a larger scan vector and a larger heat sink. Hence, the extent of remelting and solidification of previous layers is shorter, resulting in a decrease in the columnarity of the grains. Additionally, for these specimens, both VED values resulted in a texture mainly along the <100> direction with MUD values close to each other. Thus, comparing the EBSD maps given in Fig. 12, the crystallographic orientation of the AB CoCrFeMnNi depends on the applied VED during LPBF AM; this finding was also observed by Niu et. al [61] over their VED range from 59 to 185 J/mm^3.

Further microstructural analysis was conducted for each of the selected specimen conditions. As shown in Fig. 13, regardless of the VED or specimen size, melt pool boundaries and cellular sub-grain structure are visible in the SEM micrographs. One thing that is worth mentioning specifically for these selected conditions is that the VED of 73 J/mm^3 results in the fabrication of crack-free specimens when the specimen size is $5 \times 5 \times 5$ mm^3 (Fig. 13a); however, an increase in the specimen size—to, for instance, $10 \times 10 \times 10$ mm^3—starts crack formation (Fig. 13c). By contrast, for the specimens fabricated using a VED of 104 J/mm^3, cracks are visible at the grain boundaries of the $5 \times 5 \times 5$ mm^3 specimen (Fig. 13b), whereas the $10 \times 10 \times 10$ mm^3 specimen is crack-free, as revealed in Fig. 13d. These findings indicate a strong sensitivity of the CoCrFeMnNi alloy to the thermal conditions during LPBF processing, and considering the cross-sectional geometry of the test specimens (i.e., 8×8 mm^2, 8×10 mm^2 and 26×48 mm^2), a VED of 104 J/mm^3 was chosen for their LPBF fabrication and characterization.

Phase Analysis

XRD analysis was performed to identify the phases present in the starting powder and LPBF-fabricated specimens. $5 \times 5 \times 5$ mm^3 specimens were used for this purpose. Figure 14 reveals the XRD spectrum of the pre-alloyed argon gas-atomized CoCrFeMnNi powder, as well as the selected
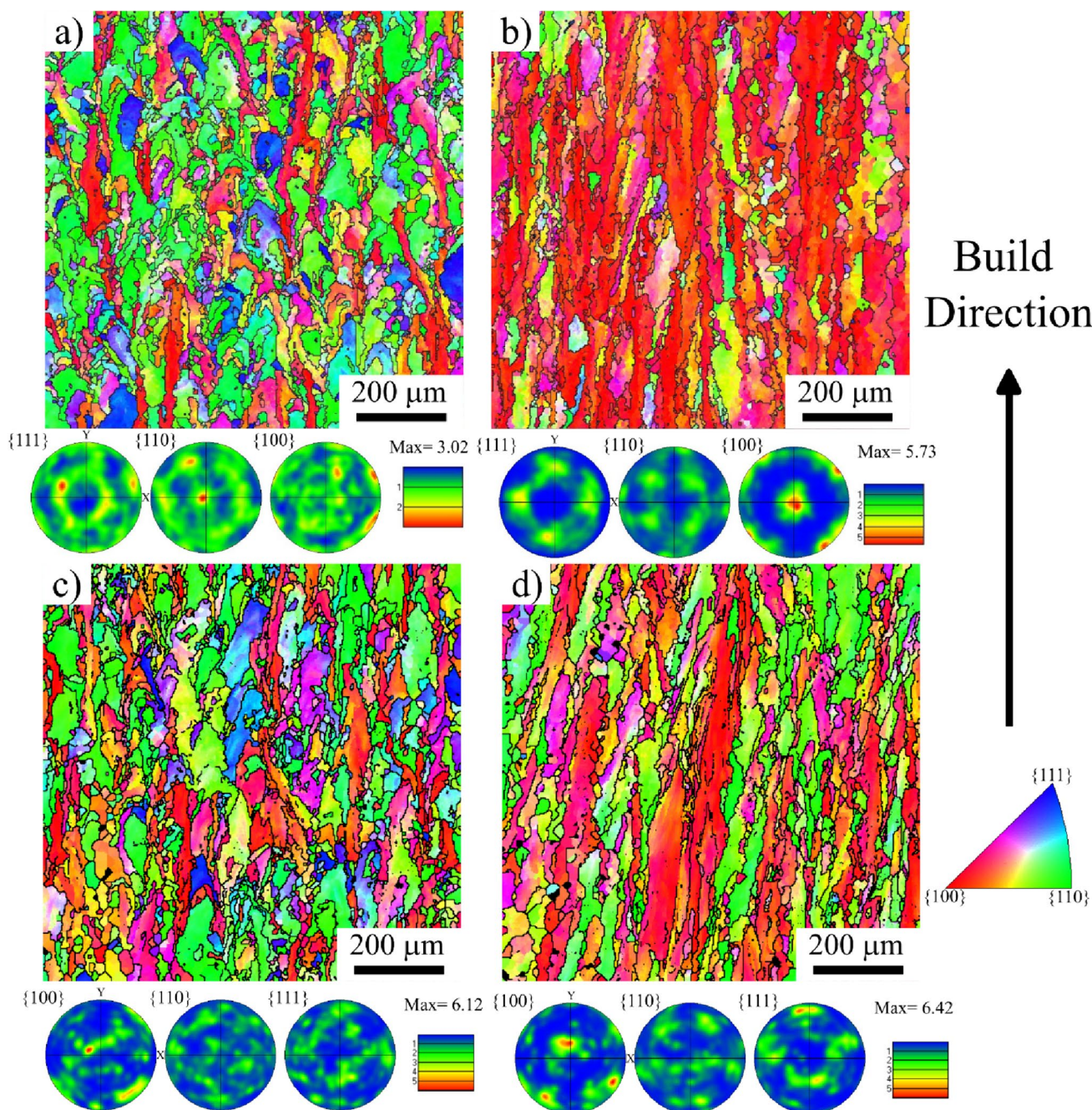
Fig. 12 IPF orientation maps and corresponding pole figures in the AB condition for 5 mm cube specimen with a VED of: **a** 73 J/mm^3, and **b** 104 J/mm^3; and 10 mm cube specimen with a VED of: **c** 73 J/mm^3, and **d** 104 J/mm^3

AB specimens with a VED of 73 and 104 J/mm^3. The XRD spectrum of the powder depicts a predominant FCC phase with diffraction peaks at 51.17°, 59.78°, 89.59°, 111.28°, and 119.07°. Also, the powder spectrum showed an additional secondary phase that couldn't be identified through the reference database associated with the diffractometer. Nevertheless, the EDS maps of the elemental distribution in CoCrFeMnNi powder, as given in Fig. 2, showed dendrites with enrichment of Fe, Cr and Co, as well as interdendrites enriched most predominately with Mn and, to a much lesser extent, Ni (that appeared reasonably well distributed). This was also observed by Laurent-Brocq et al. [66] when the solidification rate is not fast enough for the solid solution to be attained. Previously Wang et al. [10] also examined their pre-alloyed argon gas-atomized CoCrFeMnNi powder using EDS mapping and found a well-defined dendritic structure
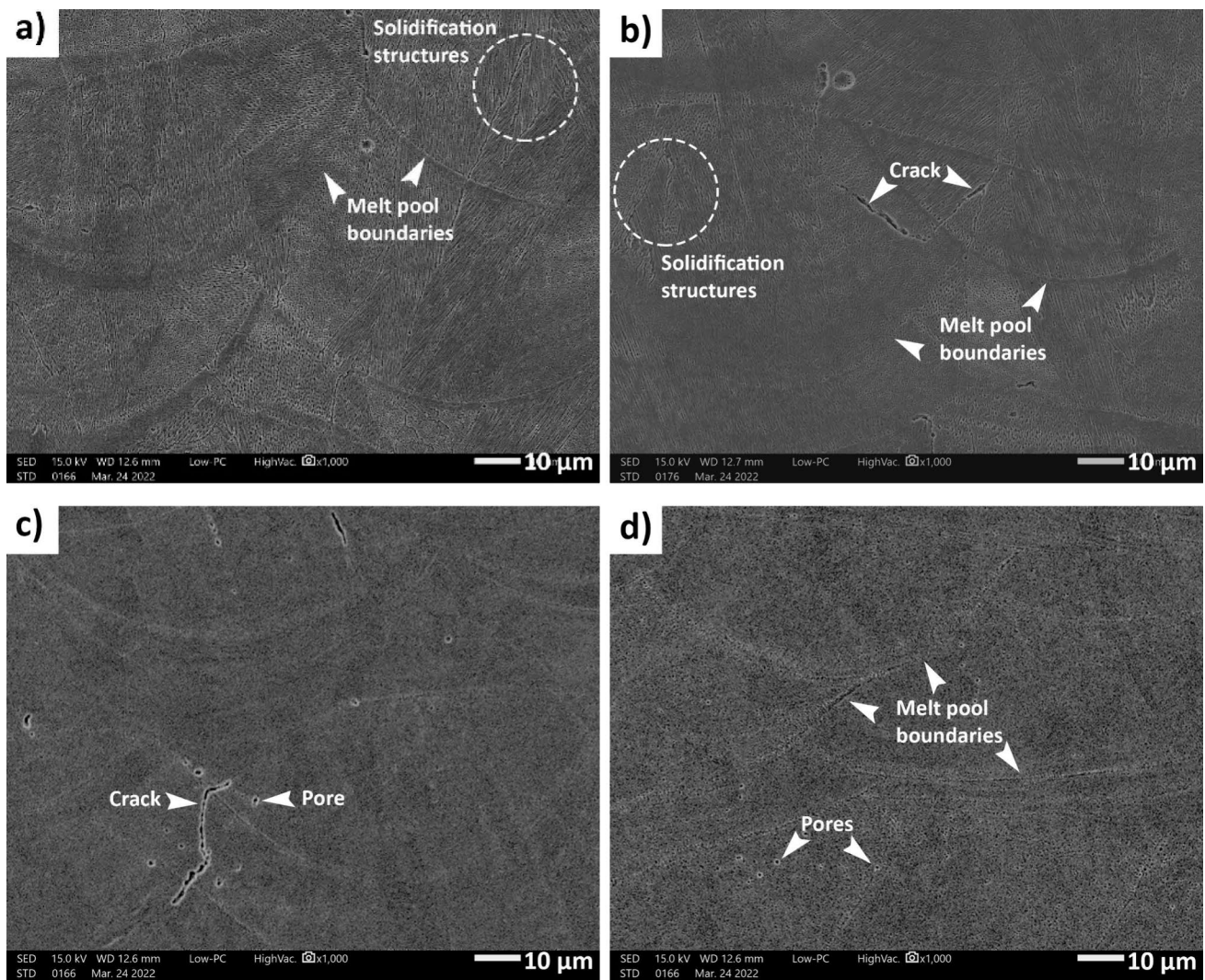
Fig. 13 SEM micrographs of AB 5 mm cube specimens at a VED of: **a** 73 J/mm^3 and **b** 104 J/mm^3; and 10 mm cube specimens at a VED of: **c** 73 J/mm^3 and **d** 104 J/mm^3

with both Mn and Ni segregated into the interdendritic regions and the dendrites enriched in Fe, Cr, and Co. These findings indicate that during solidification of the CoCrFeMnNi powder after argon gas atomization, it is challenging to reach sufficient undercooling for directly solidifying the particles with a homogeneous and equimolar solid solution phase.

For the LPBF-fabricated specimens, XRD analysis revealed a single-phase FCC spectrum with diffraction peaks at 51.09°, 59.67°, 89.49°, and 111.28°. The simple FCC crystalline structure is typical when the CoCrFeMnNi alloy solidifies in its stable state as an equimolar solid-solution phase. The specimen fabricated with 73 J/mm^3 VED had a predominant (111) texture, while the 104 J/mm^3 specimen had a (200) texture. This observation is also in agreement with the EBSD analysis discussed in the previous section.

To understand the phase transformations occurring during heating and determine the melting point of the CoCrFeMnNi alloy, DSC analysis was conducted for the powder and the LPBF specimen fabricated at a VED of 104 J/mm^3, both in the AB and HIPed conditions. Specimens were heated up to 1500 °C with a heating rate of 20 K/min to capture the whole melting range and the results are shown in Fig. 15. Both specimens showed an endothermic peak corresponding to the melting of the CoCrFeMnNi alloy. The onset of melting for the powder and the LPBF AB and HIPed specimens was 1281 °C, 1291 °C and 1310 °C, respectively. Hence, the melting point of the LPBF AB and HIPed specimens is slightly higher compared to the powder. These results agree well with the liquidus and solidus temperatures of 1340 °C and 1290 °C measured by Laurent-Brocq et al. [66] for CrMnFeCoNi.

Fig. 14 XRD spectrum of the starting powder and AB CoCr-FeMnNi specimens fabricated by LPBF with a VED of 73 and 104 J/mm^3
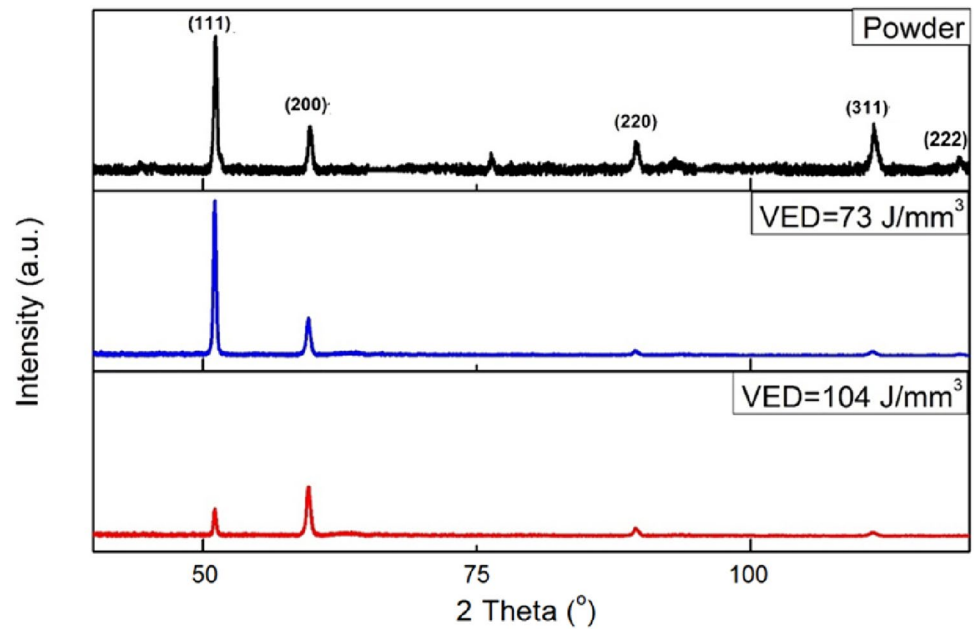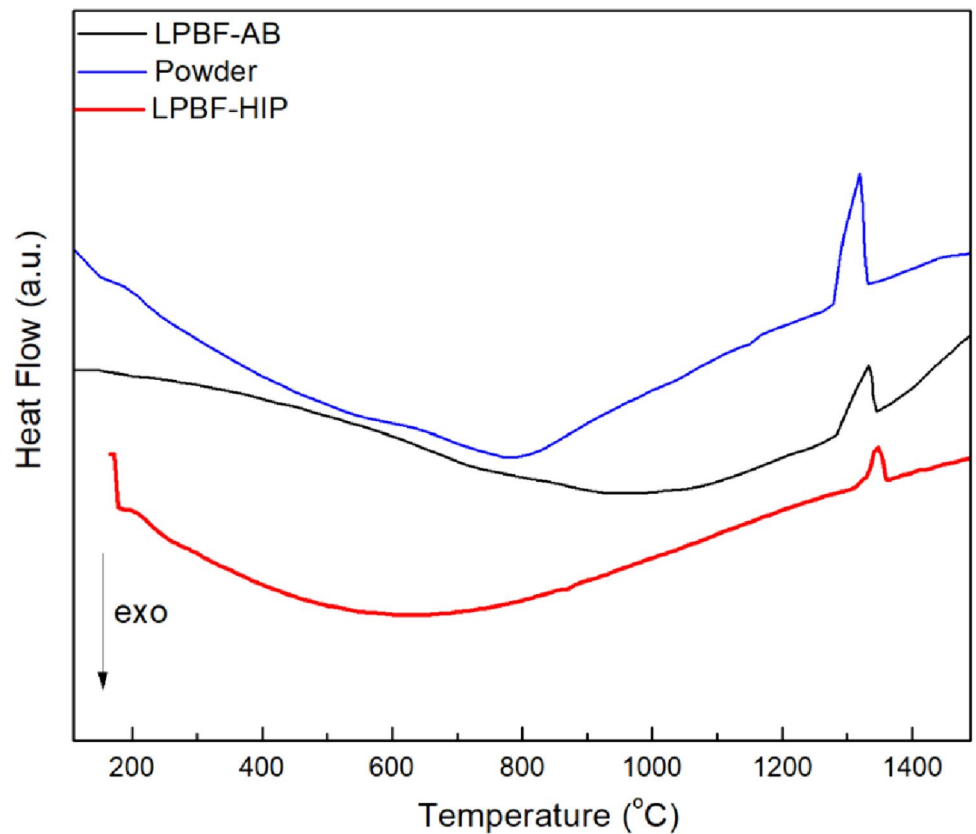

Fig. 15 DSC curves for the CoCrFeMnNi powder and LPBF AB specimens

Microstructure After HIP

After optimization of the LPBF parameters, a select number of test specimens fabricated using a VED of 104 J/mm^3 (and having a density of > 99.5%) were subjected to HIP to further densification and closure of any remaining micropores in the bulk material after LPBF processing. The IPF orientation map and SEM micrograph of the HIPed specimen in Fig. 16 show the presence of equiaxed grains with
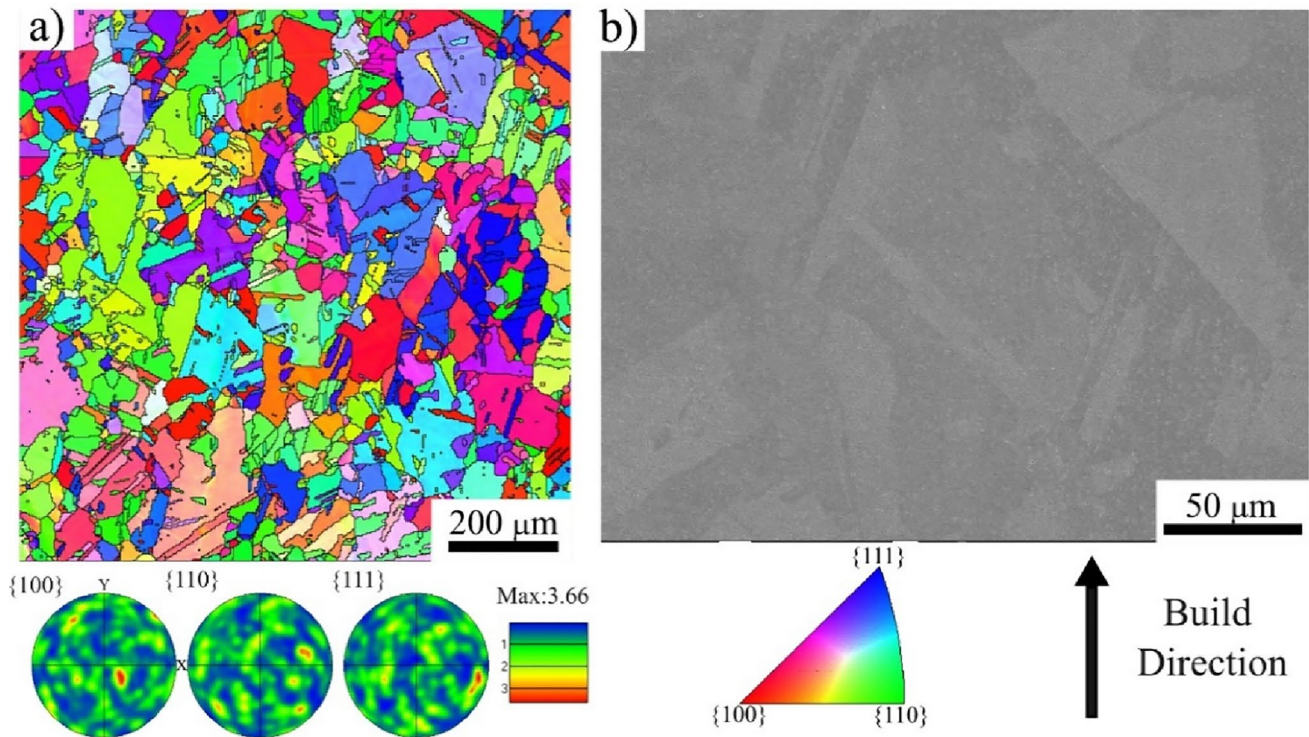
Fig. 16 **a** IPF orientation map and **b** SEM micrograph of the LPBF AB and HIPed CoCrFeMnNi alloy

annealing twins. Therefore, the applied HIP cycle resulted in the recrystallization of the columnar grains that were observed in the AB condition. The recrystallized grains with average size of ~ 46 μm have no specific crystallographic orientation, as can be seen in the IPF orientation map and corresponding pole figures. The SEM micrograph of the HIPed specimen in Fig. 16b also reveals the dissolution of the cellular sub-grain structure of the AB specimen.

Considering the test specimen geometries used in the present study, the VED condition of 104 J/mm^3 was most relevant for detailed investigation of the density to characterize the nature of the porosity by μCT, which could then provide insight for the analysis and understanding of mechanical properties. For this purpose, representative samples from test specimens built horizontally and vertically at 104 J/mm^3 VED were selected for μCT analysis.

X-Ray μCT Inspection of AB and HIPed CoCrFeMnNi

To understand the morphology, size distribution and volume of the pores in the AB and HIPed CoCrFeMnNi, high magnification X-ray μCT scans of the test specimens were acquired and analyzed. The 3D visualization reconstruction of the size and distribution of the pores is depicted in Fig. 17a, b and c for representative horizontal and vertical specimens in the AB condition. The highest volume and size of pores was observed near the specimen surface as illustrated in Fig. 17a. Within the

bulk material, the vast majority of the internal pores in both the horizontal and vertical AB specimens appear to be isolated with typical characteristics of gas-induced porosity, featuring nearly spherical-shaped pores that are relatively small in size, as seen in Fig. 17b and c. These micropores likely arose from entrapped gas bubbles in the original pre-alloyed CoCrFeMnNi powder (as revealed in Fig. 2) produced via the argon gas atomization process and/or the printed specimen as a result of the inert argon atmosphere in the LPBF process [52, 67–69].

The pores in the bulk volume are randomly distributed and Fig. 17d gives their size distribution in the horizontal and vertical AB specimens. No pores were observed (using a 2.5 μm voxel size) in the horizontal and vertical specimens after HIP, but some residual cavities, roughly 30–50 μm in depth, were evident on the surface, as shown in Fig. 17e. Quantitative analysis indicated a greater volume of smaller pores (15 μm to 30 μm) and a lower volume of coarser pores (35 μm to 50 μm) in the horizontal AB specimen compared with the vertical AB specimen. Also, the porosity content was lower in the AB specimens that were built horizontally (0.007%) relative to those built vertically (0.01%). As well, the vertical AB specimen showed a higher number of total defects (680) compared to the horizontal one (379) for the same analyzed volume. From these results, the calculated average defect size was 13.4 μm and 25.9 μm in the horizontal and vertical AB specimens, respectively.
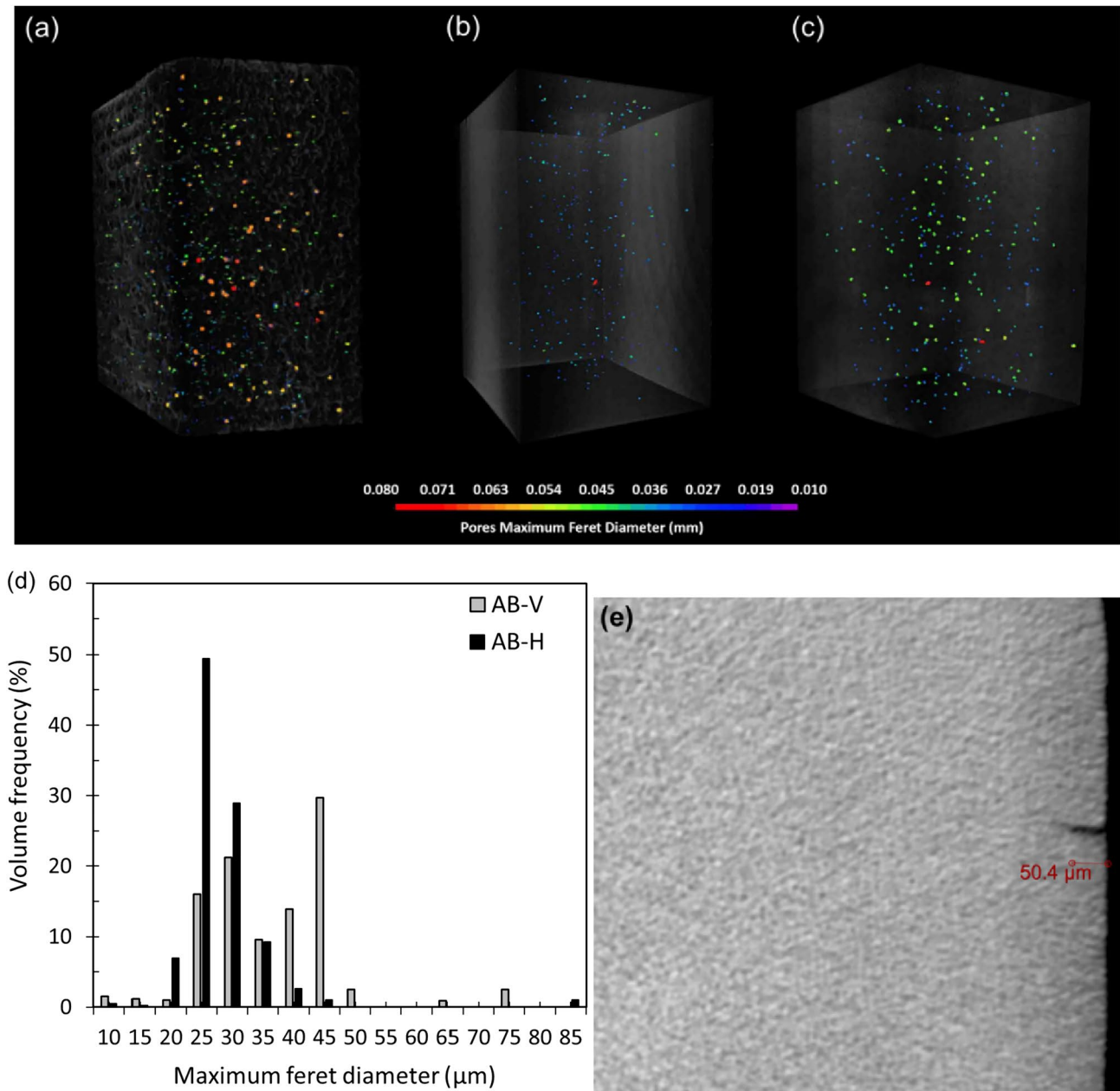
Fig. 17 Representative images from X-ray μCT scans of the test specimens built **a** horizontally showing surface pores, **b** horizontally and **c** vertically showing internal pores, **d** the size distribution of internal pores, and **e** small remnant surface cavities and absence of internal pores in the HIPed condition (horizontal specimen is shown)

Mechanical Properties

Effect of Process Parameters on Hardness

Microhardness measurements were conducted on each specimen manufactured for parameter optimization and compared to each other with respect to their VED values. The average microhardness value for each specimen is shown in Fig. 18 along with the microhardness range

reported in the literature for LPBF AB CoCrFeMnNi, which is designated by the red dashed lines [70]. The microhardness measurements revealed that all the specimens within the process parameter range utilized in this study have a statistically similar average microhardness value. It is also worth noting that these values are within the range of the reported values in the literature [70]. The main difference between the specimens fabricated with different VED values is the variation in the microhardness values, which may have been exacerbated by remnant
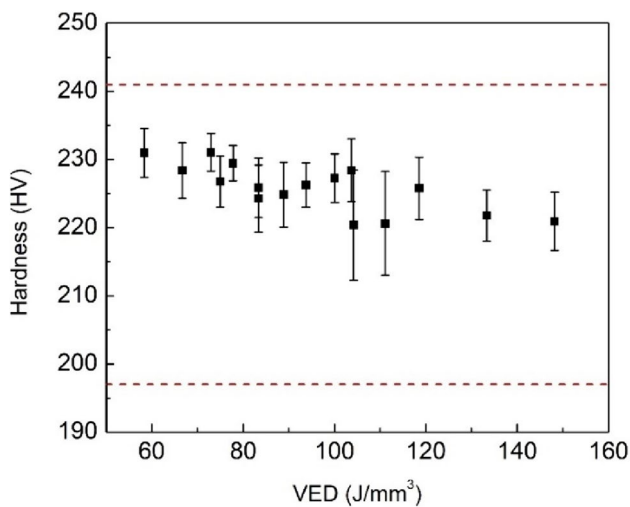
Fig. 18 Average microhardness values as a function of VED values for LPBF AB CoCrFeMnNi (Data includes both $5\times5\times5$ mm^3 and $10\times10\times10$ mm^3 cube specimens. Red dashed lines represent the microhardness range reported in the literature.)

micro-pores and micro-cracks in the specimens fabricated under non-optimal LPBF processing conditions.

Effect of Build Direction and HIP on Hardness

Microhardness measurements were conducted on test specimens fabricated with the optimum process parameters (VED of 104 J/mm^3) both in AB and HIPed conditions. The average microhardness value for the AB condition was calculated as 229 ± 5 HV and this value decreased to 152 ± 4 HV after HIP. The lower hardness observed for the HIPed CoCrFeMnNi can be attributed to the recrystallization of the columnar grains and the dissolution of the cell boundaries (Fig. 16) that were present in the LPBF AB condition (Figs. 8 and 12). Cell boundaries are often reported to contribute to the dislocation strengthening of LPBF-fabricated parts as the cell walls have extremely high dislocation densities due to the rapid heating and cooling cycles during processing [11, 71].

Tensile Properties

To assess the effect of the BD and HIP on the mechanical properties of the LPBF-fabricated CoCrFeMnNi alloy, uniaxial tensile tests were conducted on the vertically and horizontally oriented specimens both in the AB and HIPed conditions. The engineering and true stress–strain diagrams of a representative specimen for each condition are shown in Fig. 19a and b, respectively, and the average values for the YS, UTS, global and local ε_f, and T_M are given in Table 5. The specimens showed a strong anisotropy in the AB condition. As revealed in the stress–strain diagrams, the horizontal

AB specimen has higher strength and elongation values compared to the vertically built one. Also, relative to the average tensile strength properties in the vertical direction (YS of 510.3 ± 14.5 MPa and UTS of 571.1 ± 14.8 MPa), the values in the horizontal direction (YS $= 601.3\pm17.1$ MPa and UTS $= 689.2\pm5.6$ MPa) were 17.8% and 20.7% higher, respectively, for the YS and UTS. This can be associated with crystallographic texture and grain morphology. For instance, Dovgy *et. al*. [11] also reported similar results for LPBF-fabricated CoCrFeMnNi alloy. They observed that their horizontally built specimens showed a higher Taylor factor value compared to vertically built specimens, resulting in a higher yield strength. Additionally, Kim *et. al* [21] observed the same trend in the Taylor factor and yield strength between the two directions during compressive deformation of LPBF-fabricated CoCrFeMnNi alloy.

The global ε_f values (obtained from the extensometer measurements), as presented in Table 5, were nearly 60% higher for the horizontal AB specimens ($25.9\pm2.9\%$) compared to the vertically built ones ($16.3\pm1.3\%$). A similar trend is apparent for the local ε_f (obtained through DIC with the Aramis® system) with higher average values (by ~7%) for the horizontal AB specimens ($77.3\pm11.1\%$) compared to the vertically built ones ($72.0\pm10.7\%$). Figure 20a and b provides the results from a more detailed examination of the strain distribution within the gage section of representative horizontal and vertical specimens in the AB condition just before tensile fracture using the DIC technique. In this figure, the tensile loading direction is parallel to the vertical direction of the images, and the color-coded strain map on the entire gage section of the specimens corresponds to the value of normal strain in the tensile direction. The region of strain localization, indicated as the area of highest intensity in the tensile specimen gage section, corresponds to the location of the fracture that occurred immediately afterward. While it can be seen that in the horizontal AB specimen the average strain is about 22%, rising to more than triple that at the eventual fracture location, the localization is much more pronounced in the vertical AB specimen, with an average strain in the majority of the CoCrFeMnNi of only around 10%. This rises sharply to 72%, over seven times the average value, at the fracture location. The difference in the average ε_f values (global and local) for the two BDs studied can be related to the slightly lower porosity and smaller pores in the horizontal AB specimens, compared to those built vertically, as discerned from the micro-CT results (Fig. 17). Also, the presence of molten pool boundaries and any micro-cracks perpendicular to the loading direction in the vertical specimen can act as crack initiation and propagation sites during deformation that would predispose the vertically built specimens to lower strength and elongation compared to those built horizontally.
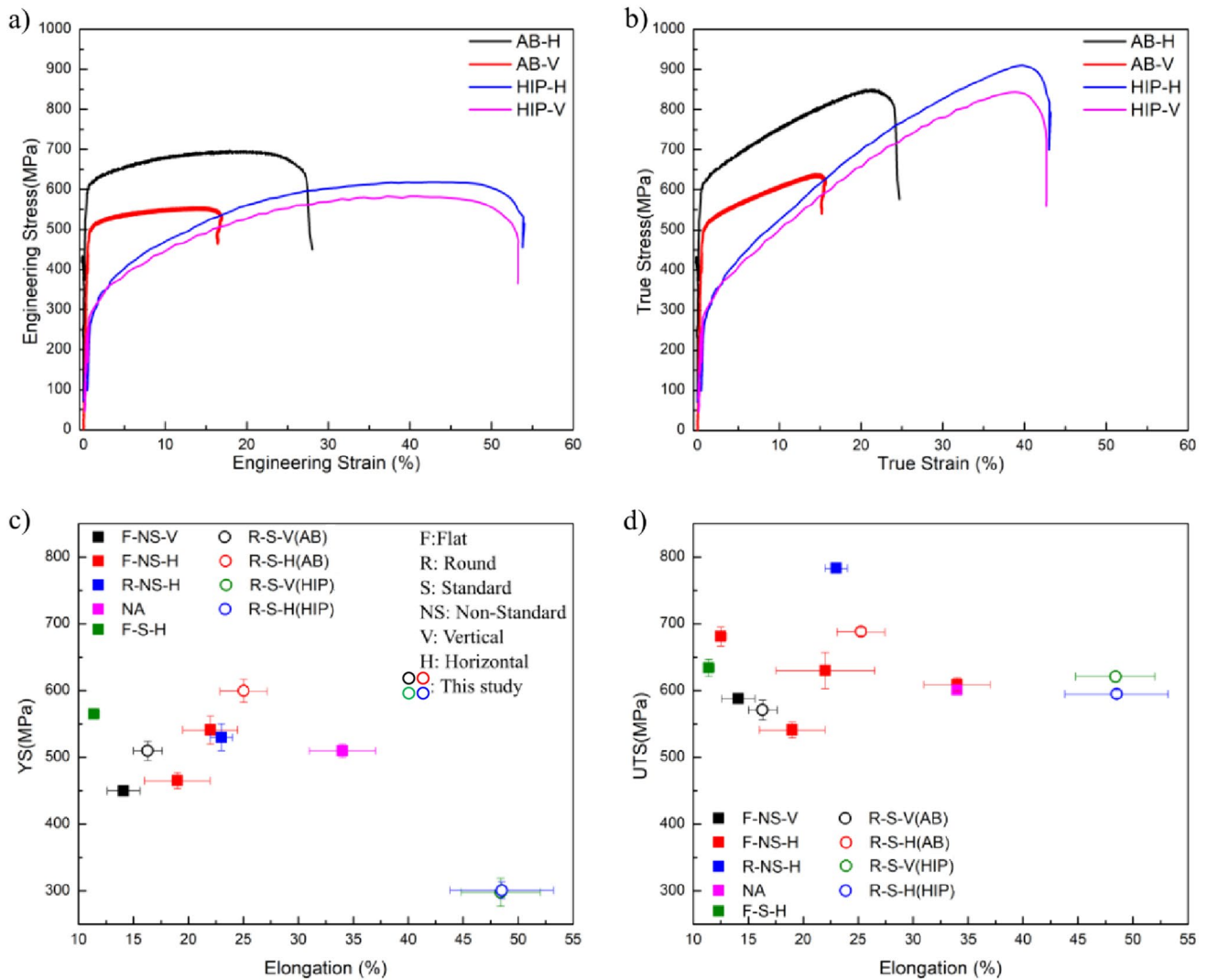
Fig. 19 **a** Engineering, **b** True stress–strain curves for LPBF-fabricated CoCrFeMnNi alloy in AB and HIPed conditions for two different BDs and their comparison to literature data in terms of **c** YS versus elongation and **d** UTS versus elongation [11, 14–16, 19, 25, 43, 52] (The results from reported literature are depicted by filled square markers whereas the results obtained in this study are plotted as open circles)

Table 5 Tensile properties of the AB and HIPed CoCrFeMnNi specimens

Property	AB—Horizontal	AB—Vertical	HIPed—Horizontal	HIPed—Vertical
YS (MPa)	601.3 ± 17.1	510.3 ± 14.5	297.8 ± 20.6	300.7 ± 12.7
UTS (MPa)	689.2 ± 5.6	571.1 ± 14.8	620.9 ± 7.8	595.0 ± 5.6
Global ε_f (%)	25.9 ± 2.9	16.3 ± 1.3	48.4 ± 3.6	48.5 ± 4.7
Local ε_f (%)	77.3 ± 11.1	72.0 ± 10.7	91.8 ± 11.8	114.9 ± 12.5
T_M (MPa)	146.4	87.2	260.9	254.6

The stress–strain curves given in Fig. 19 also clearly show the greater ability of the horizontally built CoCrFeMnNi to withstand much more plastic strain than those built vertically. The calculated area under the entire stress–strain curves indicates that the T_M increases by nearly 70% from 87.2 MPa in the vertical direction to 146.4 MPa in the horizontal direction. Thus, horizontally built CoCrFeMnNi can absorb much higher amounts of strain energy before fracture, making LPBF parts designed with this orientation possibly better suited to withstanding unexpected overloading in service.
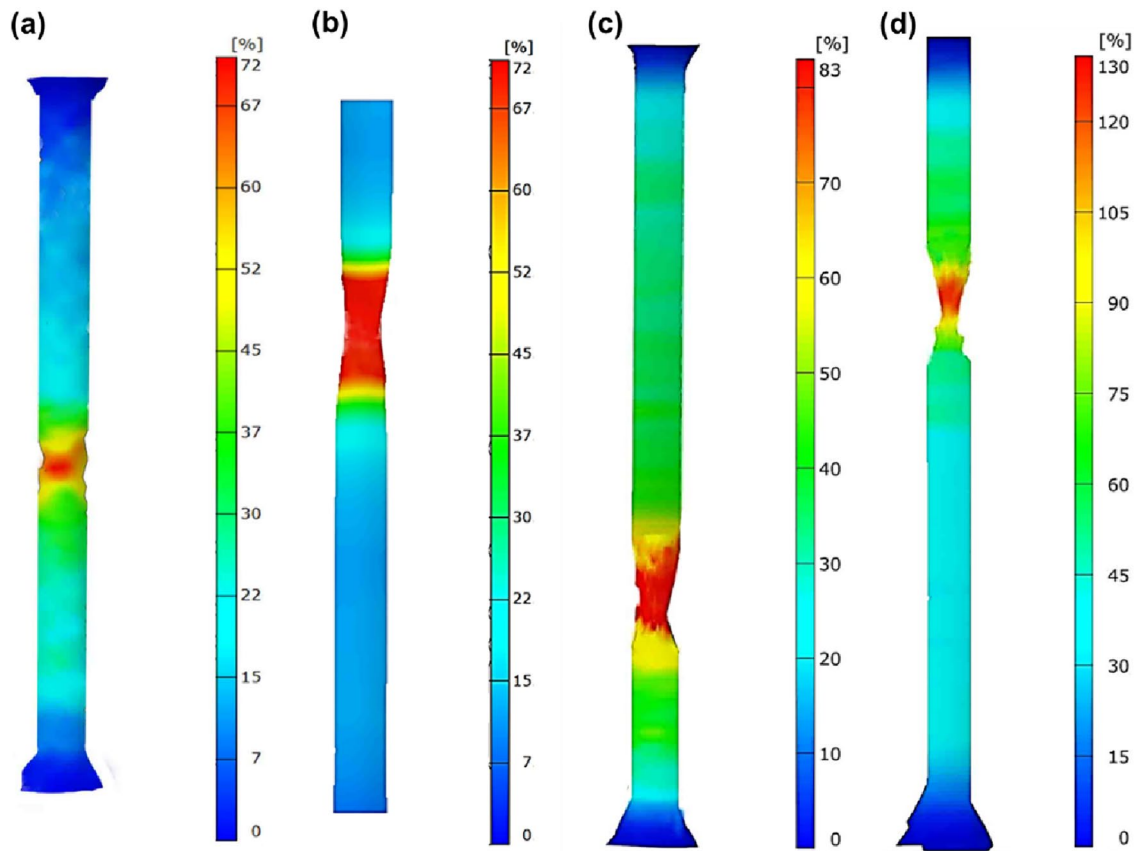
Fig. 20 DIC analysis of the local strain distribution maps on the tensile specimens just before fracture for **a** AB-horizontal, **b** AB-vertical, **c** HIPed-horizontal and **d** HIPed-vertical LPBF-fabricated CoCr-FeMnNi specimens. The color scale bar adjacent to each map denotes the local strain values (Color figure online)

After HIP, the observed anisotropy is reduced and the specimens built in both directions showed similar strength, elongation (global ε_f), T_M and strain localization behavior as indicated in Table 5 and Fig. 20c and d. The YS of both the vertical and horizontal specimens decreased by 41% and 50% after HIP. The UTS of specimens built vertically increased by 4%, while it decreased by 10% for specimens built horizontally. Similar to the hardness, the higher YS of the AB specimen may be related to the LPBF microstructure with cellular boundaries, where dislocation tangles are typically present. Hence the observed decrease in the YS of both the vertically and horizontally built specimens after HIP can be associated with the dissolution of these cell boundaries. Furthermore, after HIP, dissolution of molten pool boundaries and closure of defects, such as micro-porosity and micro-cracks, were observed microscopically (Fig. 16b) and through micro-CT analysis (Fig. 17). These combined with the recrystallization of the columnar grains reduced the microstructural anisotropy observed in the AB condition and resulted in similar tensile properties for both BDs after HIP. Moreover, relative to the AB condition, the ductility of both the vertically and horizontally built

specimens increased considerably with an increase of ~50% in the global ε_f and ~20% to 60% in the local ε_f, due to the closure of remnant defects during HIP. Also, from the strain distribution maps given in Fig. 20c and d, the average strain in the majority of the HIPed CoCrFeMnNi is around 40% for both the horizontal and vertical specimens and rises in a comparable way to more than double that at the eventual fracture location. This is can be further explained by examining the onset of localization from the strain distribution map captured at the end of the uniform deformation stage, as illustrated in Fig. 21a and b for representative horizontal specimens in the AB and HIPed conditions, respectively. There is a significant difference in terms of the plastic zone size with the strain concentrating over a more confined region in the AB specimen, whilst the plastic instabilities develop and spread more homogeneously in the HIPed specimen. Also, an earlier onset of strain localization is seen in the AB specimen at a strain value of about 20%, roughly half the value for the HIPed specimen. The improved ductility is also reflected in the increase of 80% and nearly 200% in the T_M value for the horizontal and vertical specimens, respectively, after HIP. The isotropic and high values of T_M
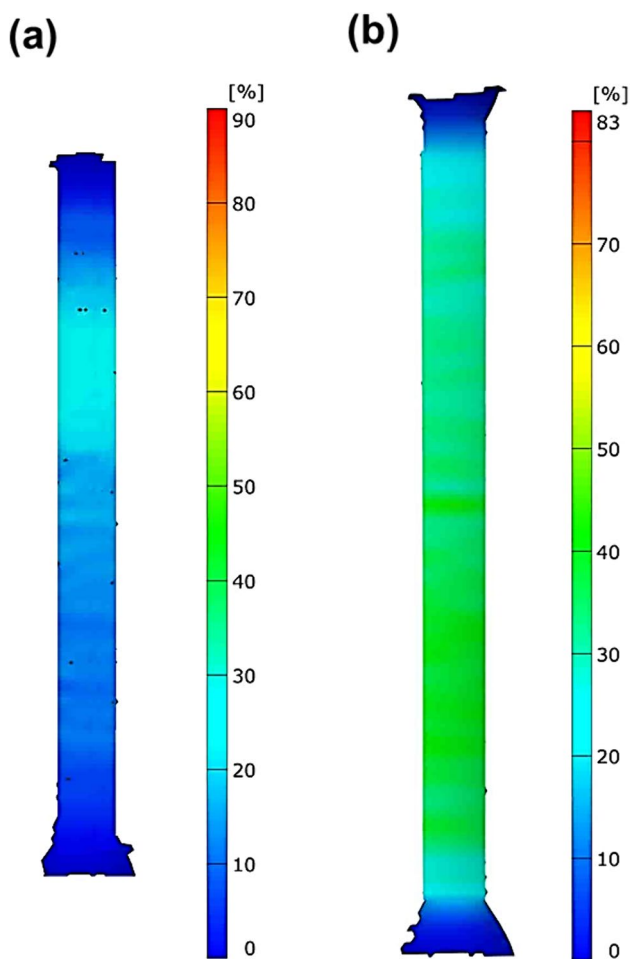
Fig. 21 DIC analysis of the local strain distribution maps on the horizontally built tensile specimens at the end of the uniform deformation stage for **a** AB and **b** HIPed conditions of the LPBF-fabricated CoCrFeMnNi. The color scale bar adjacent to each map denotes the local strain values (Color figure online)

indicate the considerably higher amount of energy per unit volume needed to completely fracture the LPBF-fabricated CoCrFeMnNi in the HIPed condition. Also, removal of the anisotropic mechanical response with post-process HIP may be desirable from a design perspective to allow flexible production of CoCrFeMnNi parts—that is, fabrication on different LPBF machines and/or in different build orientations still achieving the same properties, more akin to CoCrFeMnNi from conventional processing.

To compare these tensile properties with reported data in literature, the average YS, UTS, and elongation (i.e., global ε_f) values for each specimen condition studied in the present work were plotted together with reported values from previous research along with their corresponding specimen geometries (Fig. 19c and d). The results from the literature are depicted by closed square markers, whereas the results obtained in this present study are plotted as open circle markers. It is noteworthy that to the knowledge of the authors, this study is the first to evaluate the T_M and local ε_f of LPBF processed CoCrFeMnNi; so, no plots could be generated for these properties. The figures show that various specimen geometries and BDs have been tested for the LPBF-fabricated CoCrFeMnNi alloy; however, most of the tensile tests were conducted on flat specimens, which is in contrast to our study. It is worth noting that regardless of their BD, the round standard geometry specimens tested in the present study showed YS, UTS, and elongation values within the range of values previously reported in the literature [11, 14–16, 19, 25, 61, 72]. In fact, the horizontal AB specimens fabricated in the present study (red open circle) had the highest YS values relative to all the other specimens. Also, the vertical AB specimen (black open circle) showed both a higher YS and elongation compared to its close counterpart in literature (blue filled square). After HIP, despite the decrease in the YS, the UTS values are still within the range of the AB specimens reported in the literature. Moreover, the elongation values after HIP (open blue and green circles) are the highest values reported in the literature for the LPBF-fabricated CoCrFeMnNi alloy. Also, the room temperature tensile properties have been previously reported for conventionally processed CoCrFeMnNi; in the as-cast condition, Lam et al. [73] reported YS and UTS values of 194 MPa and 427 MPa, respectively, with an elongation of 92%. By contrast, though Kim et al. [74] reported similar strength properties, their observed elongation values were considerably lower, ranging from ~30–45%, depending on the loading direction. For wrought CoCrFeMnNi, Otto et al. [8] reported room tensile properties that depended on the grain size; for a microstructure with an average grain size of 50 µm, the YS and UTS values were about 200 MPa and 550 MPa, respectively, with an elongation ~60%. Thus, the tensile properties observed in the present study for LPBF-fabricated CoCrFeMnNi are showing higher strength values (YS and UTS) with slightly lower elongation in both the AB and HIPed conditions relative to the as-cast and wrought equivalent alloy, respectively. These findings are especially significant considering the capability of the LPBF technology to build complex geometry parts that can expand wider application of the CoCrFeMnNi alloy for structural applications, which typically have been limited due to the lower YS of this HEA when produced conventionally (cast and wrought). Also, considering that the finer LPBF microstructure gives improved tensile properties over coarser-grained cast CoCrFeMnNi, future research on post-process HIP that identifies conditions to minimize grain growth would likely reduce the YS drop, whilst providing isotropic tensile strength and ductility. Further research on the tensile properties of LPBF-fabricated CoCrFeMnNi (with and/or without post-process

HIP) at cryogenic and elevated temperatures would also provide insight for widening structural applications in different service environments.

Charpy Impact Properties

V-notch Charpy impact tests were also conducted for each specimen condition at room temperature and 77 K. The absorbed energy and Charpy impact toughness values for both temperatures are listed in Table 6. The results of the Charpy impact tests revealed a different trend compared to the tensile tests. The high energy fracture caused by the pendulum results in an overload of the sample. Due to the rapid nature of the fracture, work hardening is prevented. The absorbed energy and Charpy impact toughness of the vertical specimen is 35% higher compared to the horizontal specimen at room temperature. This could be associated with the grain orientation of the specimens. The impact is parallel to the grain boundaries in the horizontal specimen and perpendicular to the vertical specimen. Since the grain boundaries are more prone to fracture, the horizontal specimens can absorb less energy during an impact fracture. After HIP, the Charpy impact toughness of both horizontal and vertical specimens increased by 21% and 41%, respectively, due to the closure of the defects. Vertical HIPed specimens showed the highest impact toughness among all the specimens. However, the anisotropy in the Charpy impact toughness observed in the AB condition was preserved after HIP. The impact toughness for all specimen conditions showed a 20–27% decrease when tested at 77 K, yet no significant embrittlement was observed at cryogenic temperatures.

Fractography

Fracture surfaces of the specimens were investigated under a SEM after tensile testing and representative images are presented in Fig. 22. Low magnification images of the fracture surfaces show cup and cone type features for all the specimen conditions indicating that the fracture was ductile in nature. Spherical pores are observed on the fracture surfaces of the AB specimens regardless of the building orientation. However, when the two building orientations are compared, the size and fraction of these pores are clearly larger in the vertical specimen. The higher amount of larger defects observed in this specimen can be associated with the lower global and local ε_f, values recorded during tensile testing. In addition to the defects, large amounts of dimple colonies homogenously distributed throughout the fracture surface are also visible for both building directions, further verifying the ductile nature of the fracture. As shown in Fig. 22b and d, the majority of the porosity observed in the AB condition is eliminated after the specimens are subjected to HIP. The fracture surfaces of the HIPed specimens consists of fine dimples distributed throughout the fracture cross-section. There is no significant difference between the vertical and horizontal specimen orientations, which is consistent with the tensile test results.

Figure 23 shows the fracture surfaces of the broken halves of the Charpy impact test specimens. For each specimen condition tested at room temperature and at 77 K the unstable fracture region is marked by yellow dashed lines following ASTM E23 [48]. In these images, the right side of the surfaces are the V-notch and fracture initiation region next to the notch. The upper and lower sides of the yellow dashed lines are the shear lips and finally the left side of the marks is the final fracture region. All these regions located adjacent to the unstable fracture region are termed as the shear area, which is the area that absorbs the majority of the fracture energy during impact testing. Hence, the percentage of the shear area can be correlated with the impact toughness of the specimens. The shear area was calculated using image analysis methods for each specimen condition and is shown in Fig. 24. As seen in this bar chart, the shear area for the specimens tested at cryogenic temperatures is slightly lower compared to the specimens tested at room temperature. The vertical specimens showed a higher shear area compared to the horizontal ones, both in AB and HIPed conditions. Among all the specimens, the horizontal AB specimens showed the smallest shear area percentage, while the vertical HIPed specimen showed the highest. These trends are the same as the trends observed for the impact toughness of the specimens. Hence, shear area percentages successfully represent the impact toughness of the LPBF-fabricated CoCrFeMnNi alloy.

Table 6 Charpy impact properties of the CoCrFeMnNi specimens at RT and 77 K	Condition	Absorbed energy, RT (J)	Absorbed energy, 77 K (J)	Charpy impact toughness, RT (J/cm^2)	Charpy impact toughness, 77 K (J/cm^2)
	AB-H	9.3 ± 0.5	7.2*	27.8 ± 1.9	22.2*
	AB-V	14.5 ± 1.2	10.6*	43.1 ± 4.0	32.3*
	HIP-H	11.3 ± 0.3	8.2*	33.6 ± 1.2	24.5*
	HIP-V	20.3 ± 0.4	16.4 ± 0.1	61.1 ± 1.0	48.7 ± 1.1

*Standard deviation is not available

Fig. 22 Tensile fracture surfaces of the **a** AB-horizontal, **b** HIPed-horizontal, **c** AB-vertical, and **d** HIPed-vertical specimens
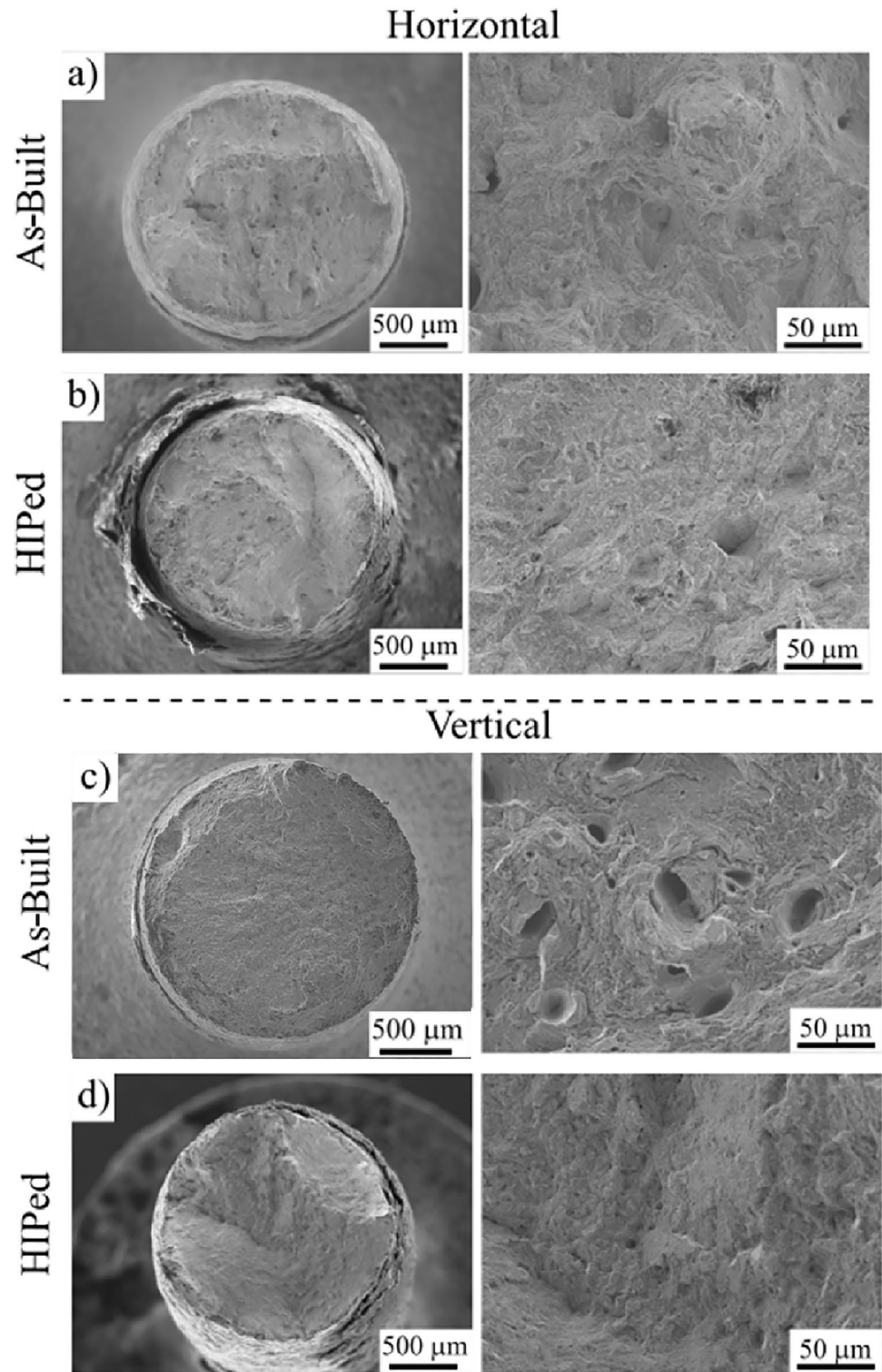

Figure 25 presents the higher magnification SEM images of the fracture surfaces of the Charpy impact specimens for each specimen and test condition. All the fracture surfaces mostly consist of fine dimples both at room temperature and at LN2 temperature suggesting ductile fracture for all the specimens. Similar to the tensile fracture surfaces, the AB specimens both in horizontal and vertical directions show porosity and cracking on their impact fracture surfaces independent of the test temperature. One significant difference worth noting is the presence of intact cellular sub-grain boundaries on the
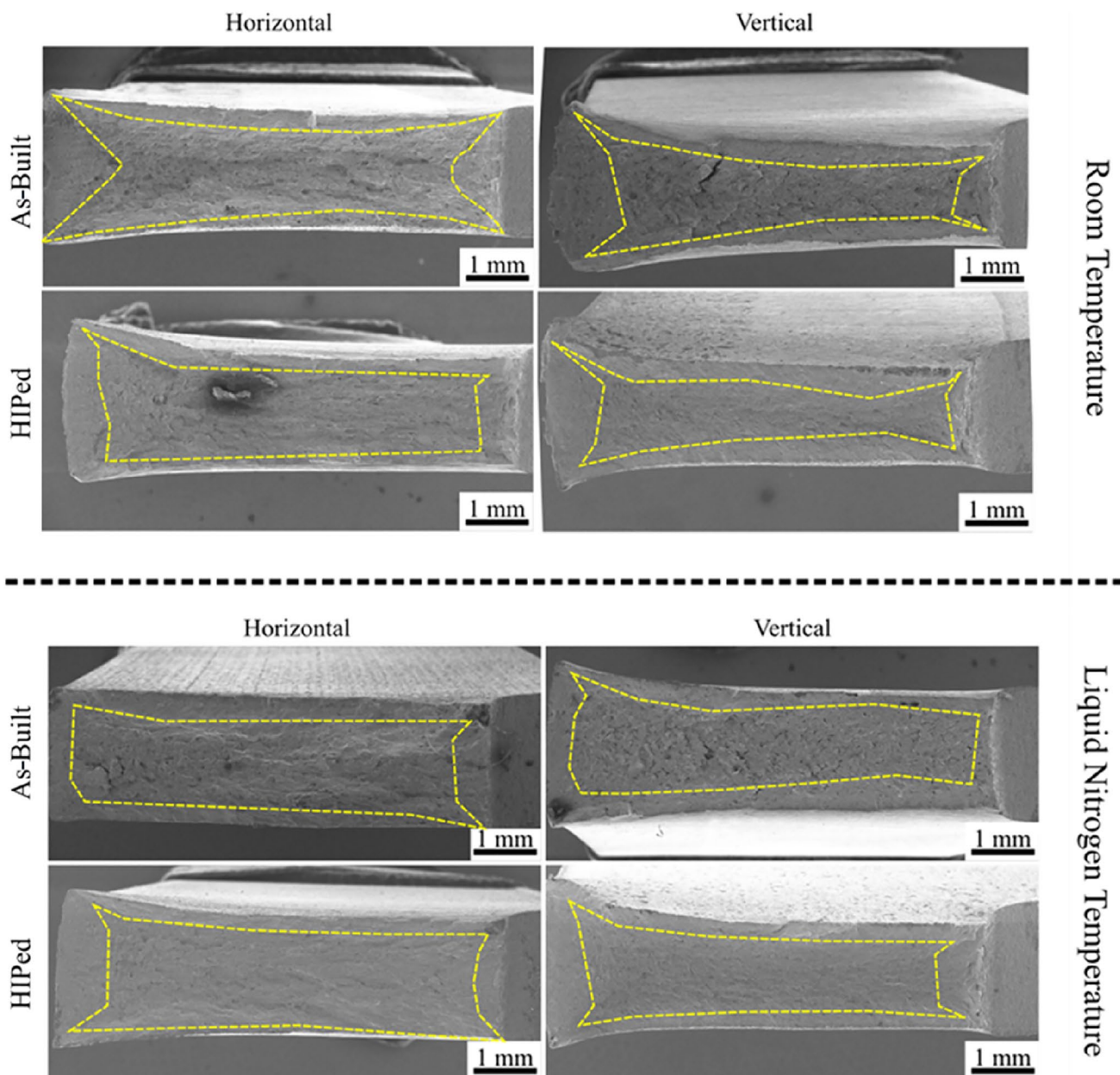
Fig. 23 The fracture surfaces of the broken halves of the Charpy impact specimens that were tested at room and liquid nitrogen temperatures. The unstable fracture region is marked by yellow dashed lines

fracture surface of the horizontal AB specimens for both test temperatures. This suggests that fracture occurred via crack propagation through the free surfaces of these sub-grain boundaries with little deformation. This observation is consistent with the lower impact toughness of the horizontal AB specimens both at room and LN2 temperatures. For the HIPed specimens, the amount of porosity and the cracks observed on the fracture surface is less compared to the AB conditions. This explains the improved fracture toughness for these specimens regardless of the testing temperature. Additionally, small equiaxed grains are also visible on some regions of the

fracture surfaces of the HIPed specimens corroborating with the recrystallized microstructure seen by EBSD (as given in Fig. 16), and fracture followed the boundaries of the small equiaxed grains in the recrystallized regions.

Wear Performance

To characterize the wear performance, low-stress abrasion testing was conducted on the AB and HIPed CoCrFeMnNi HEA, as well as wrought 316L stainless steel (SS) that served as a reference material and Table 7 lists its chemical

Fig. 24 The shear area percentage of the fracture surfaces of the Charpy impact specimens
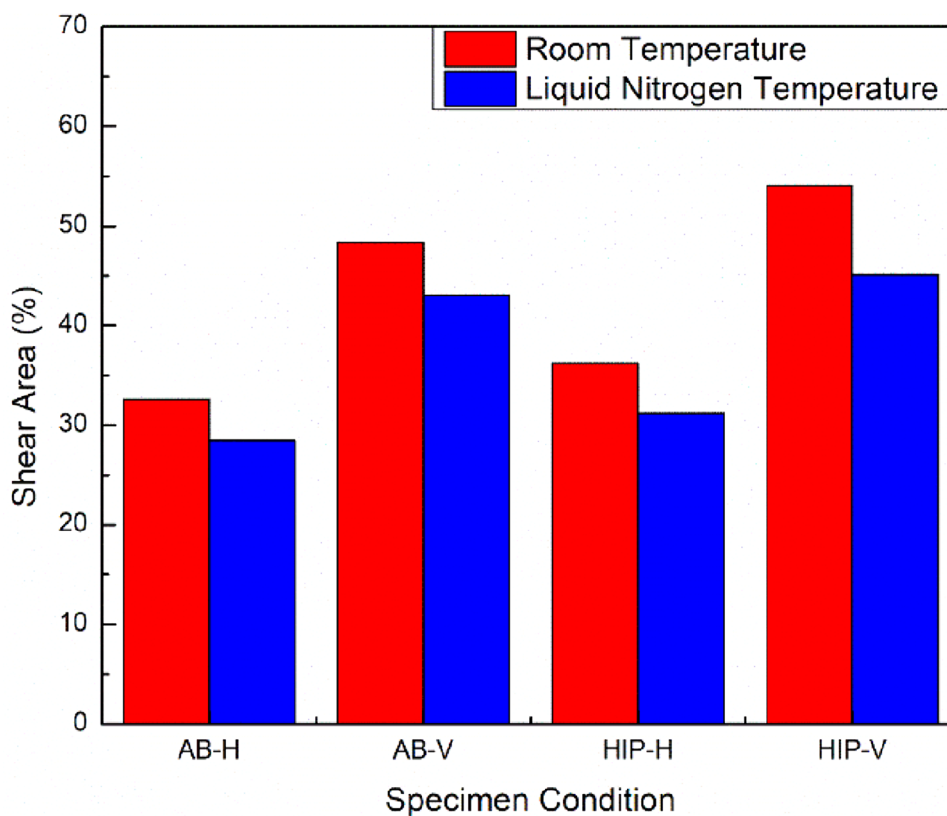
composition and properties. After testing, the wear volume loss from each specimen was measured using a laser profilometer. Figure 26 presents the profilometry images of the wear scars as a representative example. All of the evaluated materials underwent uniform material loss during abrasion.

The low-stress abrasion wear volume loss for the evaluated materials is shown in Fig. 27. Two wear tests were performed for each of these materials to ensure reproducibility, and the error bars in Fig. 27 represent the standard deviation of each measurement. As observed in the figure, both the AB and HIPed CoCrFeMnNi displayed approximately 11% better abrasion resistance than the reference 316L SS. Also, the AB CoCrFeMnNi exhibited the highest wear resistance among the evaluated materials. To the authors' knowledge, this study is the first to report the low-stress abrasion resistance of any high entropy alloy.

Figures 28, 29 and 30 show the SEM micrographs of the wear scars after low-stress abrasion testing of the 316L SS as well as the AB and HIPed CoCrFeMnNi, respectively. The direction of the abrasive follow is indicated by the arrow. In general, 316L SS exhibits ductile behavior, while both the AB and HIPed states of the CoCrFeMnNi HEA are slightly brittle in nature. As observed in Fig. 28a, and b, scratching and ploughing by the abrasive particles are the dominant wear mechanisms for 316L SS (parallel to the abrasive flow direction). There is also evidence of indentation and metal cutting by the sharp edges of the abrasive particles (Fig. 28c,

and d). 316L SS also displays plastic deformation, as seen in Fig. 28e, and f.

On the other hand, indentation and micro-fracture are the dominant wear mechanisms for the CoCrFeMnNi HEA (Fig. 29a, b and Fig. 30a, b). CoCrFeMnNi displays slightly higher micro-fracture/brittle behavior in the HIPed state compared to the AB condition. As observed in Figs. 29c, d and 30c, d, plowing by the abrasive particles also contributes to the total material loss rate. Additionally, there is evidence of metal cutting, as seen in Figs. 29e, f and 30e, f for the AB and HIPed CoCrFeMnNi, respectively. In some cases, abrasive sliding creates extruded lips at the end of the sliding path, which are then removed by the next abrasive particles, further contributing to the total material loss (Figs. 29f and 30f).

EDS mapping was conducted to identify the compositional behavior of the wear track. Figure 31a and b show the EDS mapping of the wear track for 316L SS and AB CoCrFeMnNi HEA, respectively, as representative examples.

As described above, scratching and ploughing parallel to the abrasive flow direction are the dominant wear mechanisms for 316L SS, while micro-fracture is the dominant mechanism for the HEA. Both 316L SS and CoCrFeMnNi undergo indentation by the abrasive particles, and the indents are rich in silicon (Si) and oxygen (O). It is interesting to note that, although there is a region in 316L SS enriched

Fig. 25 SEM micrographs of the fracture surfaces of the Charpy impact tested specimens at room and liquid nitrogen temperatures
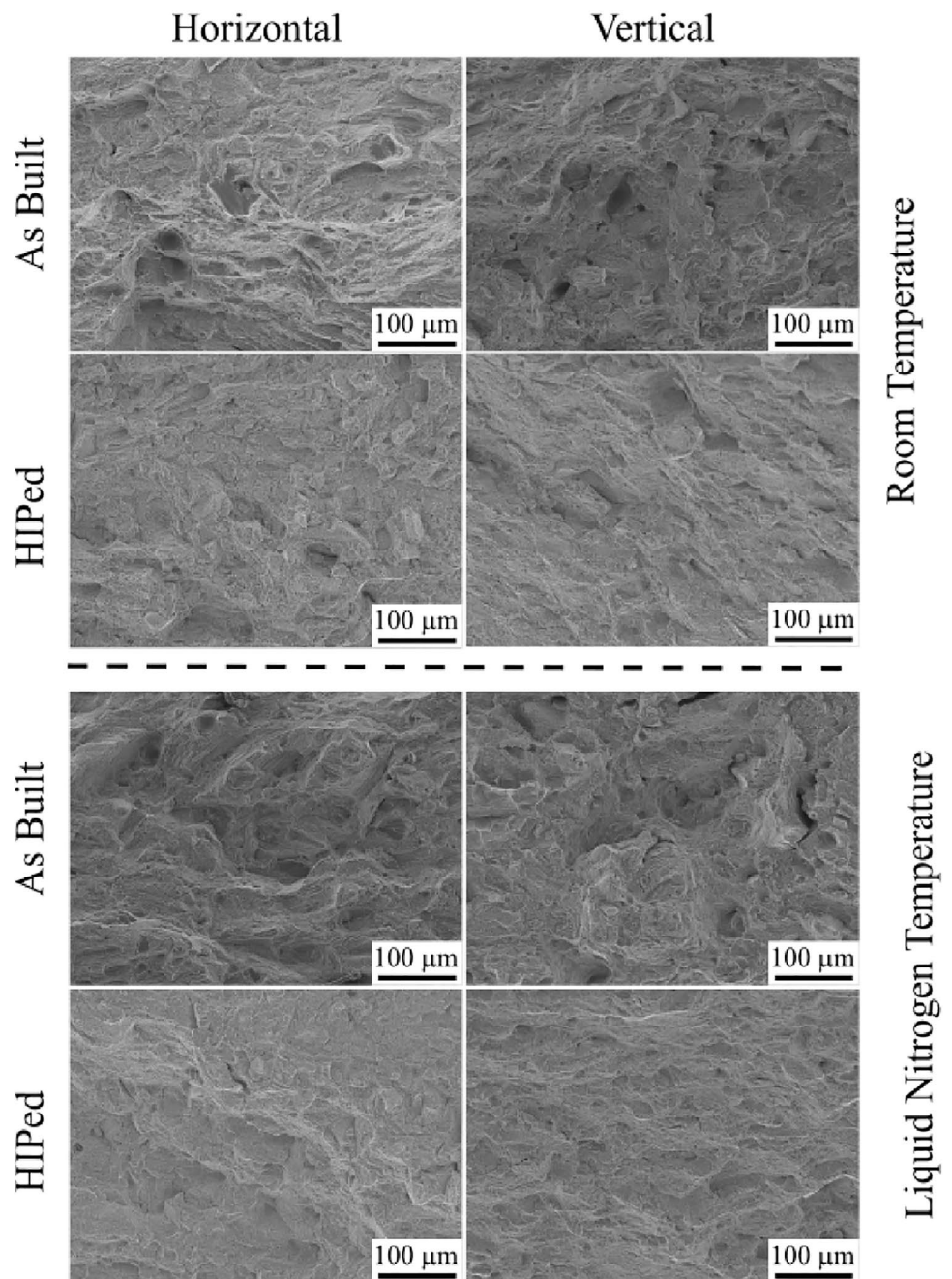
in chromium (Cr), there is no evidence of the formation of abrasion-resistant chromium carbide. As a result, the Cr-rich region wears out at the same rate as the rest of the matrix. Overall, both 316L SS and CoCrFeMnNi exhibit uniform wear, without any evidence of significant alloy segregation.

During abrasion, the first step is the indentation by the abrasive particle. The second step involves the sliding/rolling of the indented abrasive particles, leading to the removal of material from the surface, resulting in wear debris. The extent of material removal depends on the

involved wear mechanisms (e.g., scratching, ploughing, wedge formation, cutting, etc. [75]. With an increase in the penetration depth of the abrasive particle, the wear mechanism transitions from scratching/ploughing (mild) to wedge formation (moderate) and cutting (severe).

Physical properties (e.g., hardness, toughness, etc.) of materials play a crucial role in determining their wear performance. Generally, materials with higher hardness provide better wear performance. This is mainly because, for the same applied load, higher hardness results in a smaller

Table 7 The chemical composition and properties of the wrought 316L SS

Chemical composition (%)

C	Si	Mn	Mo	Cu	Cr	Ni	P	S	N	Fe
0.024	0.44	1.35	2.02	0.05	16.59	10.04	0.023	0.001	0.036	Balance

Mechanical properties

YS (MPa)	UTS (MPa)	EL (%)	Hardness (HRB)
297.6	659.5	57.8	82.9

penetration depth. As a result, materials undergo mild to moderate wear instead of severe wear. Rabinowicz [76–78] proposed a simplified wear model suggesting that the wear rate should vary inversely with the hardness of the material. While many pure metals behave in this way, engineering alloys, particularly those with multiple-phase microstructures and higher toughness, often exhibit more complex behavior.

As observed in this study, micro-ploughing and microcutting are the dominant wear modes for the evaluated materials. While pure micro-ploughing or micro-cutting may occur under certain conditions, for most engineering materials, the wear modes are often mixed micro-ploughing and micro-cutting. In this scenario, a portion of the material displaced from the wear groove is detached to form wear debris (micro-cutting), and the rest is plastically pushed to the sides of the wear groove (micro-ploughing). A schematic of the micro-ploughing and micro-cutting wear mechanisms is illustrated in Figs. 32a, b and 32c, d, respectively, modified from [79] as appropriate for the present study.

It is interesting to note that despite a 33% reduction in hardness after HIP, the HIPed CoCrFeMnNi exhibited comparable wear resistance to its harder counterpart, AB CoCrFeMnNi. This can be attributed to improved toughness and ductility after HIP. As a result, the materials undergo more plastic deformation and micro-ploughing without being completely removed from the surface. Moreover, higher toughness can facilitate the formation of a thin tribo-layer at the top surface, a key factor contributing to the observed improvement in wear performance.

Corrosion Behaviour

Figure 33a shows a representative potentiodynamic polarization curve for AB CoCrFeMnNi in a 3.5 wt% NaCl solution. Several important parameters such as corrosion potential (E_{corr}), corrosion current density (I_{corr}), passivation current density (I_{pass}), and pitting potential (E_{pit}) or breakdown potential (E_b) can be obtained from the polarization curve. Typically, Tafel extrapolation in the linear regime of potential versus current density is used to determine the corrosion potential (E_{corr}) and corrosion current density (I_{corr}).

During anodic polarization, the material's behavior varies based on environmental conditions and corrosion resistance. It may undergo active dissolution, where the material actively dissolves without passivation [80], or experience an active–passive transition. In the latter, the material dissolves actively at the OCP and can be passivated in the passive region [81]. Alternatively, the material may exhibit stable passive behavior or pseudo-passive behavior, allowing spontaneous passivation at the OCP [82, 83]. In cases of localized corrosion, this passive film is damaged at a potential known as the breakdown potential (E_b). In the presence of pitting corrosion, this potential is known as the pitting potential (E_{pit}), and in the presence of crevice corrosion, it becomes the crevice potential (E_{crev}) [84–90].

The anodic polarization of AB CoCrFeMnNi in a 3.5 wt% NaCl solution exhibits pseudo-passive behavior (Fig. 33a). The current density remains somewhat constant with increasing potential, indicating the passivation current density (I_{pass}). It is interesting to note that the occasional anodic current peaks in the polarization curve suggest the generation of metastable pitting, quickly covered by the newly formed passive film. With a further increase in potential, around 9.8 mV versus SCE, the pitting potential (E_{pit}) represents the formation of stable pits when the passive film has broken down, and the corrosive solution comes in direct contact with the material, as shown by the rapid increase in anodic current density (Transpassive region). In general, a higher pitting potential (E_{pit}) indicates the formation of a stable and compact passive film, which is more resistant to corrosive $Cl-$ anion attacks [83].

A representative polarization curve for AB CoCrFeMnNi in a 1 N H_2SO_4 solution is shown in Fig. 33b. The polarization curve in the acidic solution is slightly different from the one obtained in chloride solution. As observed in this figure, AB CoCrFeMnNi exhibits an active–passive transition during anodic polarization. In addition to typical corrosion parameters (e.g., I_{corr} and E_{corr}), we can also measure the critical current density of passivation (I_{cp}) and the corresponding primary passive (or passivation) potential (E_{pp}). This is where the passive film becomes stable, and the material transitions from the active to the passive state. We can also measure the passivation potential (E_p) and the
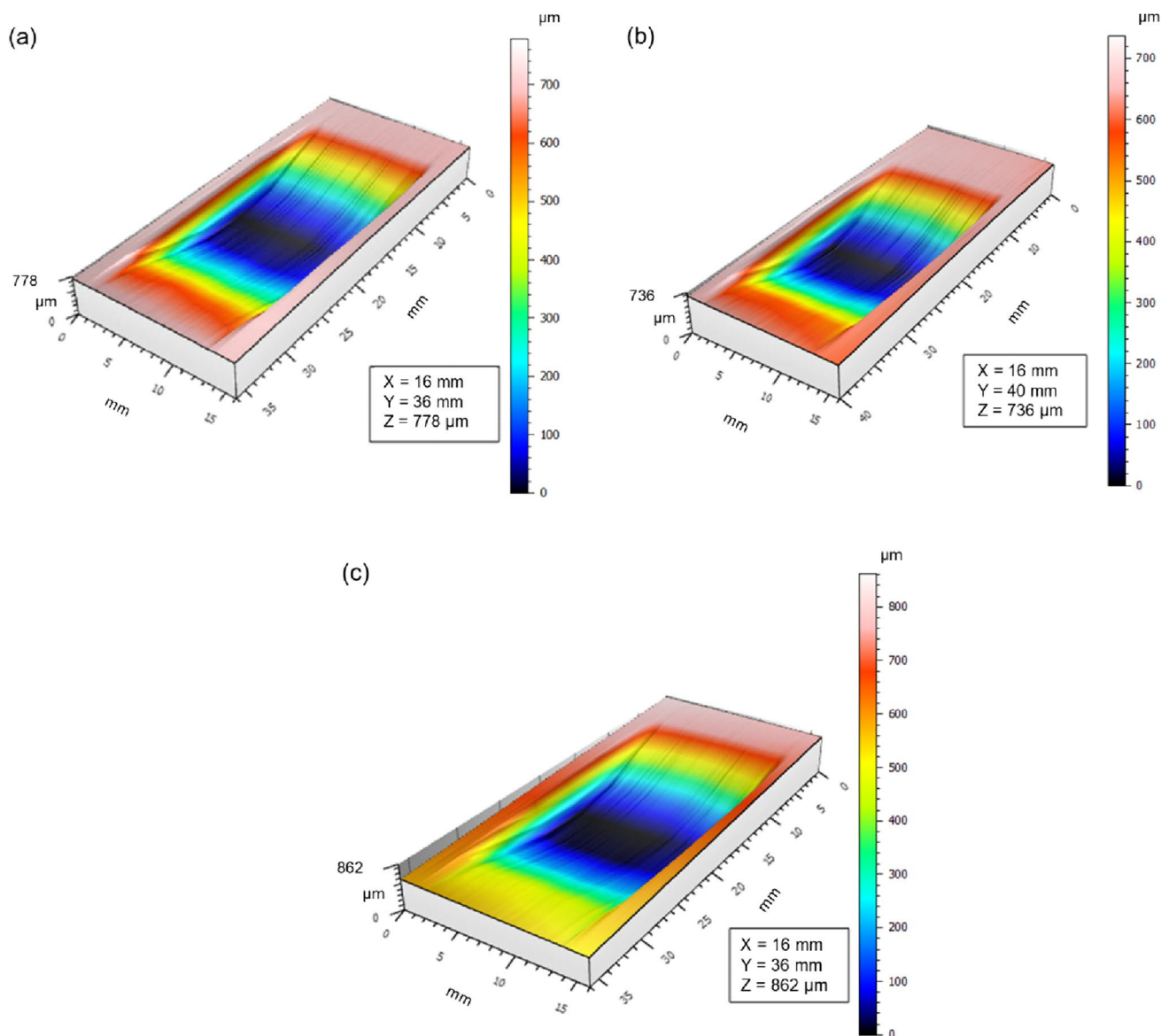
Fig. 26 Laser profilometry image of the wear scar **a** 316L SS-wrought, **b** AB CoCrFeMnNi, and **c** HIPed CoCrFeMnNi

passivation current (I_{pass}), where the anodic dissolution of the alloy undergoes a significant reduction from the critical current density of passivation (I_{cp}), bringing it to the condition of almost zero corrosion.

Figure 34a, b illustrates the potentiodynamic polarization curve for 430 SS, 316L SS, AB CoCrFeMnNi and HIPed CoCrFeMnNi in NaCl and H_2SO_4, respectively, as a representative example. Figure 34c–f shows the corrosion rate and the corrosion potential for the materials, obtained from Tafel extrapolation. In this study, three repeated tests were performed for data reproducibility, and the error bars in the graph represent the standard deviation from these three tests. It is also important to note that, for the electrochemical corrosion test, 430 SS (obtained from Metal Samples, 152 Metal Samples Rd., Mumford, AL, as recommended in ASTM G5) is also used as a reference material, in addition to 316L SS.

During anodic polarization, both 316L SS and AB CoCrFeMnNi exhibit similar pseudo-passive behavior in a chloride solution. We can observe the formation of a stable passive film, which is then damaged at the pitting potential (E_{pit}) with further increase in potential. HIPed CoCrFeMnNi, on the other hand, does not display as stable a passive film as AB CoCrFeMnNi and does not exhibit a sharp pitting potential. 430 SS displayed the smallest passive region compared to other materials. We can also see some evidence of metastable pitting before the transpassive region.

Fig. 27 Comparison of low-stress wear performance of CoCrFeMnNi HEA in the AB and HIPed conditions relative to reference 316L SS
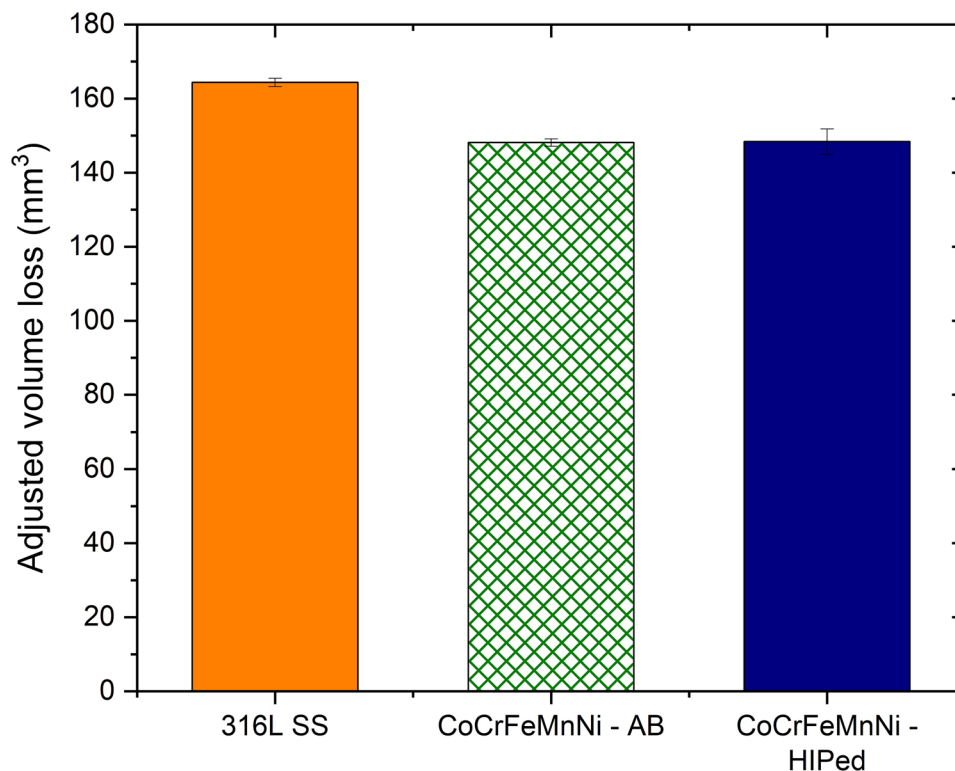
Both AB and HIPed CoCrFeMnNi display better corrosion resistance than the reference materials in the chloride-containing environment (Fig. 34c). AB CoCrFeMnNi exhibits around 2.2 times better corrosion performance than 316L SS. HIPed CoCrFeMnNi shows a similar behavior as AB CoCrFeMnNi with a slightly higher standard deviation. Figure 34e shows the corrosion potential of the evaluated materials. 316L SS exhibits the highest, while 430 SS displays the lowest corrosion potential in the chloride solution.

In the acid-containing environment, both AB CoCrFeMnNi and HIPed CoCrFeMnNi, along with 430 SS, exhibit an active–passive transition during anodic polarization, while 316L SS demonstrates the formation of a stable passive film (Fig. 34b). AB CoCrFeMnNi displays the lowest critical current density of passivation (I_{cp}) and the lowest passivation current density (I_{pass}) among the evaluated materials. In this study, 316L SS exhibited the best corrosion resistance in the acidic environment, as depicted in Fig. 34d. Specifically, 316L SS demonstrated approximately 15.5 times better corrosion resistance than the second-best-performing AB CoCrFeMnNi. This superior performance of 316L SS is attributed to the presence of Mo, in addition to Cr and Ni, which contributes to an extended passivation region and enhanced corrosion resistance in low to intermediate concentrations of sulfuric acid at ambient temperature [91–93].

Conversely, 430 SS exhibited the lowest corrosion resistance, mainly due to its lower Ni content (i.e., ∼ 0.50 wt%) and the absence of Mo. Based on the present findings, HIPed CoCrFeMnNi shows an inferior performance, approximately 6.6 times lower than that of AB CoCrFeMnNi in the acidic solution. The corrosion potential (E_{corr}) versus SCE is illustrated in Fig. 34f. As evident from this figure, an interesting correlation emerges between the corrosion rate and corrosion potential, signifying that the corrosion resistance of the evaluated materials increases with an elevation in corrosion potential (E_{corr}).

The corrosion potential (E_{corr}), corrosion current (I_{corr}) and the corrosion rate for the evaluated materials are tabulated in Table 8. The corrosion parameters from the previous study are also included for comparison. Figure 35a and b illustrate the relationship between corrosion rate (CR) and corrosion potential (E_{corr}) in chloride and acid-containing environments, respectively. As seen in Fig. 35b, a good correlation exists between corrosion rate and corrosion potential in an acid-containing environment. As observed in this figure, CoCrFeMnNi HEA with higher corrosion potential typically displays greater corrosion resistance in the acid-containing environment. However, although some CoCrFeMnNi HEA with low corrosion potential exhibit lower corrosion resistance, there is no significant correlation between the corrosion rate and corrosion potential in the chloride-containing environment (Fig. 35a).

The corrosion rate for AB and HIPed CoCrFeMnNi from this study is represented by red data points. As illustrated
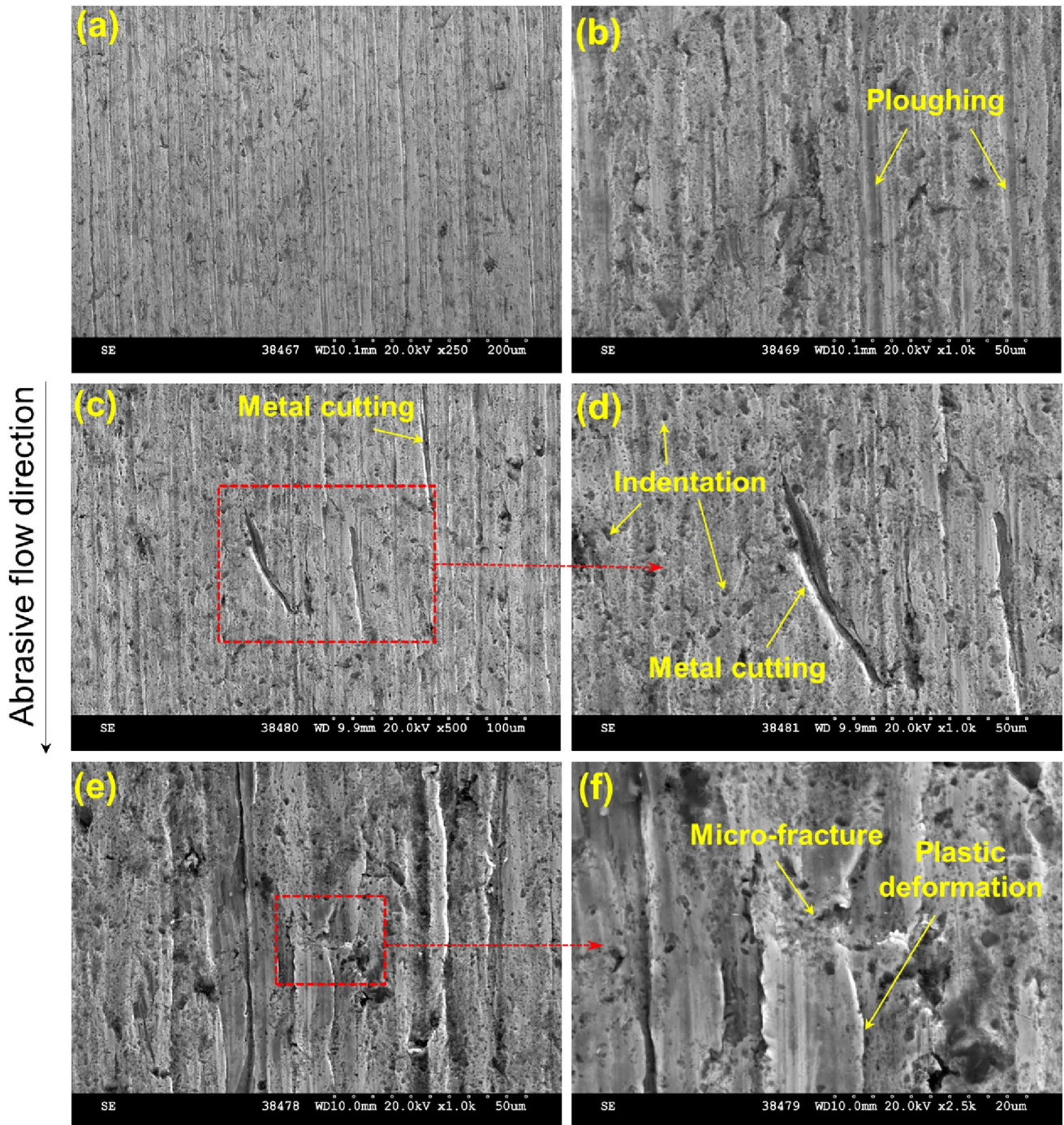
Fig. 28 Wear scar of SS-316L after low-stress abrasion

in Fig. 35a, both AB and HIPed CoCrFeMnNi display the best corrosion resistance compared to other representative CoCrFeMnNi HEAs from previous studies. AB CoCrFeMnNi exhibits 2, 6, and 35 times better corrosion resistance than CoCrFeMnNi HEAs produced by laser surface alloying, selective laser melting (SLM), and casting, respectively. In an acid-containing environment (Fig. 35b), the HIPed CoCrFeMnNi performs similarly to cast & rolled HEAs. However, AB CoCrFeMnNi produced in the resent study still remains one of the best-performing HEAs compared to others.
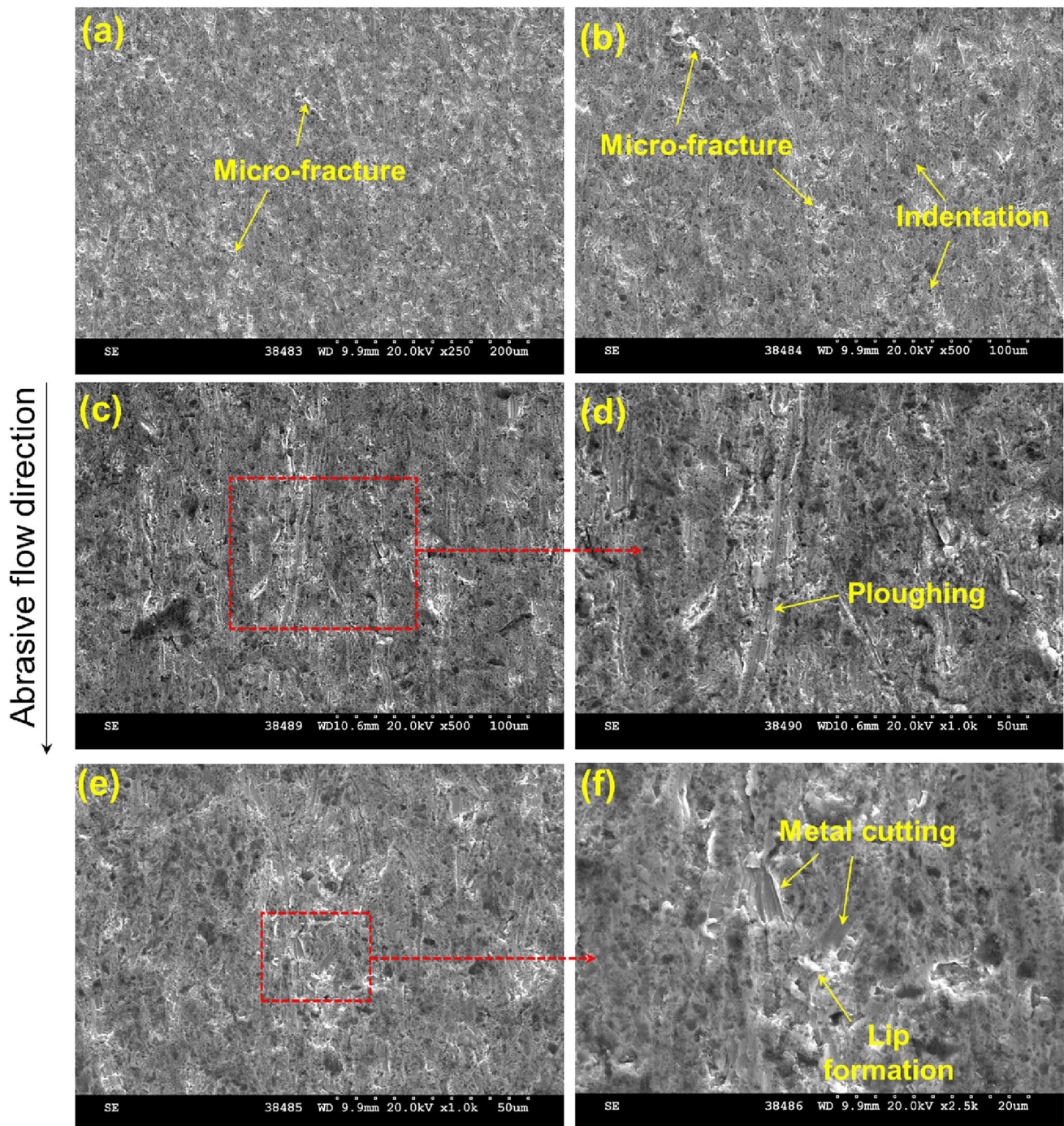
Fig. 29 Wear scar of CoCrFeMnNi—as-built after low-stress abrasion

Hydrogen Permeation

In Fig. 36a the current–density profiles for 316L SS, AB CoCrFeMnNi, and HIPed CoCrFeMnNi are presented as a function of the permeation test duration. All specimens achieved the steady-state, and their permeation curves exhibited a sigmoidal shape, which is in accordance with Fick's law [102, 103]. It is evident from this figure that 316L SS demonstrates a higher steady-state current density compared to AB and HIPed CoCrFeMnNi. The extended time required by 316L SS to reach the steady-state, in contrast to the CoCrFeMnNi HEA, is attributed primarily to its higher steady-state current and lower diffusion rate. Consequently, 316L SS exhibits a higher
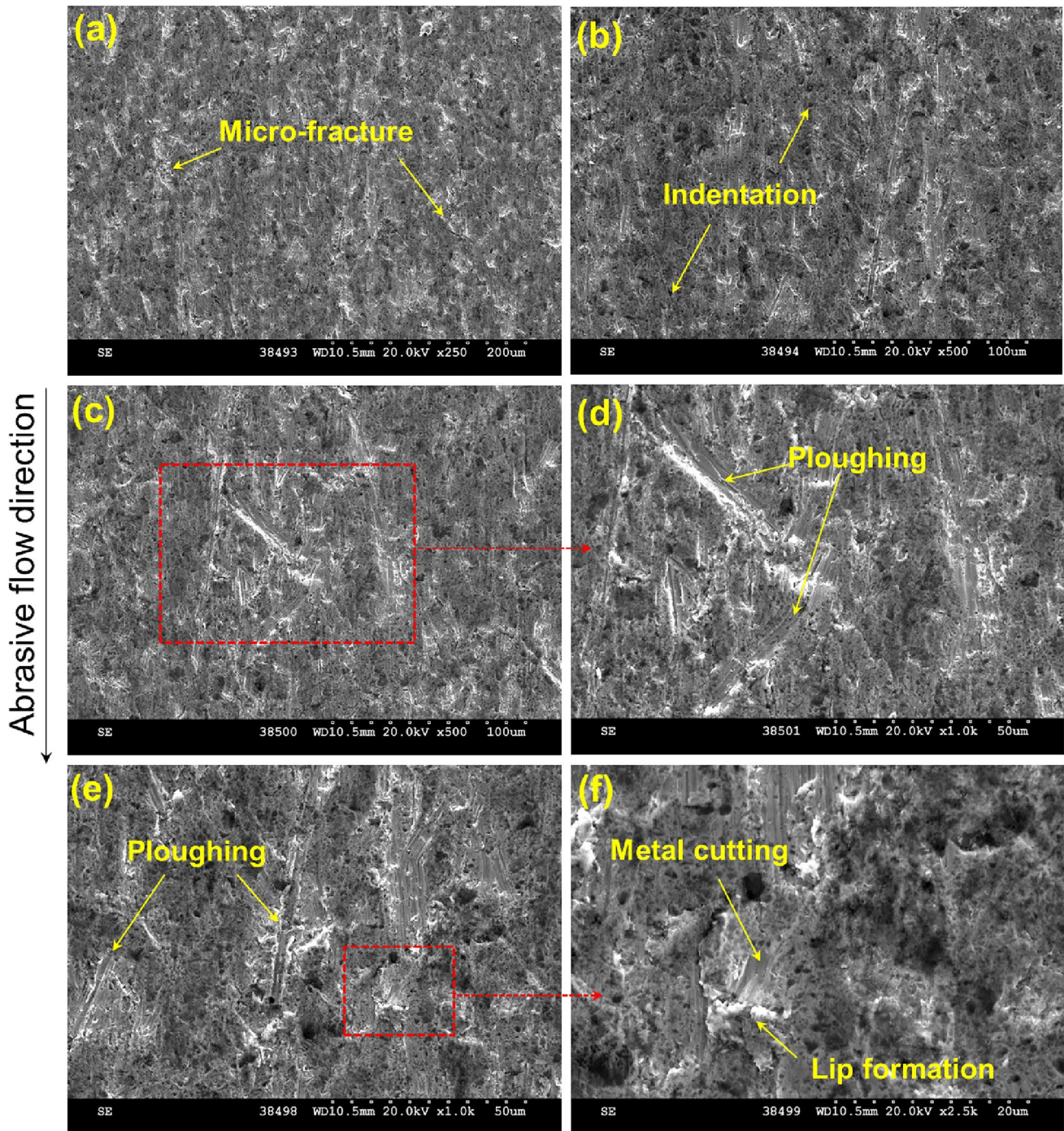
Fig. 30 Wear scar of CoCrFeMnNi—HIPed after low-stress abrasion

breakthrough time than CoCrFeMnNi in both the AB and HIPed conditions. Figure 36b illustrates the steady-state current density/permeation flux for the materials. The steady-state permeation flux for 316L SS is approximately 4.8 and 2.1 times higher than that for the AB and HIPed CoCrFeMnNi, respectively. This implies that, for identical material thickness and operating conditions, the quantity

of hydrogen atoms permeating through 316L SS will be 4.8 times greater than that through AB CoCrFeMnNi.

In contrast, Lee et al. [104] studied the hydrogen-diffusion behavior of cold rolled and recrystallized-heat-treated CoCrFeMnNi using electrochemical-hydrogen permeation testing. They compared its performance with cold rolled, solution-heat-treated 304 SS and 316L SS. It was found
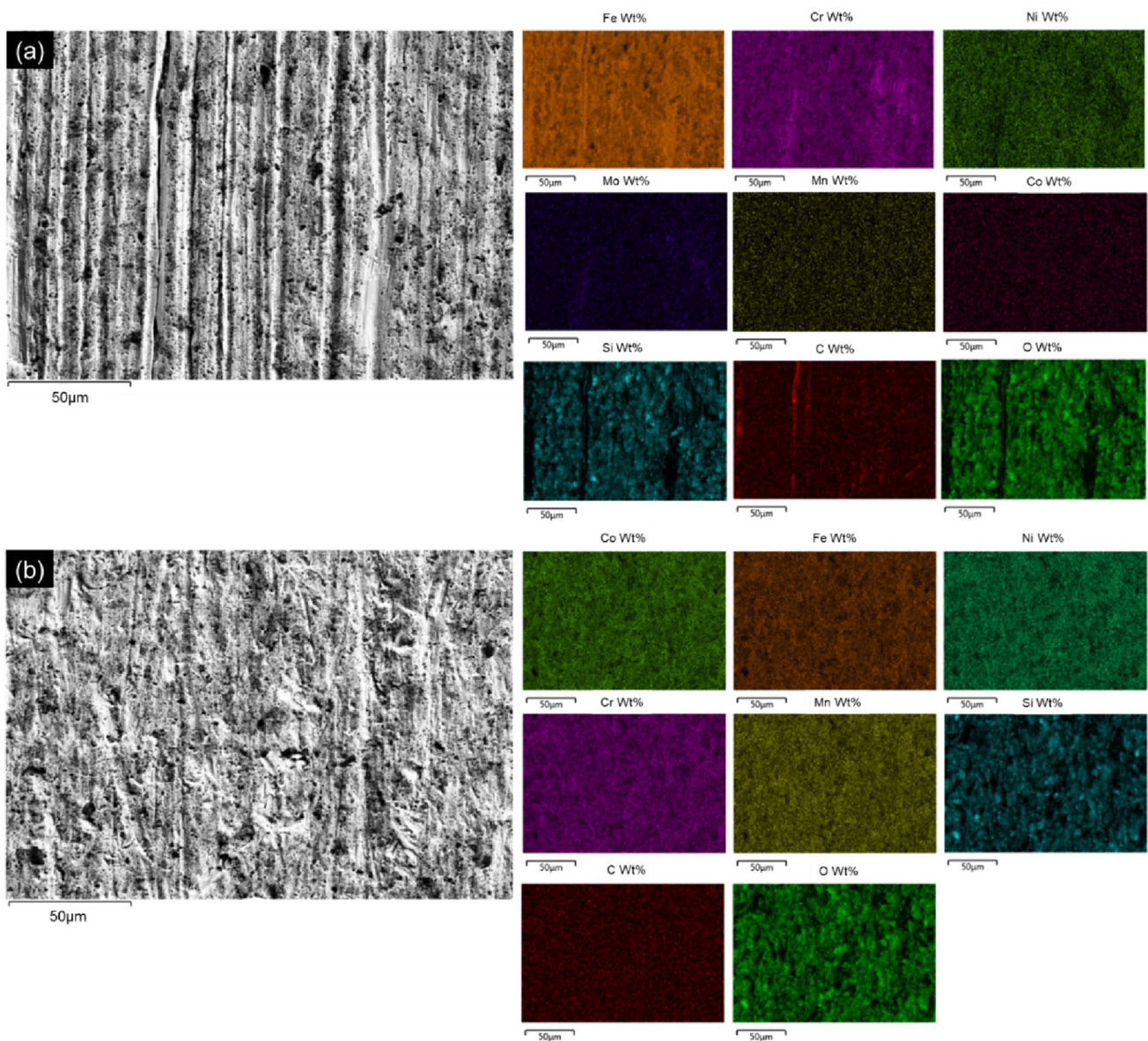
Fig. 31 EDS mapping of the wear scar **a** 316L SS and **b** AB CoCrFeMnNi

that the steady-state permeation flux for CoCrFeMnNi is approximately 1.2 and 1.6 times higher than 304 SS and 316L SS, respectively. This suggests that the hydrogen permeation behavior of materials depends on various factors, including the manufacturing process that influences the microstructure of the material, such as the dislocation densities, grain boundaries, micro-porosity, number of trap sites, activation energy barrier, and so on.

The effective hydrogen diffusion coefficient (D_{eff}) was determined using Eqs. (4) and (5) and the results are presented in Fig. 36c. The diffusion coefficient (D_{eff}) of 316L SS, AB CoCrFeMnNi and HIPed CoCrFeMnNi are 1.19×10^{-12}, 3.17×10^{-12} and 8.79×10^{-12} m^2/s, respectively. Previous investigations on CoCrNi medium entropy alloy, cold rolled Fe$_{20}$Mn$_{20}$Ni$_{20}$Co$_{20}$Cr$_{20}$ and arc melted Fe$_{20}$Mn$_{20}$Ni$_{20}$Co$_{20}$Cr$_{20}$ HEA exhibited diffusion coefficients of 2.03×10^{-16}, 1.81×10^{-11} and 3.7×10^{-16} m^2/s, respectively [102, 104, 105]. Conversely, depending on processing parameters and heat treatment, the diffusion coefficient of 316L SS varies from 1.31×10^{-11} to 4.3×10^{-16} m^2/s [104, 106, 107]. As observed in the Fig. 36c, the hydrogen diffusion coefficients of AB and HIPed CoCrFeMnNi are 2.7 and 7.4 times higher, respectively, than that of 316L SS. A previous study demonstrated that the CoCrFeMnNi HEA in colled rolled and recrystallized-heat-treated condition also exhibits a diffusion coefficient 1.4 times higher than that of 316L SS [104].
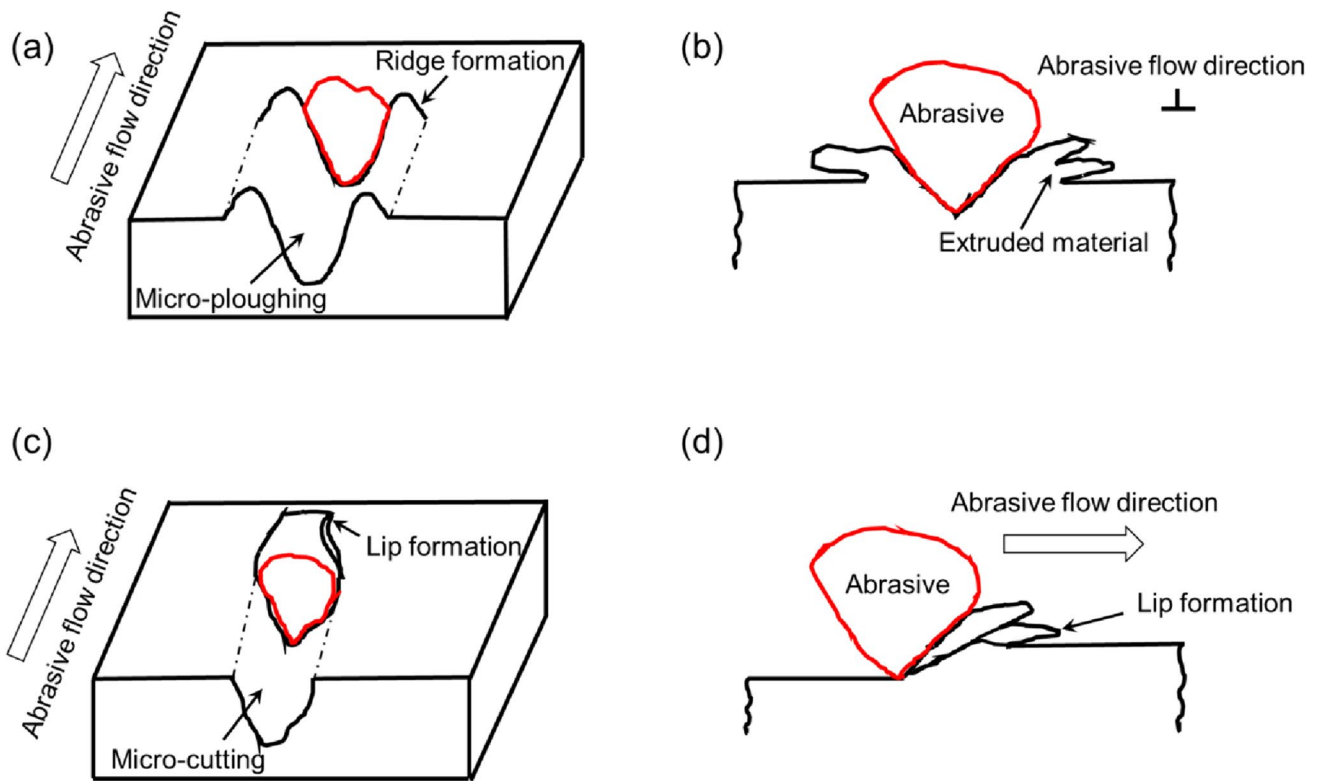
Fig. 32 Schematic of the dominant wear mechanisms, **a**, **b** micro-ploughing and **c**, **d** micro-cutting [79]
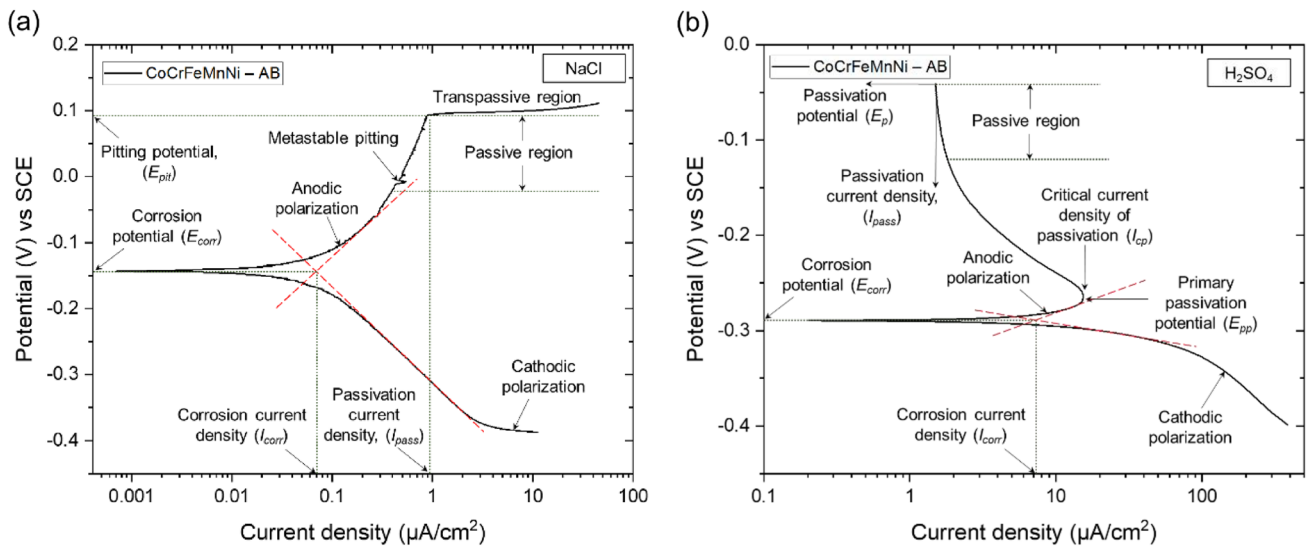

Fig. 33 Representative polarization curves for AB CoCrFeMnNi in **a** 3.5 wt% NaCl and **b** 1 N H_2SO_4

The sub-surface concentration of atomic hydrogen at the charging side of the specimen was calculated using Eq. 6, where L is the specimen thickness and J_{ss} is the atomic hydrogen permeation flux at steady-state [57]:

$$C_{0R} = \frac{J_{ss} \times L}{D_{eff}} \tag{6}$$

Figure 36d illustrates the sub-surface concentration of atomic hydrogen for the evaluated materials. The sub-surface of 316L SS contains approximately 32 and 26 times
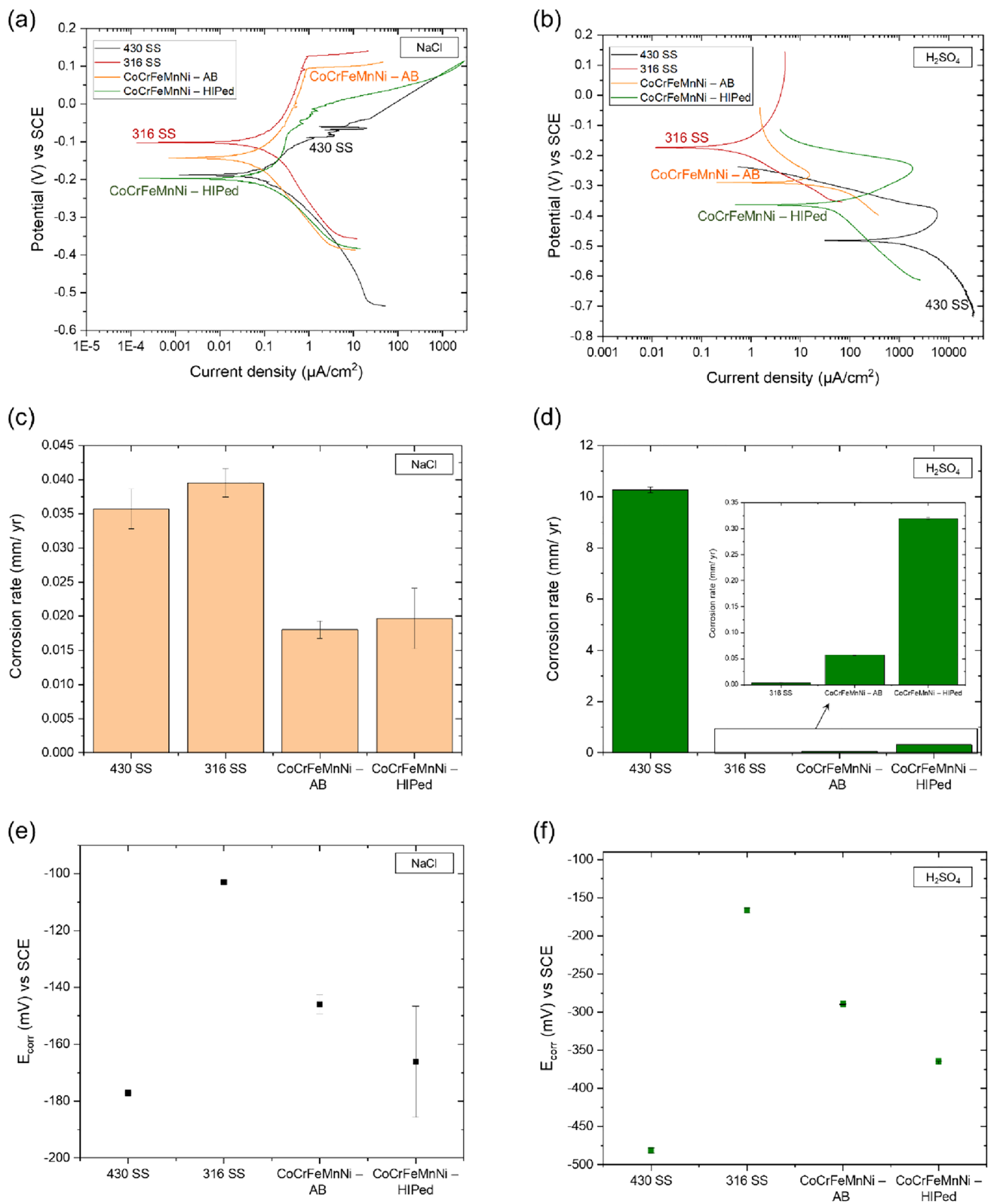
Fig. 34 Corrosion behaviour of 430SS, 316L SS, AB CoCrFeMnNi and HIPed CoCrFeMnNi, **a** - **b** potentiodynamic polarization curve, **c**, **d** CR and **e**, **f** E$_{corr}$ in NaCl and H$_2$SO$_4$, respectively

Table 8 Corrosion potential, corrosion current and corrosion rate for the evaluated materials in 3.5 wt% NaCl and 1.0 N H_2SO_4 electrolytes

Tested materials	E_{corr} (mV) versus SCE	I_{corr} ($\mu A/cm^2$)	Corrosion rate (mm/yr)	Corrosion rate (mpy)	Reference
3.5 wt% NaCl					
430 SS	−177	8.90×10^{-2}	9.06×10^{-4}	3.57×10^{-2}	This study
316L SS	−103	10.3×10^{-2}	10.02×10^{-4}	3.95×10^{-2}	This study
AB CoCrFeMnNi	−146	5.10×10^{-2}	4.58×10^{-4}	1.80×10^{-2}	This study
HIPed CoCrFeMnNi	−166	5.55×10^{-2}	5.00×10^{-4}	1.97×10^{-2}	This study
CoCrFeMnNi—As cast	−457	112.3×10^{-2}	1.01×10^{-2}	39.70×10^{-2}	[94]*
CoCrFeMnNi—SLMed	−265	47.4×10^{-2}	0.42×10^{-2}	16.8×10^{-2}	[94]*
CoCrFeMnNi—Cast	−483	554.7×10^{-2}	4.98×10^{-2}	196.0×10^{-2}	[95]*
CoCrFeMnNi—As cast	−275	38.3×10^{-2}	0.34×10^{-2}	13.5×10^{-2}	[96]*
$Co_{0.4}Cr_{0.8}Fe_{0.2}Mn_{1.0}Ni_{0.6}$—As cast	−300	47.6×10^{-2}	0.42×10^{-2}	16.8×10^{-2}	[97]*
CoCrFeMnNi—Cast	−268	6.5×10^{-2}	5.78×10^{-4}	2.28×10^{-2}	[98]*
CoCrFeMnNi—SLMed	−263	11.9×10^{-2}	10.70×10^{-4}	4.24×10^{-2}	[99]*
CoCrFeMnNi—Laser surface alloying	−218	10.5×10^{-2}	9.42×10^{-4}	3.71×10^{-2}	[100]*
1.0 N H_2SO_4					
430 SS	−481	1.01×10^{3}	1.03×10^{1}	4.04×10^{2}	This study
316L SS	−167	3.79×10^{-1}	3.68×10^{-3}	1.45×10^{-1}	This study
AB CoCrFeMnNi	−290	63.63×10^{-1}	5.71×10^{-2}	0.22×10^{1}	This study
HIPed CoCrFeMnNi	−365	3.54×10^{1}	3.19×10^{-1}	1.26×10^{1}	This study
CoCrFeMnNi—Cast & rolled	−366	5.79×10^{1}	5.19×10^{-1}	2.05×10^{1}	[101]*
CoCrFeMnNi—Cast & rolled (fine grain)	−353	4.64×10^{1}	4.16×10^{-1}	1.64×10^{1}	[101]*
CoCrFeMnNi—Cast & rolled (medium grain)	−291	0.56×10^{1}	5.05×10^{-2}	0.19×10^{1}	[101]*
CoCrFeMnNi—Cast & rolled (coarse grain)	−336	0.91×10^{1}	8.19×10^{-2}	0.32×10^{1}	[101]*
CoCrFeMnNi—Laser surface alloying	−127	0.89×10^{1}	8.04×10^{-2}	0.31×10^{1}	[100]*

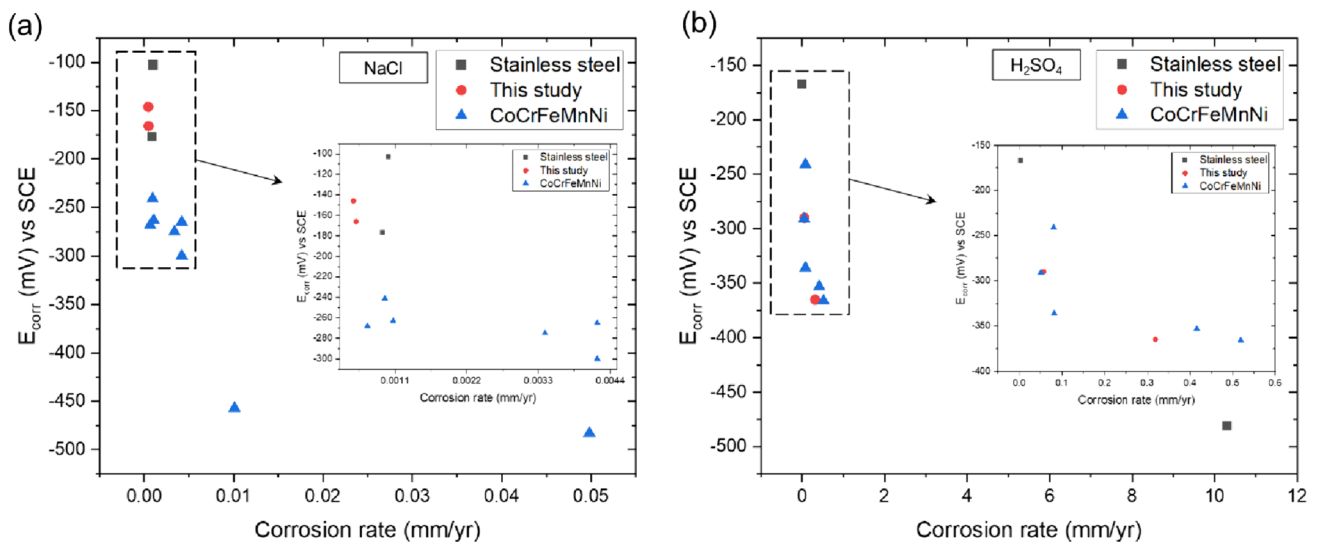*Corrosion rate was calculated from I_{corr}

Fig. 35 Relationship between corrosion rate (CR) and corrosion potential (E_{corr}) in a **a** 3.5 wt% NaCl and **b** 1 N H_2SO_4

more atomic hydrogen concentration compared to AB amd HIPed CoCrFeMnNi, respectively. A previous study indicated that 316L SS, with a FCC austenite structure, has higher hydrogen solubility compared to materials with a BCC structure, such as martensitic and ferrite [108–111]. In the case of iron-based alloys, materials with a higher
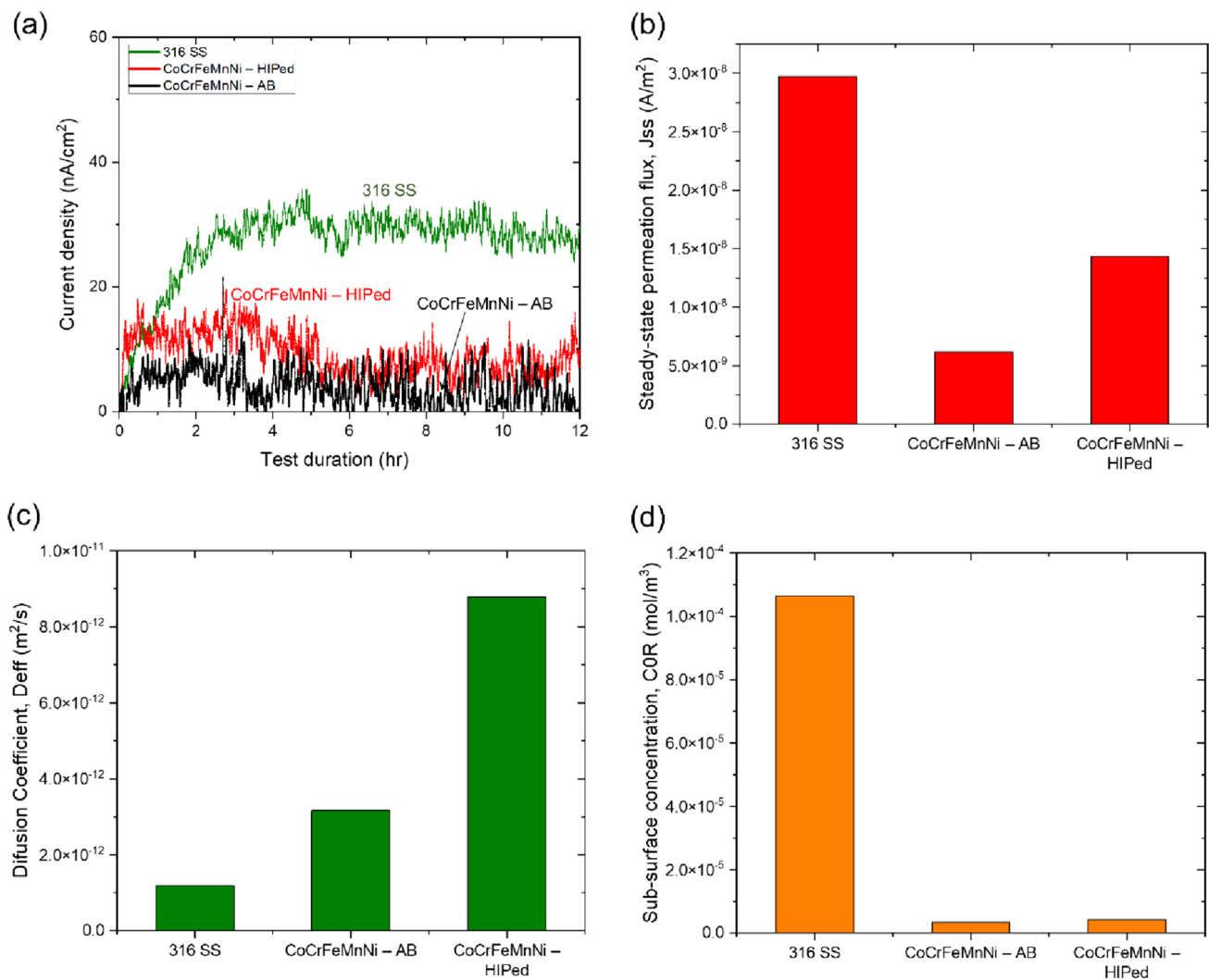
Fig. 36 Electrochemical permeation test results for 316L SS, AB CoCrFeMnNi, and HIPed CoCrFeMnNi; **a** permeation current density vs. test duration, **b** steady-state current, **c** diffusion coefficient, and **d** sub-surface hydrogen concentration

content of austenite (i.e., FCC crystal structure) typically exhibit better embrittlement resistance than ferritic ones (i.e., BCC). For HEAs, correlating the sub-surface concentration of atomic hydrogen with embrittlement resistance is crucial and requires a fundamental understanding of the degradation mechanisms.

Pu et al. [112] investigated the hydrogen embrittlement resistance of the CrMnFeCoNi HEA at both room and cryogenic temperatures through tensile experiments. Test specimens were charged via cathodic electrochemical charging. Two representative steels, namely 316L SS and X80 pipeline steel, were used for comparison. Their findings revealed that at room temperature, the embrittlement susceptibility of CrMnFeCoNi, 316L SS, and X80 PS are 13%, 25%, and 53%, respectively, suggesting that the CrMnFeCoNi HEA exhibits the highest embrittlement resistance [112]. At cryogenic temperature (i.e., 77 K), the tensile ductility

of CrMnFeCoNi HEA and 316L SS remained almost unaffected by hydrogen due to lower diffusivity at that temperature, while the ductility of pre-charged X80 pipeline steel was still reduced by 27%.

Zhu et al. [113] investigated the impact of hydrogen on the tensile properties of equiatomic FeCrNiMnCo fabricated by vacuum induction melting and compared its performance with deformed 316NG nitrogen-containing SS. They concluded that their FeCrNiMnCo HEA not only exhibits resistance to hydrogen embrittlement but also functions as an alloying element, enhancing both strength and ductility. The strength of 316NG SS experienced a slight decrease, and a significant reduction in ductility (from 32 to 16%) after hydrogen charging. In contrast, both the strength and ductility of the FeCrNiMnCo increased after hydrogen charging. The study revealed that hydrogen at the interfaces, including grain boundaries and twin boundaries, is the primary factor

influencing the mechanical properties of the materials. This phenomenon occurs because hydrogen at the interface, during deformation, promotes the formation of stacking faults/nanotwins, which, in turn, inhibits the diffusion of hydrogen. The diffusion barrier and diffusion coefficient of hydrogen in FeCrNiMnCo HEA and 316NG SS were very close at different temperatures, indicating that hydrogen diffusion is not the primary cause of the observed differences in fracture behavior.

The diffusion coefficients and sub-surface concentrations of hydrogen for the materials evaluated in present study are tabulated in Table 9. Additionally, diffusion coefficients of previously studied 316L SS samples and the $Fe_{20}Mn_{20}Ni_{20}Co_{20}Cr_{20}$ HEA in different conditions are included for reference. Disparities in the permeation behavior among different materials can be attributed to distinct crystal structures, available trap sites, activation energy, alloying elements, dislocation densities, grain boundaries, micro-porosities, and other factors [105]. It is important to note that, even for the same materials, crystalline defects (such as dislocations and grain boundaries) are not uniformly distributed throughout the material. As a result, the hydrogen diffusion behavior may exhibit variations across different localized regions, leading to deviations in the effective diffusion coefficient (D_{eff}) values.

Both the AB and HIPed CoCrFeMnNi fabricated in this study exhibit lower diffusion coefficients and sub-surface hydrogen concentrations compared to other HEAs in the literature. Additionally, the steady-state current permeating through CoCrFeMnNi is lower than that through 316L SS (reference material). This suggests that under the same material thickness and operating conditions, CoCrFeMnNi will show higher hydrogen permeation resistance than 316L SS. It's important to note that this study doesn't specifically address the hydrogen embrittlement resistance of the HEAs. Correlating sub-surface atomic hydrogen concentration with embrittlement resistance is crucial for a fundamental understanding of degradation mechanisms. To date, only limited studies have evaluated the hydrogen permeation behavior of CoCrFeMnNi alloy [102, 104, 115]. Further investigations are necessary to explore this relationship, not only for the CoCrFeMnNi alloy but also for other HEA compositions, especially in the context of enabling a green hydrogen economy to aid global decarbonization.

Conclusions

This research study involved laser powder bed fusion (LPBF) processing of the CoCrFeMnNi alloy to develop the material-process-structure–property relationships that are key to maturing digital manufacturing of a promising high entropy alloy (HEA) candidate for defence. The following conclusions can be drawn from the current study:

The commercially available argon gas-atomized CoCrFeMnNi powder consisted of spherically shaped particles with a few irregularities and fine satellites attached to their surfaces. The particle size distribution, apparent density, static flowability and dynamic flowability characteristics of the powder were suitable for LPBF processing.

The CoCrFeMnNi powder particles exhibited a dendritic structure with some entrapped gas porosity and elemental segregation, most particularly Mn and to much lesser extent Ni, within the interdendritic regions. X-ray diffraction (XRD) indicated that the powder was predominately single-phase with a face-centered cubic (FCC) structure.

The CoCrFeMnNi alloy showed high sensitivity to LPBF process conditions and considerable effort was needed to optimize the process parameters to achieve highly dense crack-free parts. Although, there was no visible relationship between the volumetric energy density (VED) and the

Table 9 Diffusion coefficient and sub-surface concentration of hydrogen

Tested materials	Diffusion coefficient, D_{eff} (m²/s)	Sub-surface concentration, C_{0R} (mol/m³)	References
316L SS	1.19×10^{-12}	1.06×10^{-4}	This work
316L SS (cold rolled, solution treated)	13.10×10^{-12}	4.80×10^{-2}	[104]
316L SS (cold rolled)	0.41×10^{-12}	–	[107]
316L SS	2.70×10^{-16}	–	[114]
CoCrFeMnNi—AB	3.17×10^{-12}	3.37×10^{-6}	This work
CoCrFeMnNi—HIPed	8.79×10^{-12}	4.10×10^{-6}	This work
CoCrFeMnNi	18.10×10^{-12}	4.30×10^{-2}	[104]
$Fe_{20}Mn_{20}Ni_{20}Co_{20}Cr_{20}$	3.0×10^{-16}	–	[102]
$Fe_{20}Mn_{20}Ni_{20}Co_{20}Cr_{20}$ (cold rolled 70%)	9.0×10^{-12}	–	[115]
$Fe_{20}Mn_{20}Ni_{20}Co_{20}Cr_{20}$ (annealed)	15.0×10^{-12}	–	[115]
$Fe_{20}Mn_{20}Ni_{20}Co_{20}Cr_{20}$ (high-pressure torsion)	30.0×10^{-12}	–	[115]
$Fe_{22}Mn_{40}Ni_{30}Co_6Cr_2$ (annealed)	55.0×10^{-12}	–	[115]

density of the specimens after LPBF processing, all the specimens having a VED lower than 60 J/mm^3, showed lack of fusion defects, while all the specimens having a VED higher than 110 J/mm^3 had a high number of large cracks. Therefore, the optimal LPBF processing window for this alloy is between 60 and 110 J/mm^3 VED.

Increasing the VED within the range of 80 to 100 J/mm^3 improved the surface features, especially for the top surface, which was more sensitive to the printing parameters compared to the side walls. Overall, for the top surface, the linear roughness parameters Ra and Rz ranged between 3–10 and 18–70 μm, respectively.

Specimen size was also an important factor and the optimal VED value for 5×5×5 mm^3 specimens was 73 J/mm^3, while 10×10×10 mm^3 specimens needed 104 J/mm^3 for a crack-free and highly dense (>99.5%) structure.

With optimal LPBF processing parameters, the as-built (AB) 5×5×5 mm^3 specimens fabricated with a VED of 73 J/mm^3 had a microstructure with a mixture of equiaxed and columnar grain structures mainly along the <110> direction without having a strong texture—as the multiple of uniform density (MUD) value was 3.02. By contrast, for the AB 10×10×10 mm^3 specimens fabricated with a VED of 104 J/mm^3, the solidification structure was columnar with the longitudinal axis oriented along the <100> direction— the preferential growth direction in FCC crystals. Within the equiaxed and columnar grains, cellular sub-grain structures were apparent. After hot isostatic pressing (HIP), the AB microstructure recrystallized and equiaxed grains with annealing twins were observed. HIP also led to the dissolution of the cellular sub-grain structure.

Both AB and HIPed specimens had higher strength, fracture strain (global and local) and modulus of toughness in the horizontally built specimens, which may be associated with crystallographic texture, grain morphology and/ or smaller size of the remnant gas pores.

After HIP, the anisotropy in the tensile mechanical properties was reduced in both the horizontally and vertically built specimens; this led to similar strain localization behavior and material toughness, as well as similar tensile strengths with elongation values that increased by ~50% due to the closure of the micro-pores. However, the yield strength of both the vertical and horizontal specimens decreased by 41% and 50% after HIP, corroborating with the observed reduction in hardness.

After HIP, the Charpy impact toughness of both horizontally and vertically built specimens increased by 21% and 41%, respectively, due to closure of the defects. The highest impact toughness was measured for the vertically built specimens in the HIPed condition. Cryogenic liquid nitrogen testing at 77 K led to a reduction in the Charpy impact toughness by 20–27% for all the specimen conditions.

The tensile fracture surfaces showed cup and cone type features for all the specimen conditions indicating that the fracture was ductile in nature. The fracture surfaces of the AB specimens had larger pores in the vertically built specimens, which correlated with the lower global and local fracture strain values. The majority of the porosity observed in the AB condition was eliminated after HIP. The fracture surfaces of the HIPed specimens consisted of fine dimples distributed throughout the fracture cross-section and similar features in both the vertical and horizontal specimens.

AB and HIPed CoCrFeMnNi exhibited better low-stress abrasion resistance than 316L SS. SEM observations revealed that scratching and ploughing parallel to the abrasive flow direction are the dominant wear mechanisms for 316L SS, while micro-fracture is the dominant mechanism for the HEAs.

In a chloride-containing environment, AB CoCrFeMnNi exhibits about 2.2 times better corrosion performance than 316L SS. HIPed CoCrFeMnNi also demonstrates similar corrosion behavior to AB CoCrFeMnNi. However, in an acid-containing environment, 316L SS shows approximately 15.5 times better corrosion resistance than AB CoCrFeMnNi. The superior corrosion performance of 316L SS is attributed to the presence of molybdenum, in addition to chromium and nickel, which extends the passivation region and enhances corrosion resistance.

316L SS demonstrates superior hydrogen permeability and a lower diffusion coefficient compared to AB and HIPed CoCrFeMnNi. This indicates that, for identical material thickness and operating conditions, the volume of hydrogen atoms permeating through 316L SS will be 4.8 times greater than through AB CoCrFeMnNi, despite having a 2.7 times lower diffusion coefficient.

After the electrochemical permeation test, 316L SS contains approximately 32 and 26 times more atomic hydrogen concentration in the sub-surface compared to AB and HIPed CoCrFeMnNi, respectively. Correlating the sub-surface concentration of atomic hydrogen with embrittlement resistance is crucial for the fundamental understanding of degradation mechanisms. Additional investigations are required to further explore this relationship.

Declarations

Conflict of interest On behalf of all authors, the corresponding author states that there is no conflict of interest.

Informed Consent Not applicable.

References

1. J.W. Yeh et al., Nanostructured high-entropy alloys with multiple principal elements: novel alloy design concepts and outcomes. Adv. Eng. Mater. **6**(5), 299–303 (2004)
2. B. Cantor et al., Microstructural development in equiatomic multicomponent alloys. Mater. Sci. Eng. A **375**, 213–218 (2004)
3. D.B. Miracle, O.N. Senkov, A critical review of high entropy alloys and related concepts. Acta Mater. **122**, 448–511 (2017)
4. R. Kozak, A. Sologubenko, W. Steurer, Single-phase high-entropy alloys–an overview. Z. Kristallogr. **230**(1), 55–68 (2015)
5. E. Pickering, N. Jones, High-entropy alloys: a critical assessment of their founding principles and future prospects. Int. Mater. Rev. **61**(3), 183–202 (2016)
6. F. Otto et al., Decomposition of the single-phase high-entropy alloy CrMnFeCoNi after prolonged anneals at intermediate temperatures. Acta Mater. **112**, 40–52 (2016)
7. G. Bracq et al., The fcc solid solution stability in the Co-Cr-Fe-Mn-Ni multi-component system. Acta Mater. **128**, 327–336 (2017)
8. F. Otto et al., The influences of temperature and microstructure on the tensile properties of a CoCrFeMnNi high-entropy alloy. Acta Mater. **61**(15), 5743–5755 (2013)
9. P.D. Jablonski et al., Manufacturing of high entropy alloys. Jom **67**, 2278–2287 (2015)
10. P. Wang et al., Additively manufactured CoCrFeNiMn high-entropy alloy via pre-alloyed powder. Mater. Des. **168**, 107576 (2019)
11. B. Dovgyy et al., Comprehensive assessment of the printability of CoNiCrFeMn in laser powder bed fusion. Mater. Des. **194**, 108845 (2020)
12. A. Piglione et al., Printability and microstructure of the CoCrFeMnNi high-entropy alloy fabricated by laser powder bed fusion. Mater. Lett. **224**, 22–25 (2018)
13. E.G. Campari, A. Casagrande, Microstructural study of CrNiCoFeMn high entropy alloy obtained by selective laser melting. Materials **15**(16), 5544 (2022)
14. P. Chen et al., Fabricating CoCrFeMnNi high entropy alloy via selective laser melting in-situ alloying. J. Mater. Sci. Technol. **43**, 40–43 (2020)
15. Y. Zhou et al., Selective laser melting of typical metallic materials: an effective process prediction model developed by energy absorption and consumption analysis. Addit. Manuf. **25**, 204–217 (2019)
16. Z. Zhu et al., Hierarchical microstructure and strengthening mechanisms of a CoCrFeNiMn high entropy alloy additively manufactured by selective laser melting. Scripta Mater. **154**, 20–24 (2018)
17. J. Guo et al., On the machining of selective laser melting CoCrFeMnNi high-entropy alloy. Mater. Des. **153**, 211–220 (2018)
18. R. Li et al., Selective laser melting of an equiatomic CoCrFeMnNi high-entropy alloy: processability, non-equilibrium microstructure and mechanical property. J. Alloys Compd. **746**, 125–134 (2018)
19. D. Zhao et al., Ordered nitrogen complexes overcoming strength–ductility trade-off in an additively manufactured high-entropy alloy. Virtual Phys. Prototyp. **15**(sup1), 532–542 (2020)
20. Y. Chew et al., Microstructure and enhanced strength of laser aided additive manufactured CoCrFeNiMn high entropy alloy. Mater. Sci. Eng. A **744**, 137–144 (2019)
21. Y.-K. Kim, J. Choe, K.-A. Lee, Selective laser melted equiatomic CoCrFeMnNi high-entropy alloy: microstructure, anisotropic mechanical response, and multiple strengthening mechanism. J. Alloys Compd. **805**, 680–691 (2019)
22. S. Xiang et al., Effects of process parameters on microstructures and tensile properties of laser melting deposited CrMnFeCoNi high entropy alloys. Mater. Sci. Eng. A **743**, 412–417 (2019)
23. J. Zhang, Y. Yan, B. Li, Selective Laser Melting (SLM) additively manufactured CoCrFeNiMn high-entropy alloy: process optimization, microscale mechanical mechanism, and high-cycle fatigue behavior. Materials **15**(23), 8560 (2022)
24. Y.-K. Kim et al., In-situ formed oxide enables extraordinary high-cycle fatigue resistance in additively manufactured CoCrFeMnNi high-entropy alloy. Addit. Manuf. **38**, 101832 (2021)
25. M. Jin et al., Cyclic plasticity and fatigue damage of CrMnFeCoNi high entropy alloy fabricated by laser powder-bed fusion. Addit. Manuf. **36**, 101584 (2020)
26. Y.-K. Kim, S. Yang, K.-A. Lee, Compressive creep behavior of selective laser melted CoCrFeMnNi high-entropy alloy strengthened by in-situ formation of nano-oxides. Addit. Manuf. **36**, 101543 (2020)
27. A. Gali, E.P. George, Tensile properties of high-and medium-entropy alloys. Intermetallics **39**, 74–78 (2013)
28. C. Zhang et al., Correlation between microstructural heterogeneity and anisotropy of mechanical properties of laser powder bed fused CoCrFeMnNi high entropy alloy. Mater. Sci. Eng. A **855**, 143920 (2022)
29. B. Wang et al., Anisotropic response of CoCrFeMnNi high-entropy alloy fabricated by selective laser melting. Materials **13**(24), 5687 (2020)
30. S. Feng et al., Effect of annealing and hot isostatic pressing on the structure and hydrogen embrittlement resistance of powder-bed fusion-printed CoCrFeNiMn high-entropy alloys. Metals **13**(3), 630 (2023)
31. ASTM, *ASTM G65–04, Standard Test Method for Measuring Abrasion Using the Dry Sand/Rubber Wheel Apparatus* (ASTM International, West Conshohocken, 2004)
32. ASTM, *ASTM G148–97, Standard practice for evaluation of hydrogen uptake, permeation, and transport in metals by an electrochemical technique*, vol. 1 (ASTM International, West Conshohocken, 2011), pp.1–10

33. ASTM, *ASTM G5, Reference test method for making potentiodynamic anodic polarization measurements* (ASTM International, West Conshohocken, 2013)

34. P. Wanjara et al., Microstructure and mechanical properties of Ti-6Al-4V additively manufactured by electron beam melting with 3D part nesting and powder reuse influences. J. Manuf. Mater. Process. **6**(1), 21 (2022)

35. F. Bernier, R. Tahara, M. Gendron, Additive manufacturing powder feedstock characterization using X-ray tomography. Met. Powder Rep. **73**(3), 158–162 (2018)

36. J.G. Kim et al., Nano-scale solute heterogeneities in the ultrastrong selectively laser melted carbon-doped CoCrFeMnNi alloy. Mater. Sci. Eng. A **773**, 138726 (2020)

37. ASTM, *ASTM B213–17, standard test methods for flow rate of metal powders using the hall flowmeter funnel* (ASTM International, West Conshohocken, 2017), pp.1–4

38. ASTM, *Astm B964–16, standard test methods for flow rate of metal powders using the carney funnel* (ASTM International, West Conshohocken, 2016)

39. G. Yablokova et al., Rheological behavior of β-Ti and NiTi powders produced by atomization for SLM production of open porous orthopedic implants. Powder Technol. **283**, 199–209 (2015)

40. ASTM, *B946–23, standard test methods for surface roughness of powder metallurgy (PM) products* (ASTM International, West Conshohocken, 2023)

41. ISO 25178-2, *Geometrical product specifications (GPS)—Surface texture: Areal—Part 2: terms, definitions and surface texture parameters.* ISO, 2012

42. P. Chen et al., The application of improved pso algorithm in pmmw image ostu threshold segmentation. Appl. Mech. Mater. **721**, 779–782 (2015)

43. Q. Zhu, L. Jing, R. Bi, *Exploration and improvement of Ostu threshold segmentation algorithm.* In: *2010 8th World Congress on Intelligent Control and Automation.* 2010. IEEE

44. S. Jiao, X. Li, X. Lu, *An improved Ostu method for image segmentation.* In: *2006 8th international Conference on Signal Processing.* 2006. IEEE

45. C. Desrosiers et al., Automated porosity segmentation in laser powder bed fusion part using computed tomography: a validity study. J. Intell. Manuf. **1**, 1–21 (2024)

46. S.M. Hartig, Basic image analysis and manipulation in ImageJ. Curr. Protoc. Mol. Biol. **102**(1), 1–12 (2013)

47. ASTM, *E384–17, standard test method for microindentation hardness of materials* (ASTM International, West Conshohocken, 2017)

48. ASTM, *E23–12c, Standard test methods for notched bar impact testing of metallic materials* (ASTM International, West Conshohocken, 2012), pp.1–25

49. O.A. Zambrano et al., Linear friction welding of abrasion resistant CPM 15V tool steel to an alloyed carbon shovel-tooth steel. J. Manuf. Mater. Process. **7**(2), 51 (2023)

50. P. Wanjara et al., Effect of pre-and post-weld heat treatments on linear friction welded Ti-5553. Metall. Mater. Trans. A **45**, 5138–5157 (2014)

51. S. Sarafan et al., Through-thickness residual stresses, microstructure, and mechanical properties of electron beam-welded CA6NM martensitic stainless steel after postweld heat treatment. Adv. Mater. Sci. Eng. **2020**, 1–16 (2020)

52. M. Osman et al., Effect of heat treatment on the microstructure and mechanical properties of 18Ni-300 maraging steel produced by additive–subtractive hybrid manufacturing. Materials **16**(13), 4749 (2023)

53. ASTM, *ASTM E23: Standard test method for notched bar impact testing of metallic materials* (ASTM International, West Conshohocken, 2007)

54. ASTM, *ASTM G65–91, Standard test method for measuring abrasion using the dry sand/rubber wheel apparatus* (ASTM International, West Conshohocken, 2016), pp.1–12

55. ASTM, *G102–89, Standard practice for calculation of corrosion rates and related information from electrochemical measurements* (ASTM International, West Conshohocken, 2004)

56. E. Van den Eeckhout, K. Verbeken, T. Depover, Methodology of the electrochemical hydrogen permeation test: a parametric evaluation. Int. J. Hydrogen Energy **1**, 1 (2023)

57. ASTM, *ASTM G148–97, Standard practice for evaluation of hydrogen uptake, permeation, and transport in metals by an electrochemical technique*, vol. 1 (ASTM International, West Conshohocken, 2018), pp.1–10

58. C. Dong et al., Effects of hydrogen-charging on the susceptibility of X100 pipeline steel to hydrogen-induced cracking. Int. J. Hydrogen Energy **34**(24), 9879–9884 (2009)

59. Z. Sun et al., Revealing hot tearing mechanism for an additively manufactured high-entropy alloy via selective laser melting. Scripta Mater. **168**, 129–133 (2019)

60. S. Griffiths et al., Combining alloy and process modification for micro-crack mitigation in an additively manufactured Ni-base superalloy. Addit. Manuf. **36**, 101443 (2020)

61. P. Niu et al., Hot cracking, crystal orientation and compressive strength of an equimolar CoCrFeMnNi high-entropy alloy printed by selective laser melting. Opt. Laser Technol. **127**, 106147 (2020)

62. S.E. Atabay et al., Microstructure and mechanical properties of rene 41 alloy manufactured by laser powder bed fusion. Mater. Sci. Eng. A **773**, 138849 (2020)

63. T. DebRoy et al., Additive manufacturing of metallic components–process, structure and properties. Prog. Mater. Sci. **92**, 112–224 (2018)

64. W. Zhang et al., Additive manufactured high entropy alloys: a review of the microstructure and properties. Mater. Des. **220**, 110875 (2022)

65. L.L. Parimi et al., Microstructural and texture development in direct laser fabricated IN718. Mater Charact **89**, 102–111 (2014)

66. M. Laurent-Brocq et al., Insights into the phase diagram of the CrMnFeCoNi high entropy alloy. Acta Mater. **88**, 355–365 (2015)

67. S.E. Atabay et al., In envelope additive/subtractive manufacturing and thermal post-processing of inconel 718. Materials **16**(1), 1 (2022)

68. S. Sarafan et al., Evaluation of maraging steel produced using hybrid additive/subtractive manufacturing. J. Manuf. Mater. Process. **5**(4), 107 (2021)

69. S. Sarafan et al., Benchmarking of 316L stainless steel manufactured by a hybrid additive/subtractive technology. J. Manuf. Mater. Process. **6**(2), 30 (2022)

70. A.O. Moghaddam et al., Additive manufacturing of high entropy alloys: a practical review. J. Mater. Sci. Technol. **77**, 131–162 (2021)

71. J. Xu et al., On the strengthening and embrittlement mechanisms of an additively manufactured Nickel-base superalloy. Materialia **10**, 100657 (2020)

72. D. Zhang et al., Grain refinement of alloys in fusion-based additive manufacturing processes. Metall. Mater. Trans. A **51**, 4341–4359 (2020)

73. T.-N. Lam et al., Tensile response of as-cast CoCrFeNi and CoCrFeMnNi high-entropy alloys. Crystals **12**(2), 157 (2022)

74. J.H. Kim et al., Mechanical properties and deformation twinning behavior of as-cast CoCrFeMnNi high-entropy alloy at

low and high temperatures. Mater. Sci. Eng. A **712**, 108–113 (2018)

75. M.A. Islam, J.J. Jiang, Y. Xie, Assessment of low-stress and rolling contact abrasion of WC-based overlays for the restoration of undercarriage components. Wear **477**, 203820 (2021)

76. E. Rabinowicz, *Wear and friction of materials* (Wiley, New York, 1965)

77. E. Rabinowicz, L. Dunn, P. Russell, A study of abrasive wear under three-body conditions. Wear **4**(5), 345–355 (1961)

78. E. Rabinowicz, A. Mutis, Effect of abrasive particle size on wear. Wear **8**(5), 381–390 (1965)

79. M.A. Islam, J.J. Jiang, Y. Xie, Optimizing material selection: a study of erosion-corrosion performance in homogeneous and carbide-containing materials. Wear **536**, 205181 (2024)

80. M. Kadowaki et al., First-principles analysis of the inhibitive effect of interstitial carbon on an active dissolution of martensitic steel. Corros. Sci. **163**, 108251 (2020)

81. Z. Wang et al., Pseudo-passivation mechanism of CoCrFeNiMo0.01 high-entropy alloy in H2S-containing acid solutions. Corros. Sci. **179**, 109146 (2021)

82. Y. Shi et al., Corrosion of Al xCoCrFeNi high-entropy alloys: Al-content and potential scan-rate dependent pitting behavior. Corros. Sci. **119**, 33–45 (2017)

83. J. Zhang et al., High-entropy alloys: a critical review of aqueous corrosion behavior and mechanisms. High Entropy Alloys Mater. **1**, 1–65 (2023)

84. Z. Szklarska-Smialowska, M. Janik-Czachor, The analysis of electrochemical methods for the determination of characteristic potentials of pitting corrosion. Corros. Sci. **11**(12), 901–914 (1971)

85. B.C. Syrett, PPR curves—a new method of assessing pitting corrosion resistance. Corrosion **33**, 221–224 (1977)

86. T. Bellezze, G. Giuliani, G. Roventi, Study of stainless steels corrosion in a strong acid mixture Part 1: cyclic potentiodynamic polarization curves examined by means of an analytical method. Corros. Sci. **130**, 113–125 (2018)

87. C.-J. Park, Y.-H. Lee, Initiation and repassivation of crevice corrosion of type 444 stainless steel in chloride solution. Met. Mater. Int. **10**, 447–451 (2004)

88. F. Ijsseling, Electrochemical methods in crevice corrosion testing: report prepared for the European federation of corrosion working party 'Physico-chemical testing methods of corrosion: Fundamentals and applications.' Br. Corros. J. **15**(2), 51–69 (1980)

89. A. Almarshad, D. Jamal, Electrochemical investigations of pitting corrosion behaviour of type UNS S31603 stainless steel in thiosulfate-chloride environment. J. Appl. Electrochem. **34**, 67–70 (2004)

90. N. Thompson, B. Syrett, Relationship between conventional pitting and protection potentials and a new, unique pitting potential. Corrosion **48**(8), 649–659 (1992)

91. J.R. Davis, Specialty handbook stainless steels, in *Atmospheric and aqueous corrosion*. ed. by J.R. Davis (ASM international, New York, 1994)

92. R. Jargelius-Pettersson, B. Pound, Examination of the role of molybdenum in passivation of stainless steels using AC impedance spectroscopy. J. Electrochem. Soc. **145**(5), 1462 (1998)

93. A. Pardo et al., Effect of Mo and Mn additions on the corrosion behaviour of AISI 304 and 316 stainless steels in H2SO4. Corros. Sci. **50**(3), 780–794 (2008)

94. Z. Xu et al., Corrosion resistance enhancement of CoCrFeMnNi high-entropy alloy fabricated by additive manufacturing. Corros. Sci. **177**, 108954 (2020)

95. S. Cao et al., Corrosion behavior of CoCrFeMnNi high entropy alloy in 3.5% NaCl solution with and without 0.05 M NaHSO3. J. Mater. Eng. Perform. **32**(16), 7545–7555 (2023)

96. S. Pathak et al., Aqueous corrosion behavior of cast CoCrFeMnNi alloy. J. Mater. Eng. Perform. **28**, 5970–5977 (2019)

97. Z. Zhou et al., Effects of W addition on the corrosion behaviors of FeCoNiCrMn high entropy alloy composites in the 3.5 wt% NaCl solution. Surf. Interfaces **23**, 100956 (2021)

98. C.-W. Lu et al., Comparative corrosion behavior of Fe50Mn-30Co10Cr10 dual-phase high-entropy alloy and CoCrFeMnNi high-entropy alloy in 3.5 wt% NaCl solution. J. Alloys Compd. **842**, 155824 (2020)

99. H. Peng et al., Corrosion behavior of an equiatomic CoCrFeMnNi high-entropy alloy-a comparison between selective laser melting and cast. Front. Mater. **7**, 244 (2020)

100. Q. Ye et al., Microstructure and corrosion properties of CrMnFeCoNi high entropy alloy coating. Appl. Surf. Sci. **396**, 1420–1426 (2017)

101. Y. Wang et al., Effect of the grain size on the corrosion behavior of CoCrFeMnNi HEAs in a 0.5 M H$_2$SO$_4$ solution. J. Alloys Compd. **858**, 157712 (2021)

102. S.C. Marques, A.V. Castilho, D.S. dos Santos, Effect of alloying elements on the hydrogen diffusion and trapping in high entropy alloys. Scripta Mater. **201**, 113957 (2021)

103. D. Dos Santos, P. De Miranda, Hydrogen solubility in amorphous and crystalline materials. Int. J. Hydrogen Energy **23**(11), 1011–1017 (1998)

104. J. Lee et al., Effective hydrogen diffusion coefficient for CoCrFeMnNi high-entropy alloy and microstructural behaviors after hydrogen permeation. Int. J. Hydrogen Energy **45**(16), 10227–10232 (2020)

105. D.-H. Lee et al., A novel methodology to estimate hydrogen diffusivity and its applications in revealing hydrogen effects in CoCrNi medium-entropy alloy versus 316L stainless steel. Int. J. Plast. **169**, 103737 (2023)

106. S. Xiukui, X. Jian, L. Yiyi, Hydrogen permeation behaviour in austenitic stainless steels. Mater. Sci. Eng. A **114**, 179–187 (1989)

107. J. Lin et al., Hydrogen permeation behavior and hydrogen-induced defects in 316L stainless steels manufactured by additive manufacturing. Mater. Chem. Phys. **250**, 123038 (2020)

108. X. Yue et al., Effect of hydrogen on the passivation for ultra-thin 316 L SS foil. NPJ Mater. Degrad. **7**(1), 79 (2023)

109. L. Guo et al., Effect of hydrogen on pitting susceptibility of 2507 duplex stainless steel. Corros. Sci. **70**, 140–144 (2013)

110. J. He et al., Hydrogen embrittlement behavior of 13Cr-5Ni-2Mo supermartensitic stainless steel. Corros. Sci. **176**, 109046 (2020)

111. J. He et al., A novel 13Cr austenitic stainless steel with excellent mechanical properties and high hydrogen embrittlement resistance via heterostructure and TRIP effects. Mater. Sci. Eng. A **793**, 139835 (2020)

112. Z. Pu, Y. Chen, L. Dai, Strong resistance to hydrogen embrittlement of high-entropy alloy. Mater. Sci. Eng. A **736**, 156–166 (2018)

113. T. Zhu et al., Influence of hydrogen behaviors on tensile properties of equiatomic FeCrNiMnCo high-entropy alloy. J. Alloys Compd. **892**, 162260 (2022)

114. S. Lee et al., Deuterium transport and isotope effects in type 316L stainless steel at high temperatures for nuclear fusion and nuclear hydrogen technology applications. Curr. Appl. Phys. **14**(10), 1385–1388 (2014)

115. J. Belo et al., Hydrogen diffusivity and interaction with Fe20Mn20Ni20Co20Cr20 and Fe22Mn40Ni30Co6Cr2 high-entropy alloys. J. Alloys Compd. **815**, 152314 (2020)

Authors and Affiliations

Sila Ece Atabay[1,2] · Sheida Sarafan[1] · Aminul Islam[3] · Fabrice Bernier[1] · Javad Gholipour[1] · Robert Amos[4] · Prakash Patnaik[1] · Priti Wanjara[1] · Mathieu Brochu[2]

✉ Priti Wanjara
  Priti.Wanjara@cnrc-nrc.gc.ca

  Aminul Islam
  MdAminul.Islam@nrc-cnrc.gc.ca

1 National Research Council Canada, Transportation and Manufacturing Division, Montréal, QC H3T 1J4, Canada

2 Department of Mining and Materials Engineering, McGill University, Montréal, QC H3A 0C5, Canada

3 National Research Council Canada, Clean Energy Innovation Research Center, Vancouver, BC V6T 1W5, Canada

4 Department of National Defence, Directorate of Technical Airworthiness and Engineering Support (DTAES), Ottawa, ON K1A 0K2, Canada